Thermally Responsive Hydrogel-Nanoparticle Composite Materials for Therapeutic Delivery
by

Laura Elizabeth Strong

Department of Biomedical Engineering
Duke University

Date:_____
Approved:

_____
Jennifer L. West, Supervisor

_____
Ashutosh Chilkoti

_____
Farshid Guilak

_____
Nimmi Ramanujam

_____
William M. Reichert

Dissertation submitted in partial fulfillment of
the requirements for the degree of Doctor
of Philosophy in the Department of
Biomedical Engineering in the Graduate School
of Duke University

2014

ABSTRACT

Thermally Responsive Hydrogel-Nanoparticle Composite Materials for Therapeutic Delivery
by

Laura Elizabeth Strong

Department of Biomedical Engineering
Duke University

Date:_____
Approved:

_____
Jennifer L. West, Supervisor

_____
Ashutosh Chilkoti

_____
Farshid Guilak

_____
Nimmi Ramanujam

_____
William M. Reichert

An abstract of a dissertation submitted in partial fulfillment of the requirements for the degree of Doctor of Philosophy, in the Department of Biomedical Engineering in the Graduate School of Duke University

2014

Abstract

Cancer is currently the second leading cause of death in the United States. Although many treatment options exist, some of the most common, including radiotherapy and chemotherapy, are restricted by dose-limiting toxicities. In addition, the largest hurdle for translating novel biological therapies such as siRNA into the clinic is lack of an efficient delivery mechanism to get the therapeutic into malignant cells. This work aims to improve this situation by engineering a minimally invasive controlled release system that specifically delivers therapeutics to the site of malignant tissue. This platform consists of two novel material components: a thermally responsive poly[N-isopropylacrylamide-co-acrylamide] (NIPAAm-co-AAm) hydrogel and gold-silica nanoshells. Therapeutic molecules are encapsulated within a poly(NIPAAm-co-AAm) hydrogel carrier, leading to increased serum stability, circulation time, and decreased exposure to off-site tissues. Additionally, gold-silica nanoshells embedded within this hydrogel will be used to optically trigger therapeutic release from the carrier. This hydrogel-nanoshell composite material was designed to be swollen under physiologic conditions (37 ^{o}C), and expel large amounts of water and absorbed molecules at higher temperatures (40-45 ^{o}C). This phase transition can be optically triggered by embedded gold-silica nanoshells, which rapidly transfer near-infrared (NIR) light energy into heat due to the surface plasmon resonance phenomena. NIR light can deeply penetrate biological tissue with little attenuation or damage to tissue, and upon exposure to such light a rapid temperature increase, hydrogel collapse, and drug expulsion will occur.

Ultimately, these drug-loaded hydrogel-nanoshell composite particles would be injected intravenously, passively accumulate in tumor tissue due to the enhanced permeability and retention (EPR) effect, and then can be externally triggered to release their therapeutic payload by exposure to an external NIR laser. This dissertation describes the synthesis, characterization, and validation of such a controlled therapeutic delivery platform.

Initial validation of poly(NIPAAm-co-AAm)-gold nanoshell composites to act as a material in site-specific cancer therapeutic delivery was accomplished using bulk hydrogel-nanoparticle composite disks. The composite material underwent a phase transition from a hydrated to a collapsed state following exposure to NIR light, indicating the ability of the NIR absorption by the nanoshells to sufficiently drive this transition. The composite material was loaded with either doxorubicin or a DNA duplex (a model nucleic acid therapeutic), two cancer therapeutics with differing physical and chemical properties. Release of both therapeutics was dramatically enhanced by NIR light exposure, causing 2–5 fold increase in drug release. Drug delivery profiles were influenced by both the molecular size of the drug as well as its chemical properties.

Towards translation of this material into *in vivo* applications, the hydrogel-nanoshell composite material was synthesized as injectable-sized particles. Such particles retained the same thermal properties as the bulk material, collapsing in size from ~330 nm to ~270 nm upon NIR exposure. Furthermore, these particles were loaded with the chemotherapeutic doxorubicin and NIR exposure triggered a burst release of the drug payload over only 3 min. *In vitro*, this platform provided increased delivery of

doxorubicin to colon carcinoma cells compared to free-drug controls, indicating the irradiated nanoshells may increase cell membrane permeability and increase cellular uptake of the drug. This phenomena was further explored to enhance cellular uptake of siRNA, a large anionic therapeutic which cannot diffuse into cells easily.

This work advances the development of an injectable, optically-triggered delivery platform. With continued optimization and *in vivo* validation, this approach may offer an novel treatment option for cancer management.

Dedication

To my mom and dad; without their constant love, support, and encouragement none of this would have been possible.

Contents

List of Tables

List of Figures

List of Abbreviations

AAc: acrylic acid

AAm: acrylamide

APS: ammonium persulfate

APTES: 3-aminopropyltriethoxysilane

ATRP: atom transfer radical polymerization

Br-initiator: bis[2-(2'bromoisobutryloxy)ethyl]disulfide

DLS: dynamic light scattering

dsDNA: double stranded DNA segment of 21 base pairs (siRNA model molecule)

EDTA: ethylenediaminetetraacetic acid

ELP: elastin-like polypeptide

EPR: enhanced permeability and retention

EtOH: ethanol

HNCP: hydrogel-nanoshell composite particle (synthesized via hydrogel template method)

LCST: lower critical solution temperature

MBAAm: methylenebisacrylamide

μCP: microcontact printing

MeOH: methanol

NAPT: nanoshell-assisted photothermal therapy

NCNS: poly(NIPAAm-co-AAm)-coated gold nanoshells (synthesized via SI-ATRP)

NIPAAm: *N*-isopropylacrylamide

NIPMAAm: *N*-isopropylmethacrylamide

NIR: near infrared

NHP: poly(NIPAAm-co-AAm) hydrogel particles without nanoshells (synthesized via hydrogel template method)

PAGE: poly(acrylamide) gel electrophoresis

PBS: phosphate-buffered saline

PDMS: polydimethylsiloxane

PDI: polydispersity index

PEG: poly(ethylene glycol)

PEGDA: poly(ethylene glycol)diacrylate

PLGA: poly(lactic-co-glycolic)acid

PMMA: poly(methyl methacrylate)

OCT: optical coherence tomography

RES: reticuloendothelial system

SI-ATRP: surface initiated- atom transfer radical polymerization

TAE: tris-acetate EDTA

TBS: tris-buffered saline

TCEP: tris(2-carboxyethyl)phosphine

TEM: transmission electron microscope

TEMED: *N*,*N*,*N*′,*N*′-tetramethylethylenediamine

TEOS: tetraethyl orthosilicate

THF: tetrahydrofuran

THPC: tetrakis(hydroxymethyl)phosphonium chloride

TSL: temperature-sensitive liposome

Acknowledgements

First, I would like to thank Dr. Jennifer West for all her mentorship and guidance. Her help, encouragement, and insight have shaped me into the independent scientist that I am today. Thank you to my committee members Dr. Chilkoti, Dr. Guilak, Dr. Ramanujam, and Dr. Reichert for taking the time to be part of my committee and being available for advice and support.

I would like to thank all the members of the West lab, past and present, for all their help and support. I especially would like to acknowledge those members of "Team Nano": Dr. Andrew Coughlin, Shreyas Dahotre, Jeff Ashton, Dr. Emily Day, and honorary member Dr. Adam Lin, for teaching me everything I know about nanoparticle synthesis and characterization, and also for making coming into the lab everyday more enjoyable. Thank you to Dr. Ryan Schweller, for always being willing to talk random science with me and being what seems like a bottomless pit of knowledge, especially when it came to my work with DNA/RNA and imaging techniques. A big thank you to Dr. Maude Cuchiara, without whom the lab would not run nearly as smoothly, and who always had time to chat about life in general and keep me sane throughout grad school.

I would like to thank my family and friends for all their love and support throughout this journey. Mom, Dad, Rick, Bea, Liam, and Connor-- thank you all for a lifetime (and more) of support and encouragement and always being just a phone call away while I've been on the other side of the country. Thanks to all my friends

throughout grad school-- Anne, Liezl, Adam, Omar, Laila, Nicky, Ryan, Andy, Maude, and many others-- for all the laughs and good times.

Finally, I would like to acknowledge my financial support from the NIH Nanobiology Graduate Interdisciplinary Training Program and the HHMI Med into Grad Training Program.

1. Introduction

Cancer, a group of diseases characterized by the growth and spread of abnormal cells, remains a considerable health concern today. In 2010, cancer was the second leading cause of death in the United States following heart diseases, accounting for approximately 1500 deaths/day; almost 1 in 4 deaths in the U.S. can be attributed to cancer (American Cancer Society, 2010). In addition, over the past 15+ years, the death rate due to heart disease rate has decreased by 40%, while the cancer death rate has stayed more constant with only an 18% decrease, as seen in Figure 1.1.

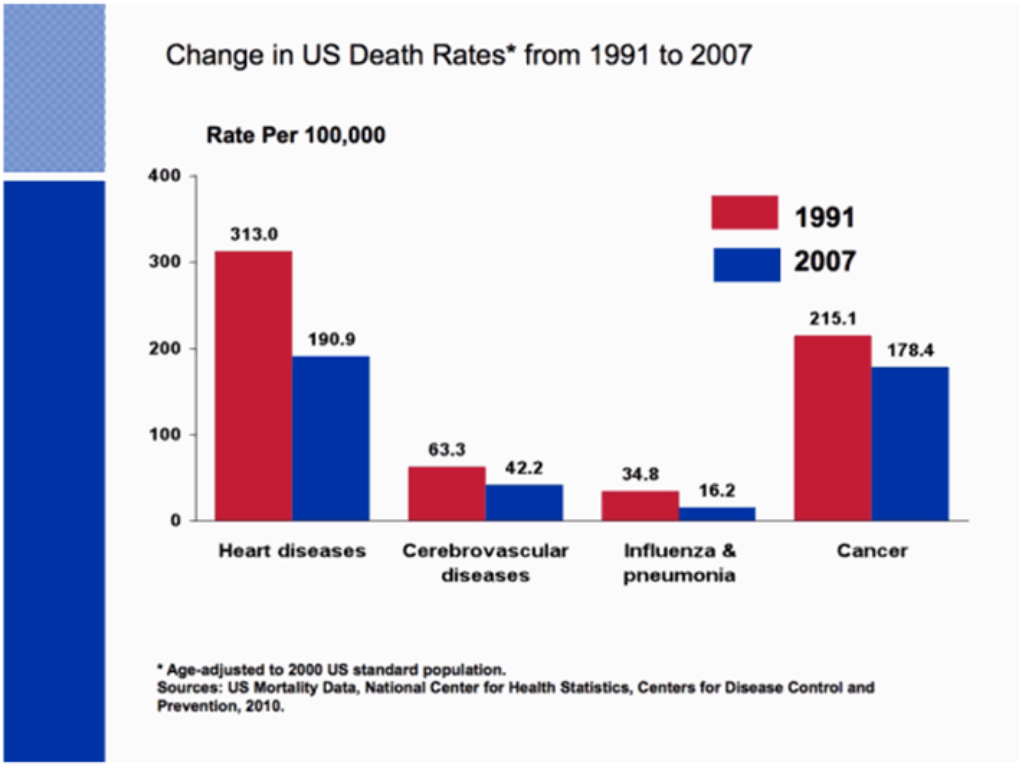

Figure 1.1. U.S. mortality rates for several diseases in 1991 and 2007. Information age adjusted to 2000 U.S. standard population. From (American Cancer Society, 2010).

Furthermore, the cost of cancer, including both direct medical costs and indirect mortality costs, was estimated to be $263.8 billion in 2010 (American Cancer Society, 2010). These statistics indicate that advances in cancer treatments are still needed in order to better manage this disease. The research presented in this dissertation aims to improve cancer treatment by utilizing a novel platform to better control the delivery of cancer therapeutics.

1.1. Characteristics of Cancer

Cancer is widely recognized to be a disease involving dynamic changes in the genome. It occurs in a wide variety of cell types and tissues, but is universally characterized by changes that allow for unregulated cell cycle progression, growth, and invasion. Tumorigenesis is a multistep process in which each step reflects genetic alterations that drive a progressive transformation of normal cells into highly malignant derivatives (Hanahan and Weinberg, 2000). In a 2000 review, Hanahan and Weinburg assert that this transformation into a malignant state manifests in six essential alterations in cell physiology: (1) self-sufficiency in growth signals, (2) insensitivity to growth-inhibitory (anti-growth) signals, (3) limitless replicative potential, (4) evasion of programmed cell death (apoptosis), (5) sustained angiogenesis, and (6) tissue invasion and metastasis (Hanahan and Weinberg, 2000). The authors note that these capabilities are shared in common by most, if not all types of human tumors.

Over the past 10 years, progress in cancer research has led to new observations that serve to both clarify and modify the original six hallmarks. In response, Hanahan and Weinburg wrote another review in 2011, in which four new concepts were discussed

(Hanahan and Weinberg, 2011). Two of these new concepts, (1) genome instability and mutation and (2) tumor-promoting inflammation, are thought be critical to the scope and conceptualization of the original six hallmarks. In addition, two new, unique hallmarks were recognized: (1) reprogramming of energy metabolism and (2) evading immune destruction. These hallmarks, along with specific therapeutic approaches to disrupt each hallmark, are illustrated in Figure 1.2.

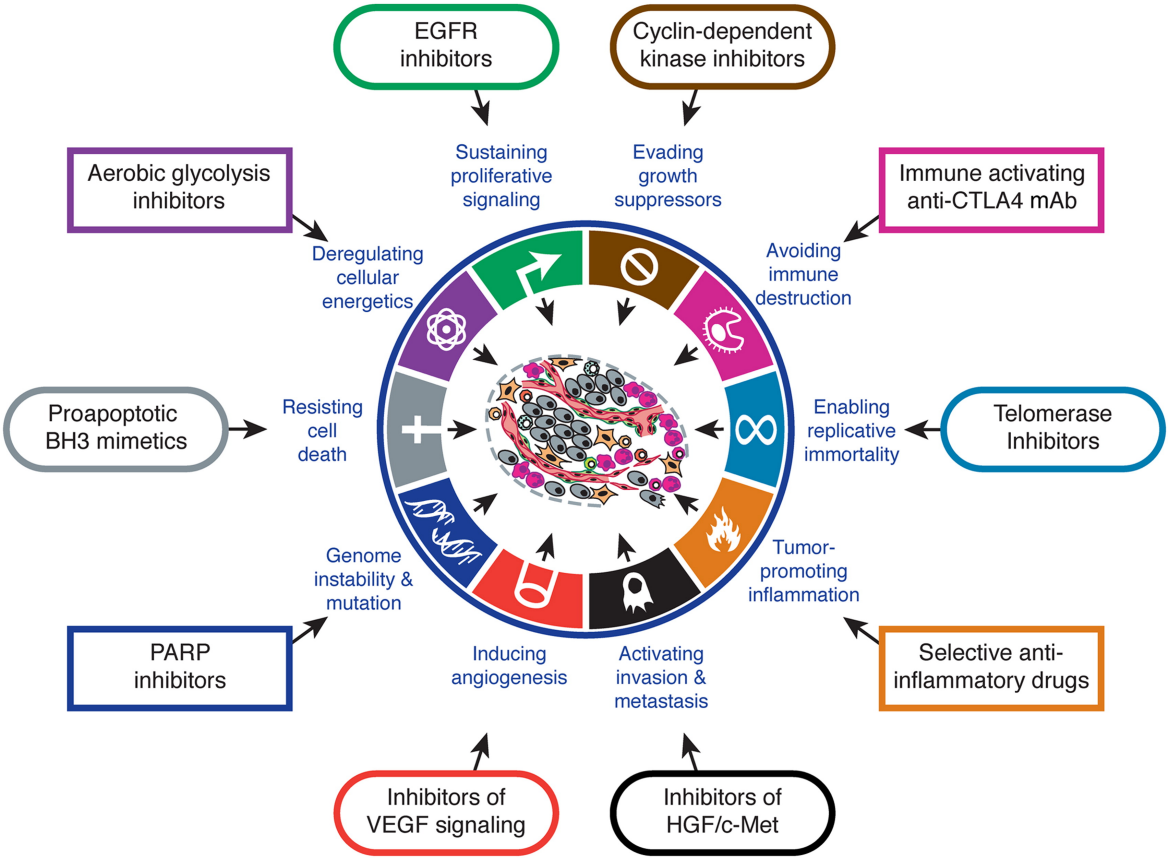

Figure 1.2. Therapeutic targeting of the ten hallmarks of cancer. Drugs that interfere with each acquired capability of cancer cells listed are either in clinical trials or approved for clinical use in certain forms of cancer. From (Hanahan and Weinberg, 2011).

1.2. Motivation: Current Standard of Care

Conventional cancer treatments include surgery, radiation therapy, and chemotherapy. These treatments may be used alone, but are also often used in combination. The goal of each treatment option is to kill as much malignant tissue as possible while minimizing harm to surrounding healthy tissues.

Surgical therapy provides the physical removal (resection) of the tumor mass (McKinnell, 2006). This is often the most effective treatment for localized disease. It is common for adjacent, healthy tissue and associated lymph nodes to be resected during surgery to help the pathologist determine if the tumor is invading surrounding tissue and decrease the risk of recurrence or metastasis. However, surgery is not applicable for tumors in inaccessible anatomic locations or with extensive intermingling of tumor and critical normal tissues (McKinnell, 2006).

In radiation therapy, tumor cells are exposed to ionizing radiation resulting in DNA damage, which leads to cell death when the cells try to divide. Therefore, this therapy is most toxic to highly proliferative cells, including cancer cells. However, since both malignant cells and healthy tissue use the same mechanism for cell division, radiation therapy also kills the rapidly dividing cells within renewing tissues such as hair follicles, oral-gastrointestinal epithelium, and hematopoietic tissue. Although radiation therapy is usually focused to minimize these, these off-site toxicities, along with other chronic toxicities, ultimately determine the maximum dose a patient may receive of radiation in his or her lifetime (McKinnell, 2006).

Chemotherapy is defined as the use of drugs to treat or control cancer. These drugs are usually given systemically and aim to target highly proliferative cells. These types of drugs include alkylating agents, antimetabolites, natural or semisynthetic products, and hormones or hormone inhibitors (Rubin and Williams, 2001). The drugs are generally cell cycle phase-specific, as demonstrated in Figure 1.3, and thereby target highly proliferative cells to a greater degree than more dormant tissues (Seiwert et al., 2007). Like radiation therapy, off-site toxicities of chemotherapeutics are significant in tissues that are normally in a highly proliferative state, such as the bone marrow, gastrointestinal tract, and hair follicles (Rubin and Williams, 2001). This leads to the side effects that most people associate with chemotherapy regimens: immunosuppression, nausea, and alopecia.

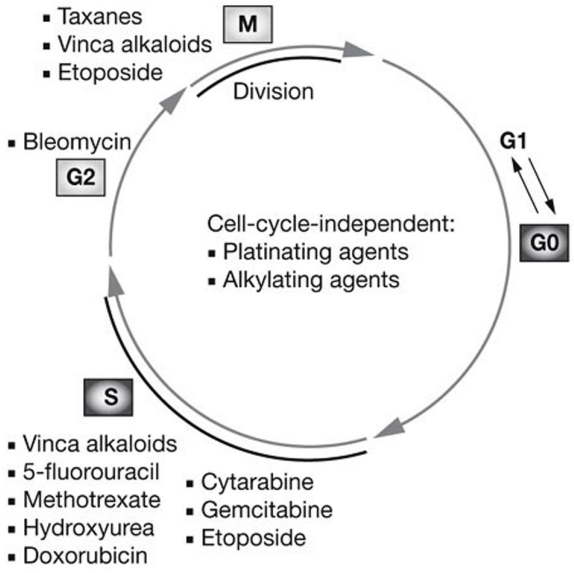

Figure 1.3. Cell cycle schematic and respective sensitivity to chemotherapeutic agents. Most agents are active in the S and M phases of the cell cycle and thereby target more proliferative tissues to a higher degree than more dormant tissues. Adapted from (Seiwert et al., 2007).

In addition, many chemotherapeutics also have less common toxic reactions, including pulmonary fibrosis (seen with bleomycin, buslfan, and mitocycin C) and cardiotoxicity (seen with doxorubicin, daunomycin, mitoxantrone, and idarubicin) (Rubin and Williams, 2001). These severe toxicities often lead to restrictions in the total doses of these drugs that may be administered (Rubin and Williams, 2001). If a patient experiences these toxicities, treatment often has to be ceased immediately, even if the drug is effective against the malignant cells. These drugs would benefit from administration in a manner that minimizes drug exposure to healthy tissues associated with these toxic effects. A more detailed explanation of such controlled delivery manners can be found in Section 1.4.

1.2.1. Emerging Therapy: siRNA

In recent years, advancing technologies in molecular biology have demonstrated that small segments of RNA can be used as a genetics-based cancer therapy. In RNA interference, double stranded RNA (dsRNA) hinders the expression of a target gene as a result of sequence homology (Oh and Park, 2009). This process occurs naturally in mammalian cells, where the enzyme Dicer initiates RNA silencing by breaking down long dsRNA molecules into small interfering RNA (siRNA) segments of around 21-23 nucleotides (Oh and Park, 2009). The siRNA molecules go on to bind to complementary sequences in cytosolic mRNA transcripts, thereby preventing protein translation of the binding targets. The overall process of RNA interference is summarized in Figure 1.4 (Bumcrot et al., 2006).

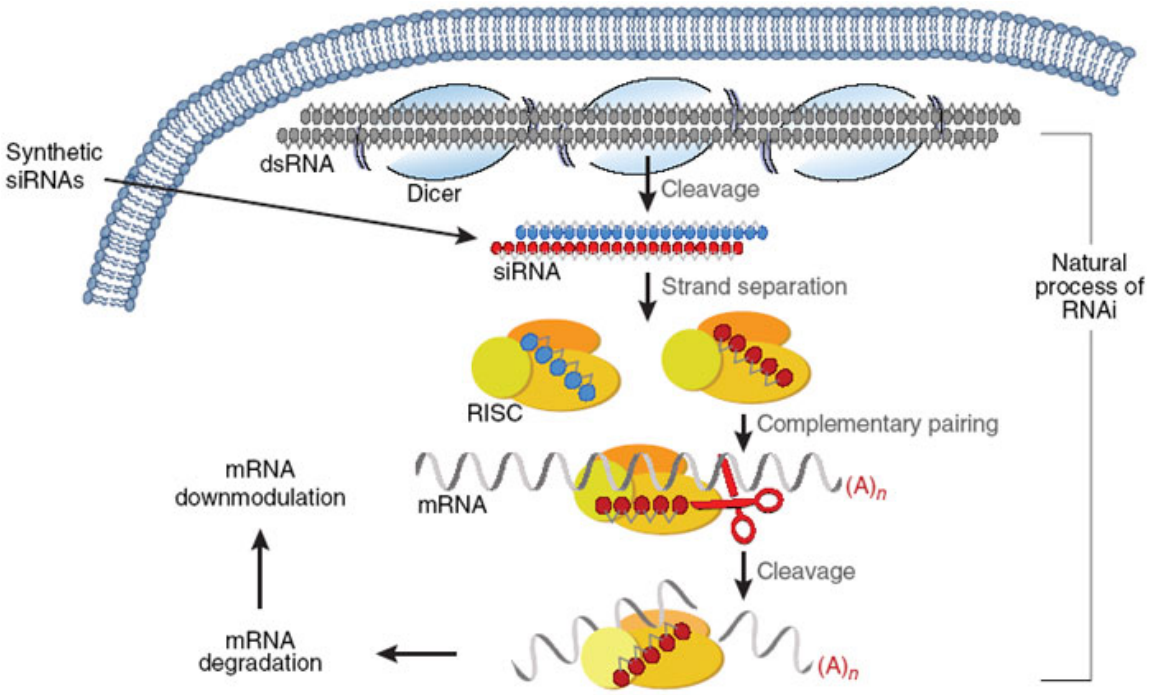

Figure 1.4. Cellular mechanisms of RNA interference. First, dsDNA is cleaved by Dicer into siRNA. These siRNAs are then incorporated into the RNA-induced silencing complex (RISC), where the strands are separated. The RISC complex containing the antisense strand seeks out and binds to complementary mRNA sequences. These mRNAs are then cleaved by the enzyme argonaute, thereby causing mRNA degradation and prevention protein translation. From (Bumcrot et al., 2006).

This biological mechanism can be exploited for cancer therapy by the introduction of synthetic siRNA targeted to a gene of choice. Elbashir et al. first showed that the introduction of a 21-nucleotide artificial siRNA could trigger gene silencing in mammalian cells (Elbashir et al., 2001). This proof of concept study demonstrated the downregulation of several different genes coding for various different firefly luciferases (Elbashir et al., 2001). Since then, siRNA has been used to downregulate key proteins in the progression of cancer showing great therapeutic potential. In fact, several siRNA molecules have advanced all the way to clinical trials (Oh and Park, 2009). Furthermore,

siRNA has been investigated for use in the treatment of many cancers including breast, ovary, cervix, liver, lung, and prostate. (Oh and Park, 2009).

Therapy using siRNA has several advantages over more traditional therapeutic strategies. First, siRNA interferes with translation, not with DNA transcription as seen in DNA-based gene therapy approaches. This approach therefore minimizes concerns about possible adverse gene alterations (Oh and Park, 2009). Another advantage is that siRNA can act on a wide range of protein targets, whereas traditional chemical drugs are limited to acting on certain classes of receptors, ion channels, and enzymes. Current biological therapies, including monoclonal antibodies and cytokines, mainly target moieties on the cell surface. SiRNAs, however, can target any mRNA regardless of the cellular location of the translated protein (Oh and Park, 2009).

A major challenge in the translation of siRNA therapy to the clinic is the efficient delivery of the molecule into target cells (Oh and Park, 2009). RNA is relatively large, anionic and hydrophilic, and therefore cannot effectively enter cells by passive diffusion. In addition, RNA molecules injected intravenously are quickly degraded by serum nuclease enzymes and cleared rapidly through the kidneys (Bumcrot et al., 2006). Furthermore, these molecules have limited penetration across capillary endothelium and inefficient uptake by parenchymal cells (Bumcrot et al., 2006). Therefore, development of an *in vivo* delivery system for siRNA is paramount for an efficient therapeutic effect to take place (Oh and Park, 2009).

1.3. Therapeutic Delivery to Solid Tumors

As mentioned in Section 1.1, one of the hallmarks of cancer is sustained angiogenesis. For a solid tumor to grow beyond 2-3 mm, it must recruit its own blood supply in order to transport nutrients and O_2 to its rapidly proliferating cells (Folkman, 1971). However, the tumor vasculature that forms differs both structurally and functionally from normal vasculature (Jain, 2005). Tumor vasculature is highly disorganized, consisting of tortuous vessels with uneven diameters (Carmeliet and Jain, 2000). Additionally, these vessels may lack functional pericytes (Benjamin et al., 1999), and have been observed to have gaps between endothelial cells as large as 2 μm (Hashizume et al., 2000), leading to vessels being highly "leaky". These phenotypic differences are hypothesized to be due to a disruption in the balance between "pro-angiogenic" and "anti-angiogenic" factors (Carmeliet and Jain, 2000, Jain, 2005). In the development of normal vasculature, "pro-angiogenic" factors that promote vessel formation (such as VEGF and Ang1) are balanced with "anti-angiogenic" factors that restrict vascularization (such as Ang2), leading to the formation of a highly organized, hierarchical vessel structure (Carmeliet and Jain, 2000). However, in tumor angiogenesis, there is a tip in the balance towards the "pro-angiogenic" side, leading to rapid growth of a disorganized vascular network (Carmeliet and Jain, 2000). These differences in vasculature are summarized in Figure 1.5.

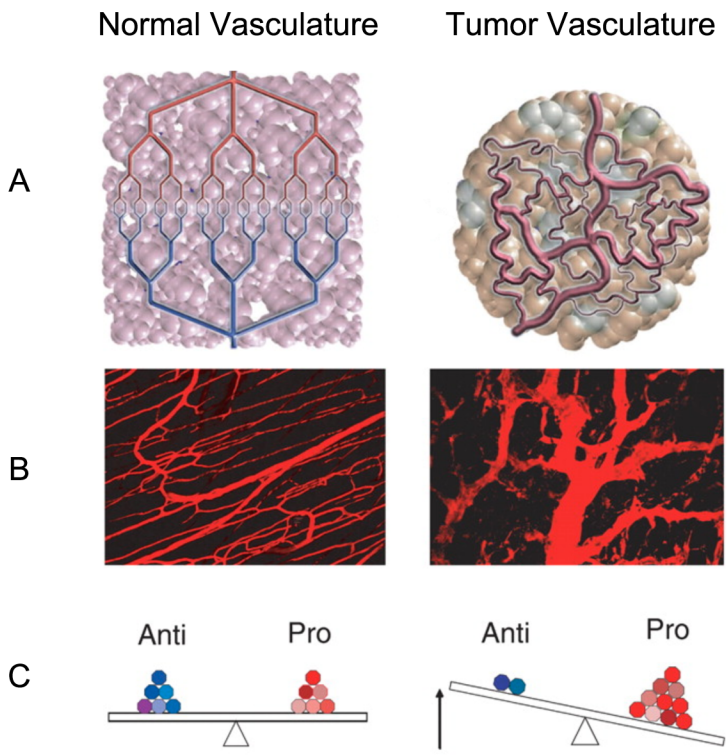

Figure 1.5. Differences in normal vs. tumor vasculature. [A] Normal vasculature (left) is highly organized in a distinct hierarchal structure, whereas tumor vasculature (right) is disorganized and erratic. [B] Representative images of normal vasculature (skeletal muscle, left) and tumor vasculature (colon carcinoma, right). [C] The formation of these vessel phenotypes are hypothesized to be due to the balance between pro- and anti-angiogenic factors, where in the case of tumor vasculature formation this balance tips towards the "pro-angiogenic" side. Adapted from (Jain, 2005).

In tumor vasculature, particles ranging in size from 10-500 nm have been shown to pass through the gaps between endothelial cells and extravasate out of the vessel (Maeda et al., 2000, Cuenca et al., 2006). Additionally, tumors often do not have the functional lymphatic vessels that are seen in normal tissues (Jain, 1987), leading to these extravasated particles persisting in the tumor interstitium. This phenomena, first observed by Matsumura and Maeda in 1986, is known as the "Enhanced Permeability and

Retention" (EPR) effect (Matsumura and Maeda, 1986), and is often exploited for delivery of nanoparticle platforms to solid tumors (Maeda et al., 2000).

It is important to note that the leaky vasculature and lack of functional lymphatics in solid tumors leads to an increase in interstitial pressure towards the center of the tumor (Baxter and Jain, 1989). This causes a convective barrier for delivering therapeutics to the center of the tumor and leads to diffusion being the main mode of transport of molecules at the center of the tumor (Jain, 1990, Baxter and Jain, 1989).

1.4. Controlled Delivery Methods

Therapeutic efficacy of both chemotherapeutics and biological therapeutics (such as siRNA) would benefit from administration in a controlled delivery manner. Controlled delivery systems can influence the performance of a therapeutic agent by manipulation of its effective concentration, location, and duration (Park, 1997). Drug delivery via controlled release offers several advantages to improve cancer therapy including (1) localized delivery of the drug to a particular tissue, thereby lowering the systemic drug level, (2) preservation of drugs that are rapidly destroyed by the body, (3) reduced need for follow up care, (4) increased comfort, and (5) improved compliance (Langer, 1990).

The field of controlled drug release has grown from the 1940s, when sustained release products aiming to reduce the frequency of dosing first came on the market, to present day, where much focus is on delivery of a variety of molecules including genes, proteins, and other therapeutics by a wide range of self-regulating systems (Park, 1997). In fact, in a review dating back to 1981, Langer and Peppas noted that while synthesis

and discovery of new potent drugs is important, critical attention should also be given to the manner in which these drugs are delivered (Langer and Peppas, 1981).

Typically, these systems are designed to release therapeutics at a desired anatomical site and maintain drug concentrations within a therapeutic band for a desired duration, as illustrated in Figure 1.6 (Liechty et al., 2010). Such systems may be diffusion controlled, swelling controlled (due to osmosis), chemically controlled (due to material degradation) or externally-triggered by a stimulus such as changes in temperature or pH (Liechty et al., 2010). Polymeric materials have been developed for all four of these types of delivery schemes.

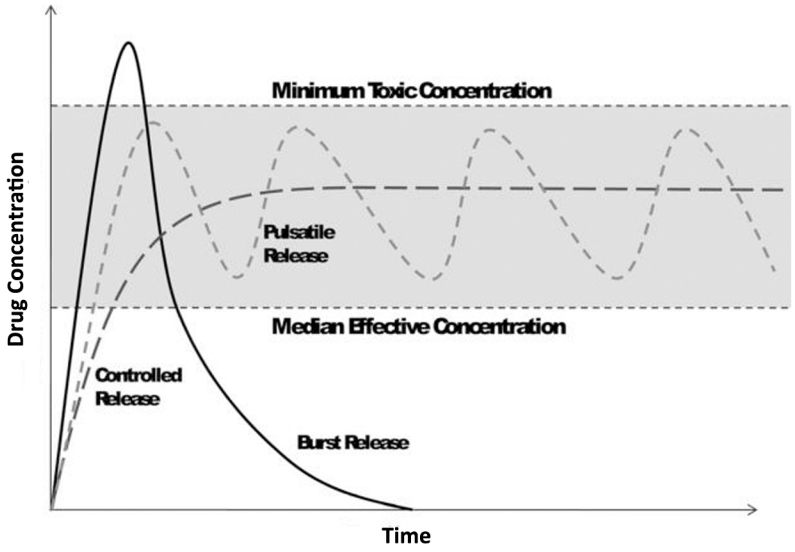

Figure 1.6. Profiles of controlled release, burst release, and pulsatile release systems within a therapeutic band. Adapted from (Liechty et al., 2010).

There are some controlled delivery systems for chemotherapeutics on the market today, most notably Doxil®, which is a poly(ethylene glycol) [PEGylated] liposome containing the chemotherapeutic doxorubicin (Safra et al., 2000). This formulation

increases the serum half-life of the drug, thereby allowing a higher percentage of the administered dose to reach the tumor site (Safra et al., 2000). However, Doxil® is given systemically and some drug will leak out of the liposome over time, leading to off-site toxicity.

Another example of a controlled delivery system for chemotherapeutics that is on the market is bis-chloronitrosourea (BCNU) wafers (Gliadel®) for the management of brain malignancies. This chemically-controlled delivery platform consists of poly(anhydride)-based wafers and are loaded with the chemotherapeutic carmustine. These poly(anhydride) wafers are implanted directly into the brain following surgical tumor resection, and slowly hydrolytically degrade, releasing drug over time to reduce the likelihood of recurrence (Westphal et al., 2003). However, surgical access is necessary for implantation, making this strategy not applicable for all cancer sites. A non-invasive drug delivery system that triggers drug release to only occur at the tumor site would be advantageous over these existing drug delivery systems.

1.5. Conclusions and Design Rationale

This work aims to create an externally-triggered drug delivery platform for the delivery of various cancer therapeutics, ranging from small molecules to large biologics. This platform will be designed to provide a burst delivery of a chemotherapeutic only at the site of malignant tissue. The platform will be comprised of two novel material components: gold-silica nanoshells and a thermally-responsive poly(N-

isopropylacrylamide-co-acrylamide) (NIPAAm-co-AAm) polymer coating, summarized in Figure 1.7.

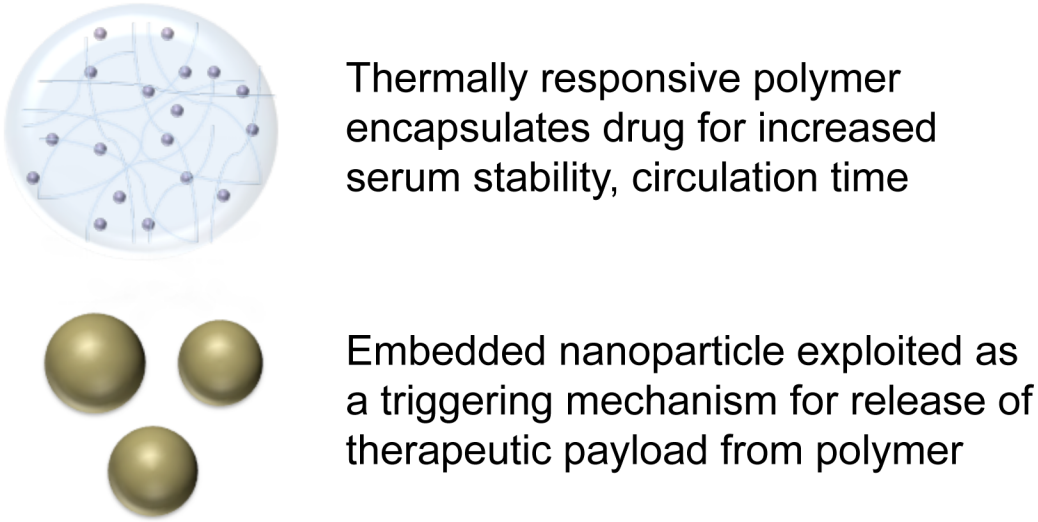

Figure 1.7. Summary of material components for developing an injectable, optically-triggered drug delivery platform.

The polymer coating will contain drug, allowing the drug-filled particles to circulate throughout the body without the drug acting on tissue. Drug release from this coating will be triggered by temperature increases, which in turn can be triggered by exploiting the optical properties of the gold-silica nanoshell.

Nanoparticle platforms offer promising approaches for cancer therapy due to unique material properties that are seen at the nanoscale. In particular, the size and optical properties of gold-silica nanoshells have been utilized for photothermal therapy, which is significantly less invasive than traditional therapies such as surgery. Additionally, unlike most chemotherapeutic and radiation therapy approaches, the location of the therapy

(heating) is tightly controlled to occur only where nanoshell and a near-infrared (NIR) laser application are combined.

Stimuli-responsive materials have been widely studied in the context of controlled drug delivery (Qiu and Park, 2001). In particular, thermally-responsive hydrogels can be used to encapsulate a drug payload in their swollen state, and then triggered to collapse and expel water and absorbed molecules upon a temperature increase. By combining such a material with the above mentioned NIR absorbing nanoparticles to locally generate heat in response to light, extremely tight spatial and temporal control over material transition and drug release can be achieved. A more detailed background on gold nanoparticles and stimuli-responsive materials follows in Chapter 2.

This dissertation builds on successful results from previous studies of thermally-responsive hydrogel-nanoparticle composites to create an optically-controlled drug delivery platform. This injectable, controlled delivery platform consists of a drug-containing, thermally-responsive hydrogel coating on individual gold-silica nanoshells. These particles can be injected intravenously and passively accumulate in tumor tissue due to the EPR effect. Once the particles reach the tumor site, an NIR laser will be applied to the tumor. This will cause a rapid heating of the embedded nanoshells, which in turn triggers a collapse of the polymer coating and release of absorbed drug molecule directly at the tumor site.

In the next chapter, the methods to synthesize and characterize the gold-silica nanoshells used throughout this dissertation, as well as the synthesis and characterization of bulk poly(NIPAAm-co-AAm)-gold nanoshell composites used for initial validation

studies are described. Chapter 3 discusses the ability to load and release a range of cancer therapeutics from this material as well as validation of the system *in vitro* against a colon carcinoma cell line. Chapters 4-6 discuss synthesis of this composite material as injectable-sized particles using two different techniques. In Chapter 4, a templating method using a gelatin mold is used for particle synthesis, while Chapter 5 describes particle synthesis using controlled radical polymerization using surface initiated-atom transfer radical polymerization (SI-ATRP). Chapter 6 analyzes the ability to load and release drug from the SI-ATRP synthesized particles, as well as validation of the system *in vitro*. Chapter 7 investigates the ability of NIR irradiation of gold-silica nanoshells to induce cell membrane permeability, and exploits this mechanism for delivery of large biologic therapeutics (siRNA). Finally, concluding remarks are found in Chapter 8 along with recommendations for future studies.

2. Material Synthesis and Characterization[1]

The delivery platform developed in this dissertation consists of two material components: near-infrared absorbing gold-silica nanoshells and a thermally-responsive poly(NIPAAm-co-AAm)-hydrogel coating. The first portion of this chapter describes the properties of these two materials and discusses previous studies that have utilized these materials in cancer medicine. Additionally, the methods for the synthesis and the characterization of gold-silica nanoshells, bulk poly(NIPAAm-co-AAm) hydrogels, and bulk nanoshell-hydrogel composites are described herein. The gold-silica nanoshells described are used in all later chapters, and the bulk hydrogels and composites are also used in Chapter 3.

2.1. Gold Nanoparticles

Metal nanoparticles have been highly investigated for use in biological and medical applications due to their unique size and optical properties. In particular, gold-based nanoparticles provide a biocompatible surface layer, and well-established gold-thiol chemistries can be easily utilized for a variety of surface functionalizations. The four main gold nanoparticle types that will be further discussed are solid gold

---

[1] Portions of this chapter are adapted from:

Strong L.E., and West J.L. "Thermally Responsive Polymer-Nanoparticle Composites for Biomedical Applications." *Wiley Interdiscip Rev Nanomed Nanobiotechno*l. 3(3): 307-317 (2011).

Strong L.E., Dahotre S.N, and West, J.L. Hydrogel-nanoparticle composites for optically modulated cancer therapeutic delivery. *J. Control. Release.* 178(8): 63-68 (2014).

nanoparticles (AuNPs), gold nanorods (AuNRs), gold-gold sulfide (Au-Au_2S) nanoparticles, and gold-silica nanoshells, although a wide variety of shapes and formulations have been reported. These particles are of importance in biomedical applications because of their strong and tunable optical properties, which can be exploited to induce localized heating upon exposure to light. Additional properties of these particles are summarized in Table 2.1.

Table 2.1. Nanoparticle Properties. Adapted from (Strong and West, 2011).

Au Nanoparticles	**Au-Au_2S Nanoparticles**	**Silica-Au Nanoshells**	**Au Nanorods**
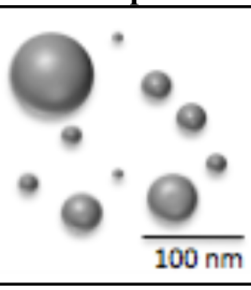	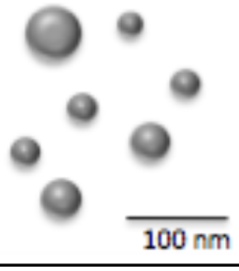	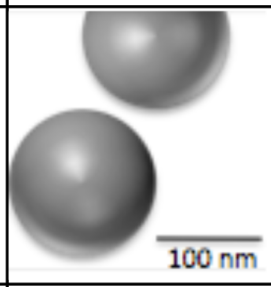	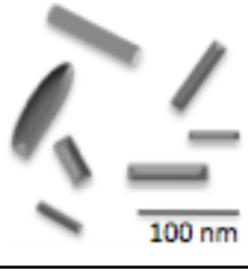
Diameter: 2-100 nm	**Diameter:** 30-40 nm	**Diameter**: 120-150 nm	**Aspect Ratio:** 1.5-10 (ex: 20x100 nm)
Extinction: 520-575 nm	**Extinction** (tunable): ~850 nm	**Extinction** (tunable): ~800 nm	**Extinction**: 600-1300 nm
Pros: highly investigated, ease of synthesis	**Pros:** NIR absorbance	**Pros:** NIR absorbance	**Pros:** NIR absorbance
Cons: extiniction coefficent near that of hemoglobin	**Cons:** synthesis byproduct of gold colloid	**Cons**: large	**Cons:** surfactant toxicity from synthesis

2.1.1. Optical Properties

The unique optical properties of gold nanoparticles have been investigated for many years, dating back to Michael Faraday's observation that gold colloids interact with light to produce a vibrant red color (Faraday, 1857). When these particles are exposed to

electromagnetic waves, the particles are set into motion by the electric field. If the frequency of incident light equals the natural frequency of the free vibrations in the particle, resonance occurs which is typically accompanied by a large amount of absorption.

2.1.1.1. Optical Absorption

The absorptive processes of gold-based nanoparticles are due to the surface plasmon resonance phenomena, in which exposure of an electric field of light at a particle's peak extinction (resonance condition) induces a coordinated oscillation of conduction band electrons (Figure 2.1), and this absorbed energy may be eventually dissipated as thermal energy, causing localized heating (Kelly et al., 2002). In addition to absorption, scattering of light may occur at frequencies not corresponding to the natural frequencies of the particle, and is discussed in more detail in the following section.

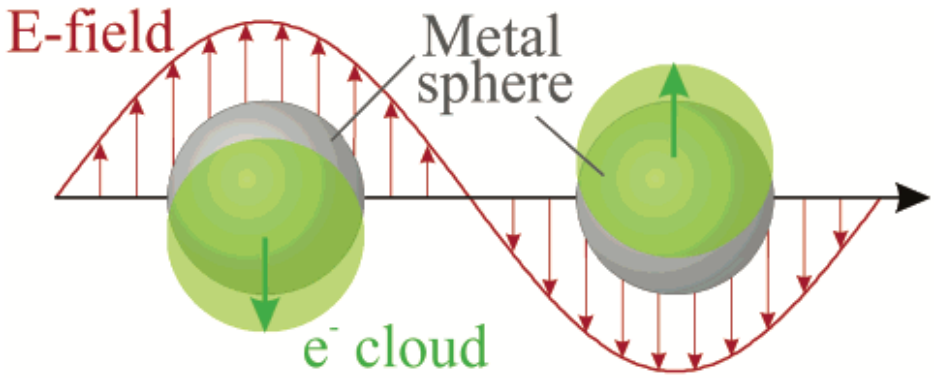

Figure 2.1. Diagram of surface plasmon resonance. Upon light irradiation, the electric field causes the conduction electron charge cloud to oscillate relative to the particle nuclei. From (Kelly et al., 2002).

2.1.1.2. Optical Scattering

In 1908, Mie theory was developed to describe the scattering properties of gold nanoparticles by solving Maxwell's equations of light scattering by gold colloids spherical or cylindrical shape, and was further modified to describe core/shell nanoparticles in 1951 (Aden and Kerker, 1951).

Mie theory may be used to describe the dependence of geometry on particle resonance for particles consisting with a dielectric core and gold shell (Averitt et al., 1999a). Assuming the total particle size is smaller than the wavelength of incident light ($r_2 << \lambda$), a quasi-static approximation can be used, which assumes spatial variations in the incident electromagnetic field are unchanging but still time dependent. Additionally, the particles are assumed to be perfectly spherical and any dipole-dipole interactions between adjacent particles are ignored as the particles are at a dilute concentration in solution. These equations are solved using the dielectric constants of the core (ε_1), shell (ε_2) and dispersive medium (ε_3), as well as the core radius (r_1) and total particle radius (r_2), as seen in Figure 2.2.

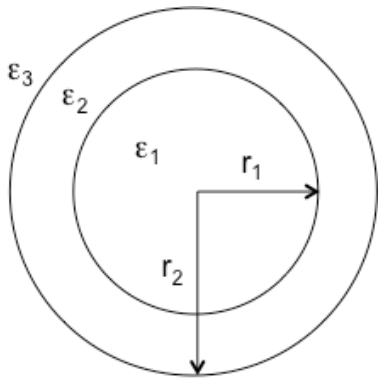

Figure 2.2. Nanoshell geometry used in Mie Theory calculations. Particles consist of a core radius (r_1) and total particle radius (r_2). The dielectric constants of the dispersive media, shell, and core are ε_3, ε_2, and ε_1 respectively.

The following equations, first described by Averitt et al., are important for describing the polarization behavior of conduction band electrons in the gold shell in response to light. First, Equation 2.1 describes the ratio of particle volume to shell volume (P):

$$P = 1 - \left(\frac{r_1}{r_2}\right)^3 \qquad \textbf{Equation 2.1}$$

Next, ε_a and ε_b are defined using the particle volume ratio as well as the dielectric constants of the various mediums:

$$\varepsilon_a = \varepsilon_1(3 - 2P) + 2\varepsilon_2 P \qquad \textbf{Equation 2.2}$$

$$\varepsilon_b = \varepsilon_2 P + \varepsilon_2(3 - P) \qquad \textbf{Equation 2.3}$$

With these values of ε_a and ε_b, the polarizability (α) of the particles can be described. This described the degree with which electrons in the outer shell are displaced from the particle mass in response to electromagnetic irradiation:

$$\alpha = 4\pi\varepsilon_0 r_2^3 \left[\frac{\varepsilon_2\varepsilon_a - \varepsilon_3\varepsilon_b}{\varepsilon_2\varepsilon_a + 2\varepsilon_3\varepsilon_b}\right] \qquad \textbf{Equation 2.4}$$

where ε_0 is the permittivity of free space ($8.85 \cdot 10^{-12}$ F/m). The resonance condition of a particle is obtained when the polarization (α) is maximal, and thus occurs as the real portion of the denominator in Equation 2.4 reaches 0. Assuming both the core and dispersive media are dielectric, i.e. $\mathrm{Im}(\varepsilon_1,\varepsilon_3) = 0$, a resonance condition as a function of wavelength can be obtained:

$$\frac{r_1}{r_2} = \left[1 + \frac{3}{2}\frac{\varepsilon_2'(\lambda)(\varepsilon_1 + 2\varepsilon_3)}{[\varepsilon_2'(\lambda)]^2 - \varepsilon_2'(\lambda)(\varepsilon_1 + \varepsilon_3) + \{\varepsilon_1\varepsilon_3 - [\varepsilon_2''(\lambda)]^2\}}\right]^{1/3} \qquad \textbf{Equation 2.5}$$

Thus, Equation 2.5 provides an expression relating the core radius: particle radius ratio needed to obtain a resonance condition at a particular wavelength. In fact, by adjusting r_1/r_2 from 0.6 to 0.9, the plasmon resonance of a particle shifts from 600 nm to over 1000 nm. These equations were originally developed to describe gold-gold sulfide nanoparticles (Averitt et al., 1999a), but may also be used to describe gold-silica nanoshells (Oldenburg et al., 1998). Figure 2.3 shows the optical tunability of gold-silica nanoshells using these parameters. Particles with a 120 nm silica core can be designed to have a peak extinction coefficient from near 700 nm to over 1000 nm by decreasing the shell thickness from 20 nm to 5 nm (Hirsch et al., 2006).

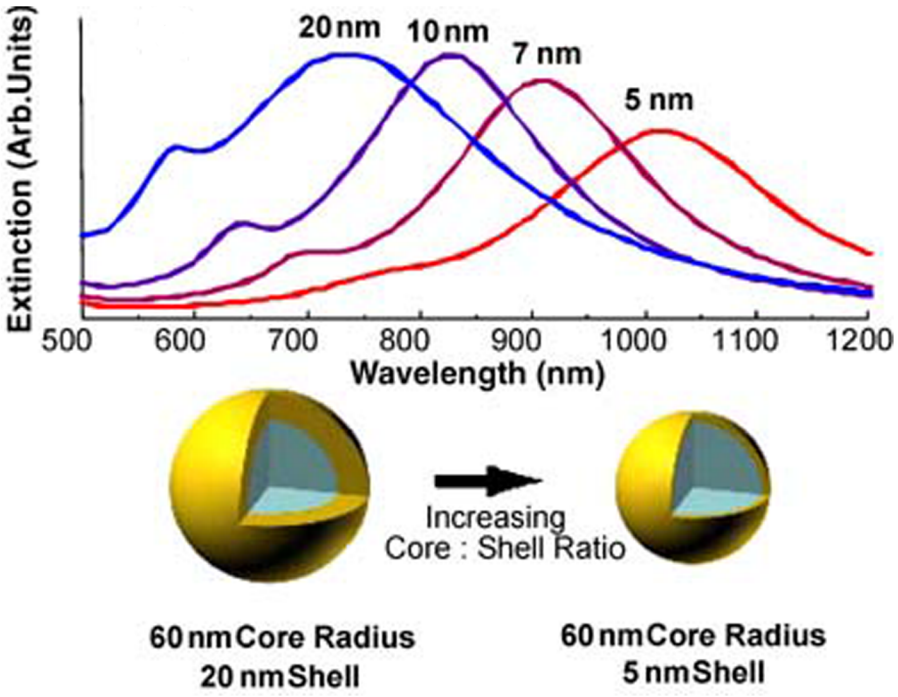

Figure 2.3. Optical tunability of gold-silica nanoshells. By altering gold-silica shell:core ratios, optical tunability can be obtained. A thinner shell causes a red shift in absorbance. Adapted from (Hirsch et al., 2006).

2.1.1.3. Optical Properties of Biological Tissue

In biological tissues, light absorption is mainly due to either water molecules or macromolecules such as proteins and pigments (Niemz, 2004). Water, the main constituent in most tissues, has a very small absorption coefficient in the visible range, but its absorption coefficient increases drastically starting at around 900 nm. In vascularized tissues, hemoglobin is the predominant macromolecule absorber, and has absorption peaks in the UV and visible spectrum, but its absorption drops off significantly around 650 nm.

Thus, the near-infrared (NIR) range (700-900 nm) is above the absorption of biological molecules such as hemoglobin (<650 nm) and below the range absorbed by water (>900 nm), as illustrated in Figure 2.3 (Weissleder, 2001).

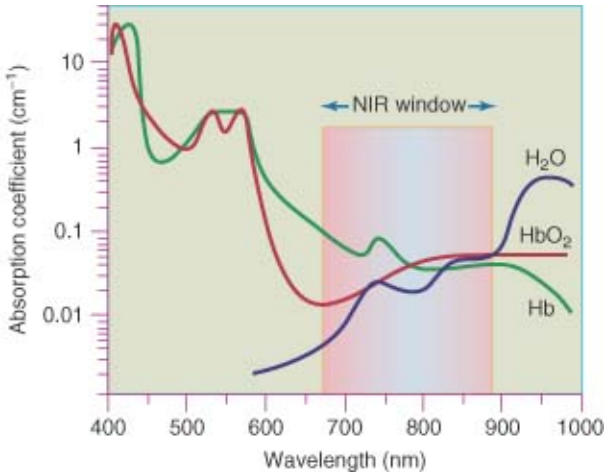

Figure 2.4. Tissue permeability of NIR light. Near-infrared light (650-900 nm) is of particular interest in biological applications as it is minimally absorbed by biological chromophores and water. From (Weissleder, 2001).

Therefore, these wavelengths may deeply penetrate biological tissue with relatively little attenuation or tissue damage. Gold-based nanoparticles including gold-gold sulfide nanoparticles, gold-silica nanoshells, and gold nanorods can all be tuned to have a peak extinction in the NIR range (Averitt et al., 1999b, Averitt et al., 1997, Hirsch et al., 2006, Yu et al., 1997).

2.1.2. Types of Gold Nanoparticles

Gold nanoparticles (AuNPs, also called gold colloids) are one of the most stable and highly investigated metal nanoparticle (Daniel and Astruc, 2004). These particles, thought of as "soluble gold" in antiquity, were used for aesthetic and curative purposes as early as the 4th and 5th centuries B.C. (Daniel and Astruc, 2004). Several synthesis

techniques exist, the most common being citrate reduction of chloroauric acid ($HAuCl_4$) in water (Turkevich et al., 1951). These particles (with diameters ranging from 2-100 nm) have maximum absorption around 520-575 nm, depending on the diameter of the particles, with the smaller particles maximally absorbing at lower wavelengths (Daniel and Astruc, 2004).

2.1.2.1. Gold Nanorods

Gold nanorods are anisotropic nanoparticles composed of solid gold, where particle shape strongly influences optical properties. Gold nanorods show a surface plasmon band near 520 nm similar to spherical AuNPs, but also have a second band at a longer wavelength (Mohamed et al., 1998). These optical properties are dependent on the particle's aspect ratio (ratio of length to diameter) (Yu et al., 1997). The dominant surface plasmon band occurs at a longer wavelength, and is based on the axial length of the particle (Yu et al., 1997). The secondary surface plasmon band occurs around 520 nm due to the weaker transverse resonance (Yu et al., 1997). Particles with larger aspect ratios will have the primary longitudinal resonance at a longer wavelength than particles with a smaller aspect ratio (Yu et al., 1997). These particles can be synthesized either by use of rigid templates or, more commonly, by use of seed and growth solutions in the presence of surfactants (Nikoobakht and El-Sayed, 2003).

2.1.2.2. Gold-Gold Sulfide Nanoparticles

Gold-gold sulfide nanoparticles were first developed by Zhou et al. (Zhou et al., 1994). Due to their optical properties, these particles were originally thought to consist of a dielectric gold sulfide (Au_2S) core surrounded by a thin gold shell (Averitt et al., 1997).

Controversy still remains over the exact structure of these particles; however optical simulations using Mie theory and surface conjugation studies suggest particles have a core/shell structure with a continuous gold coating (Averitt et al., 1999a, Gobin et al., 2010). These nanoparticles are synthesized by mixing a sulfur-based precursor (Na_2S or $Na_2S_2O_3$) with an excess of $HAuCl_4$ (Zhou et al., 1994, Averitt et al., 1997). The ratios of these two materials can be adjusted to alter surface plasmon resonance of the particles from 600 nm to greater than 1000 nm (Averitt et al., 1999a). Much research has been done on gold-gold sulfide nanoparticles that are NIR absorbing; these particles generally have a 35-55 nm diameter and surface plasmon resonance near 800-900 nm (Averitt et al., 1999a, Averitt et al., 1999b, Sershen et al., 2000, Gobin et al., 2010, Day et al., 2010).

2.1.2.3. Gold-Silica Nanoshells

Gold-silica nanoshells were first developed by Oldenburg et al. (Oldenburg et al., 1998). These particles consist of a dielectric silica core surrounded by a solid gold shell, and adjustments of these two parameters provides tunability of the optical properties of these particles, with thinner gold shells causing a red-shift in extinction spectra. Peak extinction coefficients of these gold-silica nanoshells can range from visible to near-infrared and even infrared ranges (Hirsch et al., 2006). Most photothermal studies have utilized particles with a 120 nm core and 10-15 nm shell, as this corresponds to a peak absorption coefficient in the near infrared range, where biological tissue is most permissive of light (Sershen et al., 2001, Sershen et al., 2002c, Sershen et al., 2005, Hirsch et al., 2003, Hirsch et al., 2006, Bikram et al., 2007, Kim and Lee, 2008, Day et al., 2009). Gold-silica nanoshells have been widely researched for applications in cancer

medicine due to their ease of synthesis and predicable optics, and were therefore chosen as the triggering component for the delivery platform developed in this dissertation.

2.1.3. Gold Nanoparticles in Cancer Medicine

Near infrared absorbing gold nanoparticles, particularly gold-silica nanoshells, have been investigated for both imaging and therapy applications in cancer medicine. This is due to numerous advantageous properties of the particles. First, the outer shell of these particles is made of reduced gold, a material known to be biocompatible due to its resistance of corrosion and low toxicity (Hirsch et al., 2006). Second, the size of these particles allows them to be injected intravenously and passively accumulate in tumor tissue due to the EPR effect (Matsumura and Maeda, 1986). Finally, the optical extinction of nanoshells involves both scattering and absorption components. The scattering properties of nanoshells can be harnessed for optical imaging of the particles using dark field microscopy, optical coherence tomography (OCT), or reflectance confocal microscopy (RCM) (Gobin et al., 2007, Loo et al., 2005, Coughlin et al., 2014). When these particles absorb light, the electron-photon interactions within the gold shell yield to heat dissipation and results in photothermal ablation of nearby cells (Hirsch et al., 2006). Photothermal therapy is advantageous for cancer management as cell death only occurs where both nanoshell accumulation and NIR light exposure occurs, minimizing off-site toxicity commonly seen in other cancer treatment modalities. A brief discussion of the use of gold-silica nanoshells for cancer therapy follows.

2.1.3.1. *In vitro* Studies

Photothermal therapy using gold-silica nanoshells was first demonstrated by Hirsch et al. in 2003 (Hirsch et al., 2003). In this study, SK-BR-3 human breast carcinoma cells were incubated with gold-silica nanoshells and exposed to an NIR laser. Cells that were incubated with nanoshells exhibited a loss in viability upon NIR exposure, whereas cells without nanoshells had no loss in viability (Hirsch et al., 2003).

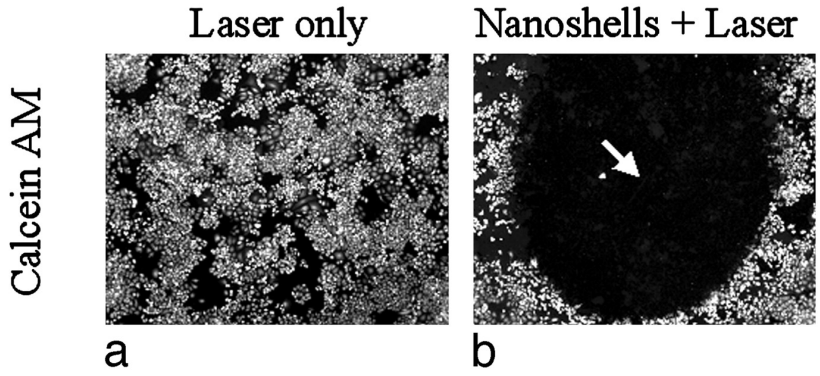

Figure 2.5. *In vitro* validation of photothermal therapy. [A] Cells irradiated in the absence of nanoshells maintained viability as determined by Calcein AM staining. [B] Cells irradiated in the presence of nanoshells showed a circular zone of cell death indicated by a lack of Calcein AM staining. Adapted from (Hirsch et al., 2003).

Further *in vitro* studies have focused on active targeting of nanoshells using antibodies and other protein based ligands including anti-HER2 (Loo et al., 2005, Lowery et al., 2006, Bernardi et al., 2008), anti-IL13Rα2 (Bernardi et al., 2008), ephrinA1 (Gobin et al., 2008), and VEGF (Day et al., 2012). Gold colloids (Pitsillides et al., 2003), gold-gold sulfide nanoparticles (Gobin et al., 2010, Day et al., 2010) and gold nanorods (Huang et al., 2006) have also been investigated for photothermal therapy potential *in vitro*, displaying similar results as gold-silica nanoparticles.

2.1.3.2. *In vivo* Studies

Photothermal therapy has been further evaluated in several *in vivo* studies, most commonly in mouse models. In the first study by Hirsch et al., transmissible venereal tumor (TVT) cells were inoculated in the hind leg of SCID mice and grown to a diameter of ~1 cm (Hirsch et al., 2003). Poly(ethylene glycol) (PEG)-passivated gold silica nanoshells were injected interstitially at the tumor site. Nanoshells are often coated with polymer chains such as PEG, as this has been shown to minimize plasma protein adsorption and therefore increase *in vivo* circulation time of the particles. Next, tumor sites were exposed to 820 nm light at 4 W/cm^2, and temperature profiles were obtained using phase-sensitive, fast spoiled gradient-echo MRI for thermal imaging. Results showed an average temperature increase of 9.1±4.7 ^oC, and gross pathology indicated tissue damage and hemorrhaging.

Not all tumor sites will be amenable to having direct injection of particles into the tumor. Further studies have shown the ability of gold-silica nanoshells to be injected intravenously, circulate throughout the body, and passively accumulate in tumor tissue via the EPR effect. In the first of such studies by O'Neal et al., PEGylated gold-silica nanoshells were injected into the tail vein of mice with a subcutaneous tumor (O'Neal et al., 2004). The tumor was exposed to an 808 nm diode laser 6 hours post-injection. In addition, a "sham" group received a saline injection followed by laser treatment, and a control group received no treatment. Figure 2.6 shows a Kaplan-Meyer survival plot for the three groups, with all mice in the nanoshell-assisted photothermal therapy (NAPT) group surviving for the 60 day period, whereas the mean survival for the control and

sham groups were 10.1 days and 12.5 days respectively. Further *in vivo* studies have investigated NAPT as a potential treatment for malignant glioma (Day et al., 2011, Day et al., 2012).

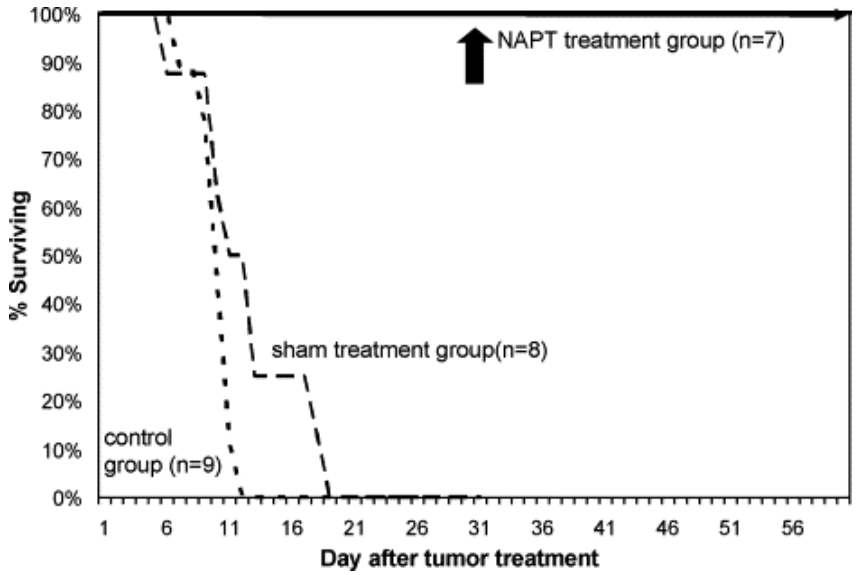

Figure 2.6. Survival curve from NAPT. NAPT mice showed 100% survival after 60 days, while the sham and control groups had an average survival of 12.5 and 10.1 days respectively. From (O'Neal et al., 2004).

Studies of the biodistribution and clearance of gold-silica nanoshells indicate that the particles are primarily cleared via the liver and spleen (James et al., 2007). At 24 hours post injection, there are higher nanoshell concentrations in the tumor versus most other tissues. Eventually these particles are cleared by the reticuloendothelial system (RES) primarily through the liver and spleen, and no toxicities or bioincompatibilities have been seen up to 404 days post injection (Gad et al., 2012).

Due to the promise shown in these *in vivo* studies, photothermal therapy with gold-silica nanoshells is currently in FDA clinical trials for refractory head and neck cancer as well as primary and metastatic lung cancer (Nanospectra Biosciences, 2014). In

this treatment, nanoshells are injected intravenously, allowed to passively accumulate in the tumor, and then the tumor site is exposed to NIR light from a fiber optic probe (Nanospectra Biosciences, 2014).

2.1.3.3. Multimodal Particles

The inherent ability of gold-silica nanoshells to both scatter and absorb light allows for a single particle platform to be used for both diagnostic purposes (imaging) and therapy (photothermal ablation). These particles have been used for contrast agents for a variety of imaging techniques. Gobin et al. demonstrated that gold-silica nanoshells can be used for both contrast agents for OCT and photothermal therapy simultaneously (Gobin et al., 2007). In addition to their scattering properties, gold-silica nanoshells also exhibit two-photon induced photoluminence, allowing utilization of two-photon microscopy for analysis of nanoparticle distribution in tumor tissue (Park et al., 2008). Additionally, Coughlin et al. endowed gold-silica nanoshells with magnetic properties by conjugation of gadolinium chelates, thus creating a single particle platform providing MR contrast, optical contrast, and photothermal therapy (Coughlin et al., 2014).

2.2. Thermally Responsive Polymers

The gold-silica nanoshells previously described will provide the stimulus for drug release from a hydrogel coating. Stimuli-responsive ‘smart’ polymers undergo fast, reversible conformational changes in response to small changes in the environment (Galaev and Mattiasson, 1999). These changes typically involve the polymer microstructure transitioning between a hydrophilic and hydrophobic state, altering chain conformations leading to macroscopic material size and properties changes (Galaev and

Mattiasson, 1999). Systems responsive to local chemical changes, such as changes in pH, as well as systems responsive to external stimuli, such as ultrasound, light, or temperature, have been studied (Bikram and West, 2008). Commonly studied temperature-sensitive polymers include acrylamide-based hydrogels, especially poly(NIPAAm), as well as elastin-like polypeptides (ELPs) (Galaev and Mattiasson, 1999, Meyer et al., 2001b, Chilkoti et al., 2002, Bikram and West, 2008).

Many temperature-sensitive polymers display lower critical solution temperature (LCST) behavior, in which a reversible volume phase transition occurs. At lower temperatures, it is thermodynamically favorable for water molecules to form hydrogen bonds with polar groups on the polymer chains, causing the hydrogel to be in a swollen state. At higher temperatures, there is an increase in Gibbs free energy (ΔG), and hydrogen bonding between the water molecules and polymer chains becomes thermodynamically unfavorable compared to polymer-polymer and water-water interactions (Schild, 1992). This causes the water to move into bulk solution and the polymer chains to collapse onto themselves forming hydrophobic interactions (Sasak et al., 1996).

2.2.1. N-isopropylacrylamide and Other Acrylamides

Poly(N-isopropylacrylamide) is a widely studied thermally-responsive polymer that exhibits an LCST near physiologic temperatures (Bikram and West, 2008). Pure poly(NIPAAm) hydrogels have an LCST range of 25-32 ^{o}C, and by incorporating a more hydrophilic comonomer into the hydrogel, this LCST can be raised to near 45-50 ^{o}C (Yoshida et al., 1994). Common comonomers used include acrylamide (AAm) or acrylic

acid (AAc). In addition, incorporation of N-isopropylmethacrylamide (NIPMAAm) increases the LCST as the steric hinderance associated with the additional methyl group inhibits the phase transition (Keerl et al., 2008). In contrast, hydrogels consisting of hydrophilic acrylamide/acrylic acid monomers exhibit a positive volume change with increasing temperatures (Owens et al., 2007a, Owens et al., 2007b). The chemical structures of these various acrylamides are described Figure 2.7.

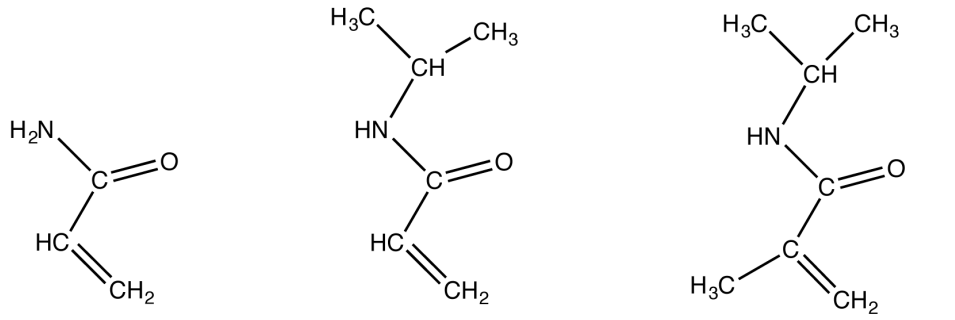

Figure 2.7. Chemical structures of various acrylamides.

2.2.2. Elastin-Like Polypeptides

Another widely researched thermally-responsive polymer material is elastin-like polypeptides (ELPs), which are synthetic peptides derived the hydrophobic domain of tropoelastin (Urry, 1997). ELPs generally consist of oligiomeric repeats of the pentapeptide VPGXG (where X is any amino acid except proline) (Urry, 1997). By using recombinant methods to synthesize these polymers, a monodisperse product with little batch-to-batch variability can be achieved, which is highly advantageous over synthetic polymeric materials (Meyer et al., 2001b, Chilkoti et al., 2002, Bikram and West, 2008).

By altering amino acid sequence or number of repeats, ELP LCSTs (also commonly called transition temperatures, or T_t) are highly tunable and can be brought to above physiologic temperatures (Meyer et al., 2001a, Chilkoti et al., 2002, Meyer et al., 2001b). ELPs are commonly synthesized by inducing the expression of a genetic sequence that encodes these repetitive polypeptides in *E. coli* and then purifying the peptide product. This is commonly done through a process known as recursive directional ligation (RDL), which allows the synthesis of large, repetitive genes (Chilkoti et al., 2002). Additionally, these materials can be designed such that they can assemble into crosslinked hydrogel networks (Asai et al., 2012).

2.2.3. Thermally-Responsive Polymers in Cancer Medicine

Many of the first comprehensive studies of a thermally responsive polymer being used in cancer medicine studies come from the Chilkoti group (Meyer et al., 2001b, Meyer et al., 2001a, Dreher et al., 2003, Furgeson et al., 2006, Liu et al., 2006, Dreher et al., 2007, MacKay et al., 2009, Liu et al., 2010). ELP chains may be conjugated to hydrophobic chemotherapeutic drugs to drive self-assembly into macromolecule complexes. Such complexes improve chemotherapeutic administration by (1) increasing the overall accumulation in solid tumors, (2) distributing drug homogenously throughout tumor tissues, and (3) increasing intracellular localization of these therapeutics (MacEwan et al., 2010). The first of such studies, published in 2001, showed that ELPs conjugated to drugs could be thermally targeted to solid tumors (Meyer et al., 2001a). ELPs were designed to have a T_t of ~41 ^{o}C, such that these particles would remain soluble in solutions below their T_t (such as at physiologic temperature), but then become

insoluble and aggregate at solution temperatures above 41 ^{o}C. These particles were injected intravenously and circulated throughout the body at 37 ^{o}C. However, if localized hyperthermia treatments were used to heat a solid tumor, these particles became insoluble and aggregated, resulting in increased tumor accumulation (Meyer et al., 2001a). Similar results have been seen in additional studies (Liu et al., 2006) and additional analysis shows that thermal cycling of the tumor between 37^{o}C and 41 ^{o}C further enhances ELP accumulation (Dreher et al., 2007).

A similar study compared the ability to target both thermally responsive ELPs and thermally responsive poly(NIPAAm-co-AAm) to tumors (Meyer et al., 2001b). In this study, both the ELP and poly(NIPAAm-co-AAm) used were tuned to have an LCST at 40 ^{o}C. This was accomplished by substituting Ala and Gly residues for the more hydrophobic Val at the fourth position of the ELP pentipeptide, and by using an 84:16 ratio of NIPAAm:AAm in the poly(NIPAAm-co-AAm). Heating did increase accumulation of both thermally responsive carriers in the tumor over both controls; however, the ELP displayed enhanced accumulation in tumors over the polymer. The authors speculate that this may be because the LCST of poly(NIPAAm) and its copolymers can only be tailored to a limited extent by altering incorporation of comonomers, chain length, sequence, and stereochemistry; whereas ELPs genetic control allows for more precise tuning of chemical properties such as transition temperature (Meyer et al., 2001b).

A study by MacKay et al. analyzed the *in vivo* efficacy of an ELP-like drug carrier loaded with the chemotherapeutic doxorubicin (MacKay et al., 2009). These

carriers, called chimeric polypeptides (CPs), consisted of two segments: a biodegradable ELP segment and a short doxorubicin attachment segment. These particles self-assemble into sub-100 nm nanoparticles upon drug attachment, as seen in Figure 2.8. Particles were injected into a BALB/c subcutaneous mouse tumor model via a tail vein injection (5 mg doxorubicin equivalent/kg). After 24 hours post-administration, tumor tissue had a 3.5-fold increase in doxorubicin concentration for the CP-doxorubicin group compared to the free doxorubicin group. In addition, the CP-doxorubicin group showed decreased doxorubicin concentration in several tissue sites known to be affected by doxorubicin side effects, including the muscle, lung, and heart (MacKay et al., 2009).

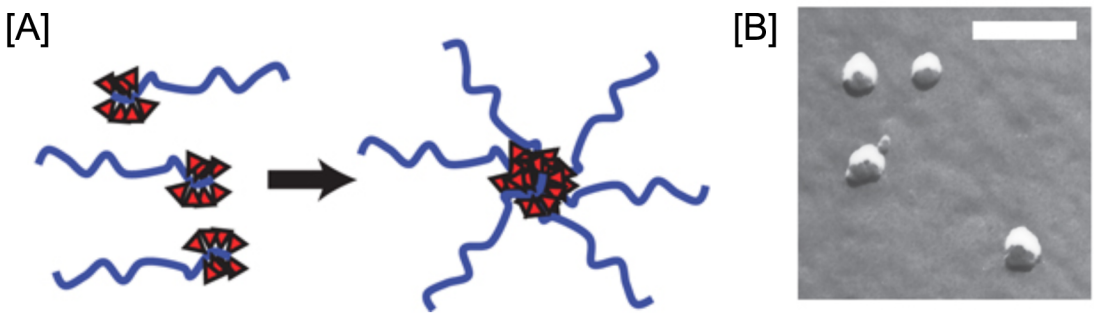

Figure 2.8. Self assembly of CP-doxorubicin nanoparticles. [A] After conjugation of doxorubicin (red triangles) to chimeric polypeptides (blue lines), these particles self assemble into micelles in aqueous environments. [B] These micelles are smaller than 100 nm, as demonstrated by freeze-fracture TEM (scale bar = 200 nm). Adapted from (MacKay et al., 2009).

It is interesting to note that this study did not utilize the thermal properties of the CP particles. A further study investigated a similar CP-doxorubicin material designed to transition from nanoscale micelles to microscopic aggregates upon mild hyperthermia (39-42 ^{o}C), as to allow for thermal targeting (McDaniel et al., 2012). Additional studies

have investigated drug conjugation to ELPs through acid-labile hydrazine bonds for drug release within the acidic environment of lysosomes (Dreher et al., 2003, Furgeson et al., 2006), the effect of ELP-radionuclide conjugates on tumor progression (Liu et al., 2010), active targeting of complexes to tumor tissue using a CD13 targeting peptide (Simnick et al., 2011), and synthesizing complexes which respond to multiple stimuli (including temperature pH, and cosolutes) (Callahan et al., 2012). Additionally, other groups have looked at ELPs as delivery vehicles for short peptides to disrupt transcriptional functions (Bidwell and Raucher, 2005), and micelle formation by combining poly(NIPAAm)-chains and the chemotherapeutic 5-fluorouracil (Zhang et al., 2012).

2.3. Thermally Responsive Polymer-Nanoparticle Composites

Thermally responsive polymer-metal nanoparticle composites couple the ability of certain metal nanoparticles to convert external stimuli to heat with polymers that display sharp property changes in response to temperature changes, allowing for external control over polymer properties. These systems have been investigated for a variety of biomedical applications, including drug delivery (Sershen et al., 2000, Sershen et al., 2002a, Bikram et al., 2007, Satarkar and Hilt, 2008), microfluidic valve (Sershen et al., 2002b, Sershen et al., 2005, Satarkar et al., 2009) and microlens (Kim et al., 2005) control. Additionally, the effects of these encapsulated nanoparticles on polymer bulk properties have been studied (Wang et al., 2004b, Wang et al., 2004a).

2.3.1. Microfluidic Valves

Due to remote triggering of dramatic changes in material size and shape, thermally responsive polymer-nanoparticle conjugates have been investigated for use in

the controlled manipulation of valves in microfabricated devices. Sershen et al. proposed a combination of poly(NIPAAm-co-AAm) hydrogels, gold colloid particles, and gold-silica nanoshells for use in independent control of multiple valves within a microfluidic device, as seen in Figure 2.9 (Sershen et al., 2002b, Sershen et al., 2005). Using these materials, independent control of two valves at a T-junction was achieved. One valve consisted of a poly(NIPAAm-co-AAm)-gold colloid composite while the other contained a poly(NIPAAm-co-AAm)- gold-silica nanoshell composite. When exposed to green (532 nm) light, the gold colloid channel opened and the gold-silica remained closed, but when exposed to NIR (832 nm) light, the gold-silica channel opened while the gold-colloid channel remained closed (Sershen et al., 2005). The authors noted that a larger number of independently controlled components could be achieved by using multiple nanoparticles with different absorption spectra, utilizing directed light, or tailoring the hydrogels to have differing LCSTs (Sershen et al., 2005).

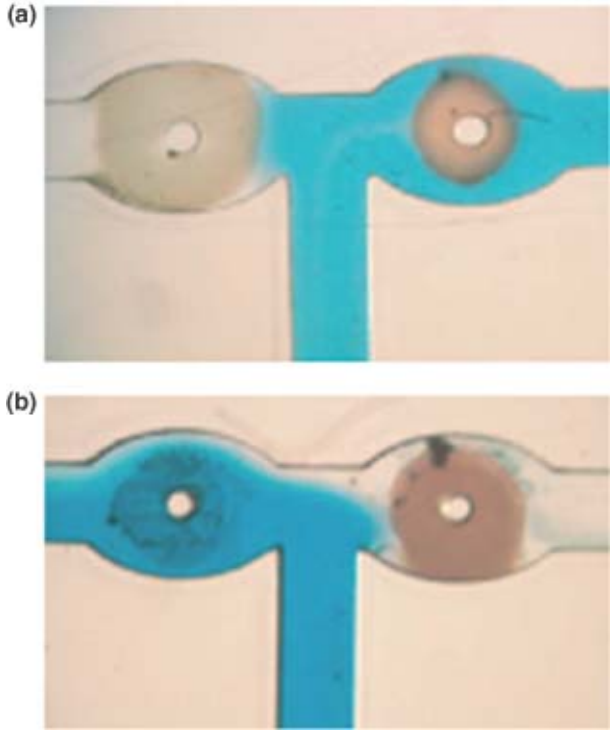

Figure 2.9. T junction in a microfluidic device formed by two valves; one made with a gold colloid nanocomposite hydrogel and one made of a gold nanoshell composite hydrogel. [A] After the entire device is illuminated with 532 nm light for 5 s, the gold colloid channel opens and the gold nanoshell remains closed [B] The opposite response is seen when the device is illuminated with 832 nm light. From (Sershen et al., 2005).

2.3.2. Drug Delivery

Photothermally modulated drug delivery was first shown by Sershen et al. using a combination of poly(NIPAAm-co-AAm) and gold-gold sulfide nanoparticles (Sershen et al., 2000). This study used hydrogels with a 95:5 molar ration of NIPAAm:AAm to achieve an LCST slightly above physiologic temperature. Upon NIR irradiation of these composites, the temperature of the hydrogel exceeds the LCST causing a burst release of any soluble molecules contained in the hydrogel matrix. Enhanced release of molecules such as methylene blue, ovalbumin, and bovine serum albumin was found to follow near infrared irradiation of the nanoparticle-composite hydrogels (Sershen et al., 2000).

Further investigation of this system showed that it could be applied to photothermal delivery of insulin (Sershen et al., 2002a). A similar system using the same hydrogel formation with gold-silica nanoshells also successfully demonstrated photothermal drug delivery (Bikram et al., 2007). Studies showed that the collapse of hydrogel-nanoshell composites was controlled by both laser fluence and gold-silica nanoshell concentration (Bikram et al., 2007). Photothermal release studies of methylene blue, insulin and lysozyme showed a pulsatile drug release that was dependent on the molecular weight of the molecule (Bikram et al., 2007).

The optically-triggered cancer therapeutic delivery platform developed in this dissertation builds upon these successful studies utilizing poly(NIPAAm-co-AAm)-gold nanoshell composites. The methods used to synthesize and characterize these bulk poly(NIPAAm-co-AAm)-gold nanoshell composites are outlined in the remainder of this chapter, and initial validation of these materials to deliver cancer therapeutics is described in Chapter 3.

2.4. Materials and Methods

All reagents were purchased from Sigma-Aldrich and used as received, unless otherwise noted. All water used in synthesis, purification, and testing was treated by a Milli-Q system (≥18.0 MΩ·cm resistivity).

2.4.1. Gold-Silica Nanoshell Synthesis

Gold-silica nanoshells are synthesized using a four-step process that is outlined in this paragraph, with details to follow. First, silica nanoparticles are formed using the Stöber method, and then surface functionalized with amine groups using silane reagents.

Small gold colloid particles (~2 nm) are then adsorbed onto the aminated surface. These served as nucleation sites for a final reduction step in chloroauric acid, potassium carbonate, and formaldehyde, producing a gold shell around the silica particle. This synthesis process is summarized in Figure 2.10, accompanied by a TEM micrograph depicting shell growth (Oldenburg et al., 1998).

For the first step of silica nanoparticle formation via the Stöber method (Stober et al., 1968), tetraethyl orthosilicate (TEOS) was reduced in ethanol (EtOH) in the presence of ammonium hydroxide (NH_4OH). To achieve nanoparticle diameters of approximately 120 nm, 0.5 g of NH_4OH (28%) was added to 32.06 g 200 proof EtOH. With rapid stirring, 1.69 g of TEOS (99.999%) was added. The reaction mixture was rocked overnight at room temperature. The following day the particles were washed by three rounds of centrifugation (2500 x g, 30 min) and suspended in EtOH. The silica particles were then functionalized with amine groups via a reaction with 3-aminopropyltriethoxysilane (APTES). For every 1 ml of cores at 4 wt%, 5 µl of APTES (Gelest, Inc.) was added under rapid stirring and allowed to react overnight at room temperature. The following day, the reaction solution was boiled for 2 hr to ensure surface exposure of amine groups. The suspension was then centrifuged three times (2500 x g, 30 min) and resuspended in EtOH.

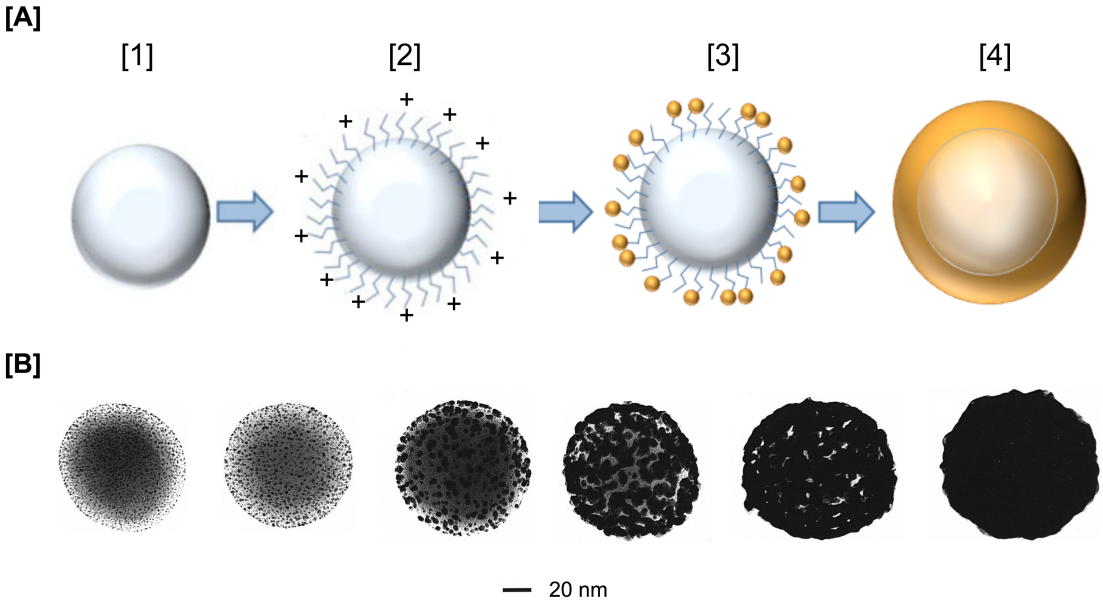

Figure 2.10. Gold-silica nanoshell synthesis. [A] The four steps of gold-silica nanoshell synthesis: (1) formation of silica core, (2) amine functionalization, (3) adsorption of gold colloid and (4) shell growth. [B] TEM image depicting shell growth on a silica core from adsorbed gold colloid (steps 3-4 from [A]). Adapted from (Oldenburg et al., 1998).

Colloidal gold particles with a 2-4 nm diameter were prepared by a reduction of chloroauric acid ($HAuCl_4$) as previously described in the literature (Duff et al., 1993). Briefly, a tetrakis(hydroxymethyl)phosphonium chloride (THPC, TCI America, 80%) solution was made by mixing 400 µl of THPC with 33 ml H_2O. Next, 4 ml of this THPC solution was added to 1.2 ml of 1 N sodium hydroxide (NaOH) and 180 ml of H_2O. This solution was rapidly stirred for at least 5 min, and then 6.75 ml of 1 wt% $HAuCl_4$ (Alfa Aesar, 99.999%) was added. The mixture was stirred until the suspension color stabilized (<1 min) and the product was stored at 4 ^{o}C. Generally this colloid suspension was aged for at least 2 weeks before being used in subsequent steps.

Aminated silica core particles were then mixed with this gold colloid suspension to create "seed" particles with the colloids being adsorbed onto the silica core via electrostatic interaction between the positively charged amine group and negatively charged colloids. For this reaction, 30 ml of colloid suspension was mixed with 180 μl functionalized cores (at 4 wt%) and 1 ml of 1 M NaCl. The reaction mixture was rocked for at least 48 hr at room temperature and washed by two rounds of centrifugation (1500 x g, 30 min) and resuspended in H_2O.

Nanoshell synthesis was completed by a shell growth step. A gold plating solution was made by combining 200 mg of potassium carbonate (K_2CO_3), 12 ml of 1% $HauCl_4$, and 800 ml H_2O. Various seed particle volumes (200-500 μl) were added to 1 ml of the plating solution. 10 μl of formaldehyde (HCHO, 37%) was added to each suspension with rapid mixing. This causes a reduction reaction in which the adsorbed colloids of the seed particles serve as nucleation sites for shell growth via deposition of reduced gold ions. Formulations that produced particles with an extinction profile peak near 800 nm were linearly scaled up. After synthesis, nanoshells were washed by one round of centrifugation (735 x g, 10 min) and resuspended in 1.81 mM K_2CO_3 for storage. Before use in subsequent applications, stored nanoshells were washed via one centrifugation round (735 x g, 10 min) and resuspended in H_2O.

After synthesis, particle extinction spectra from 400-1000 nm were collected using a Cary 50 Varian spectrophotometer. Nanoshells were also characterized by electron microscopy with an FEI Tecnai G^2 Twin transition electron microscope (TEM).

Additionally, dynamic light scattering (DLS) was then used to measure the hydrodynamic diameter of the particles using a Malvern Zetasizer ZS.

2.4.2. Poly(NIPAAm-co-Aam) Hydrogel Synthesis

Poly(NIPAAm-co-Aam) hydrogels were synthesized using free radical-initiated addition polymerization. Prior to synthesis, NIPAAm (97%) was dissolved in tetrahydrofuran (THF) and recrystallized in *n*-hexane to remove the small molecule inhibitor *p*-methoxyphenol from the packaged NIPAAm. The recrystallization process was repeated at least 3 times and the final product was dried under vacuum and stored at -20 ^{o}C. Stock solutions of NIPAAm (1.75 M), AAm (≥99%, 15 M), and *N,N'*-methylenebisacrylamide (MBAAm) (≥98%, 0.169 M) were prepared in water. A prepolymer solution of a 95:5 molar ratio of NIPAAm:AAm and a 1:750 molar ratio of monomer:crosslinker (MBAAm) was prepared from the stock solutions: 3.56 ml 1.75 M NIPAAm, 21.88 µl 15 M AAm, and 51.78 µl 0.169 M MBAAm and 116.34 µl H_2O were added to a three-neck round bottom flask (3.75 ml total). Argon (Ar) gas was bubbled through this solution for at least 15 min in order to remove dissolved O_2, which inhibits the polymerization process. With rapid stirring, 37.5 µl of 10% (w/v) ammonium persulfate (APS, ≥98%) in H_2O and 7.5 µl of *N*,*N*,*N*′,*N*′-tetramethylethylenediamine (TEMED, ≥99%) were added to initiate the redox reaction for free radical polymerization. To synthesize composite hydrogels, nanoshells were added to a concentration of 8 x 10^9 nanoshells/ml to the monomer solution prior to adding APS/TEMED. The polymerization solution was then quickly poured into a mold consisting of 2 glass slides separated by a 1.5 mm Teflon® spacer held together by metal

clamps. The hydrogel was then cured at 30 ^{o}C for 2 h. After curing, the hydrogel slab was soaked in 95% EtOH for at least 12 hr followed by H_2O for at least 12 hr to remove any initiators and unreacted monomers. Hydrogel disks (4 mm diameter) were punched out of the hydrogel slab with a cork borer. A schematic of this polymerization process is shown in Figure 2.11.

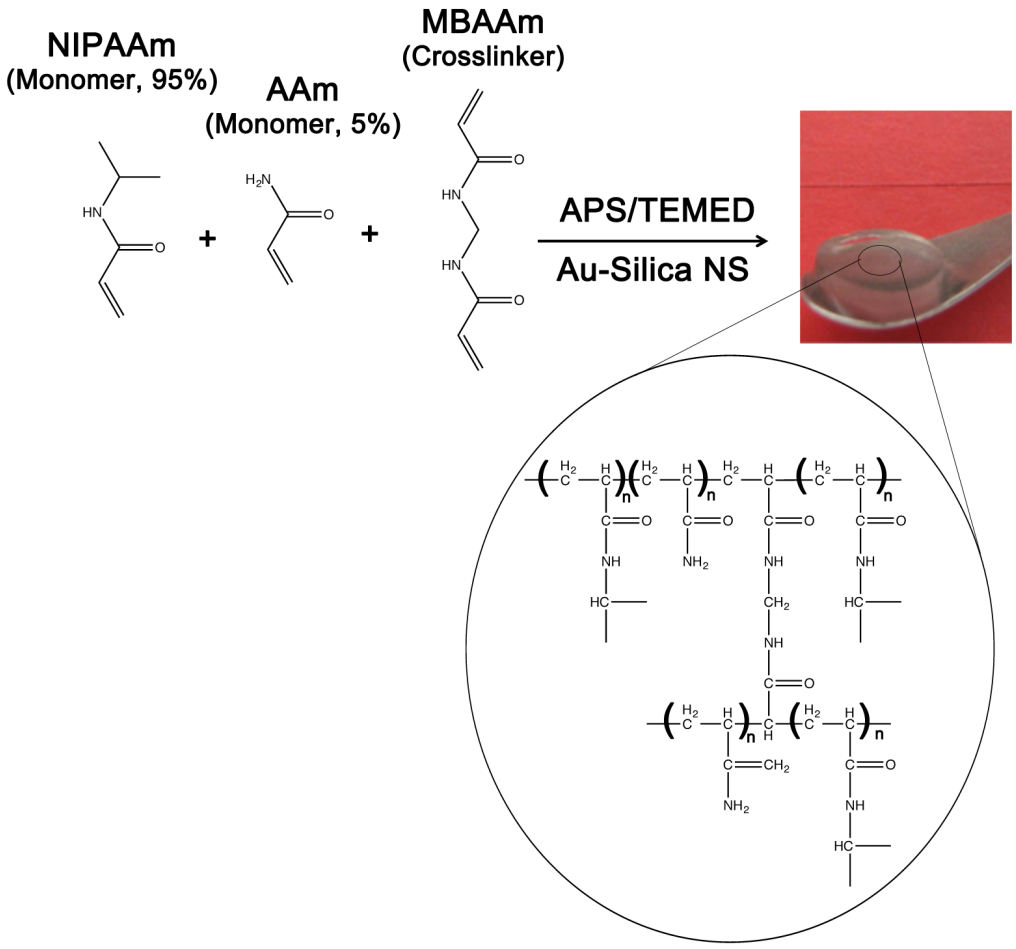

Figure 2.11. Poly(NIPAAm-co-AAm) hydrogel synthesis. A solution of a 95:5 molar ratio of the monomers NIPAAm:AAm and a 1:750 ratio of crosslinker MBAAm:monmers is polymerized by free radical polymerization initiated by APS and TEMED.

2.4.3. Poly(NIPAAm-co-AAm) Hydrogel Morphology and Mesh Size

Differences in the mesh size of poly(NIPAAm-co-AAm) hydrogels and poly(NIPAAm-co-AAm)-nanoshell composite hydrogels were assessed using a method similar to that used by Weber et al. (Weber, Lopez, and Anseth 2009). Hydrogels of a 4 mm diameter and 2 mm height were dried under vacuum overnight and then soaked in a 1 mg/ml solution of trypsin inhibitor (MW = 20,000 Da) in phosphate-buffered saline (PBS, pH 7.4) for 48 hr at 4 ^{o}C. Hydrogels were then placed in fresh PBS and release of the trypsin inhibitor was analyzed over 120 min by taking aliquots of the soak solution and analyzing for protein content using a Micro BSA Protein Assay (Thermo Scientific). To determine the diffusion coefficient of the protein through the hydrogel, the release profiles were fit to Equation 2.6 (Crank 1975):

$$\frac{M_t}{M_\infty} = 1 - \frac{6}{\pi^2}\sum_{n=1}^{\infty}\frac{1}{n^2}\exp\left(-\frac{Dn^2\pi^2 t}{a^2}\right) \qquad \textbf{Equation 2.6}$$

where M_t is the amount of protein that has diffused out of the hydrogel at time t; M_∞ is the amount of protein that has diffused out after time equals infinity (here estimated after 72 hr), D is the diffusion coefficient of the protein through the hydrogel, and a is the radius of the hydrogel (4 mm).

The mesh size of the hydrogel networks (ξ) is related to the diffusion coefficient of a given solute by Equation 2.7:

$$\frac{D_g}{D_o} = \left(1 - \frac{r_s}{\xi}\right)\exp\left(-\Upsilon\left(\frac{v_2}{1 - v_2}\right)\right) \qquad \textbf{Equation 2.7}$$

where D_g is the diffusion coefficient of the solute through the hydrogel calculated from Equation 2.3, D_o is the diffusion coefficient of the solute in solution (1.45 cm^2/s x 10^6) (Weber et al., 2009), r_s is the solute (trypsin inhibitor) radius (2.19 nm) (Weber et al., 2009), Υ is the ratio of the volume required for translational movement of the solute to the average free volume per liquid molecule, and is generally approximated to be 1, and v_2 is the volumetric swelling ratio (Weber et al., 2009). The volumetric swelling ratio was calculated using Equation 2.8:

$$v_2 = 1 + \frac{\rho_c}{\rho_s}\left(\frac{M_s}{M_d} - 1\right) \qquad \textbf{Equation 2.8}$$

where ρ_c and ρ_s are the densities of the composite material and solvent, respectively; and M_s and M_d are the swollen and dry masses of the hydrogel, respectively.

2.4.4. Poly(NIPAAm-co-AAm) Hydrogel Deswelling

The swelling behavior of the poly(NIPAAm-co-AAm) gels was analyzed in response to changes in temperature. The hydrogels were allowed to swell at room temperature (22 ^oC) for at least 24 hr before testing. To determine the LCST of the hydrogels, the gels were first weighed and placed in TRIS-buffered saline (TBS, pH 7.4) and then incubated at various temperatures (29 ^oC, 33 ^oC, 37 ^oC, 41 ^oC, 45 ^oC, and 50 ^oC) for 10 min. After incubation, the gels were weighed again and the deswelling of the gel was calculated using Equation 2.9.

$$Deswelling\ Ratio\ (\%) = 100 * {Weight_{Temp}}\Big/{Weight_{Temp= 22^oC}} \qquad \textbf{Equation 2.9}$$

Additionally, the thermal behaviors of hydrogels with and without nanoshells were compared. These gels were either incubated at 50 ^oC or exposed to an NIR laser and

weighed at various times. For this test, gels were placed in 2 ml TBS and incubated in a 50 ^{o}C water bath. Gels were weighed every 10 min for 30 min and the deswelling of the gel was calculated using Equation 2.10.

$$Deswelling\ Ratio\ (\%) = 100 * {Weight_t}/{Weight_{t=0}} \quad \textbf{Equation 2.10}$$

The thermal behavior of gels with and without nanoshells in response to NIR irradiation was then analyzed. Gels were placed in 2 ml of TBS and exposed to an NIR laser (Coherent Diode, 808 nm, 8 W/cm^2, 30 min). The gels were weighed every 10 min for 30 min and the deswelling of the gel was calculated using Equation 2.10.

2.5. Results

2.5.1. Gold-Silica Nanoshell Characterization

As synthesized, the nanoshells utilized in this study were found to have a diameter of 153 ± 9 nm (as analyzed by TEM) and a Z-average diameter of 156.0 nm and a polydispersity index of 0.090 (as analyzed by DLS). These particles strongly absorb in the near infrared (NIR), with a peak extinction coefficient at 780 nm. A TEM image of the gold-silica nanoshells and their extinction spectra are shown in Figure 2.12.

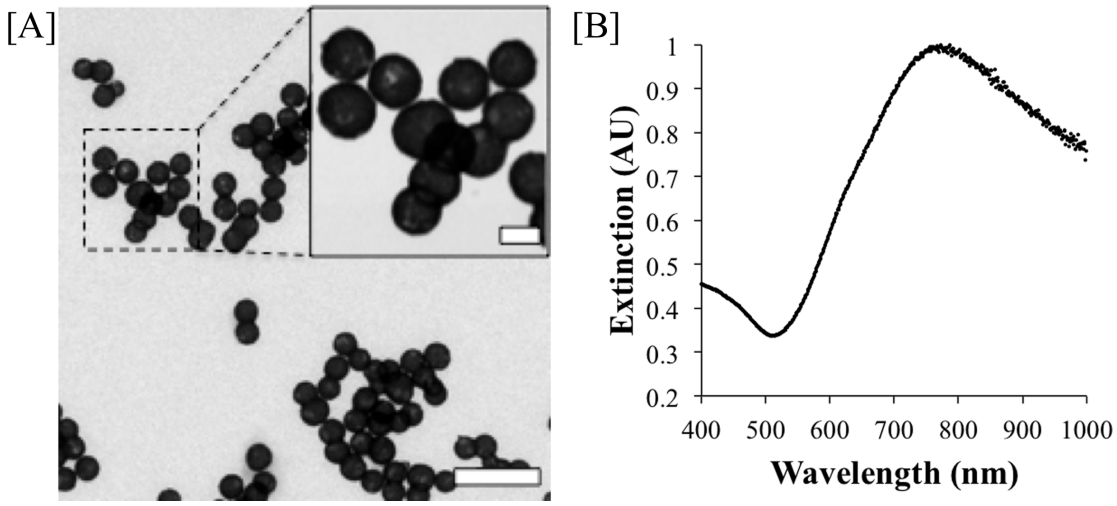

Figure 2.12. Gold-silica nanoshell characterization. [A] TEM image of synthesized gold-silica nanoshells. Scale bars = 500 nm, 100 nm (inset). [B] Extinction spectra of synthesized gold-silica nanoshells. Particles were synthesized to have maximum light absorption in the NIR region.

2.5.2. Poly(NIPAAm-co-AAm) Hydrogel Morphology and Mesh Size

Release profiles of trypsin inhibitor from composites with and without nanoshells are shown in Figure 2.13. From these release profile fits, diffusion coefficients of trypsin inhibitor and mesh sizes for hydrogels with and without nanoshells were calculated using Equations 2.4 and 2.5. Both were found to be similar, indicating diffusive transport through both materials is comparable, and are displayed in Table 2.2 .

Table 2.2. Calculated diffusion coefficients and mesh sizes for hydrogels with and without nanoshells.

	Diffusion Coefficient (D) ($cm^2/s \times 10^6$)	Mesh Size (ξ) (nm)
Nanoshells	0.70 ± 0.11	2.60 ± 0.07
No Nanoshells	0.89 ± 0.08	2.78 ± 0.07

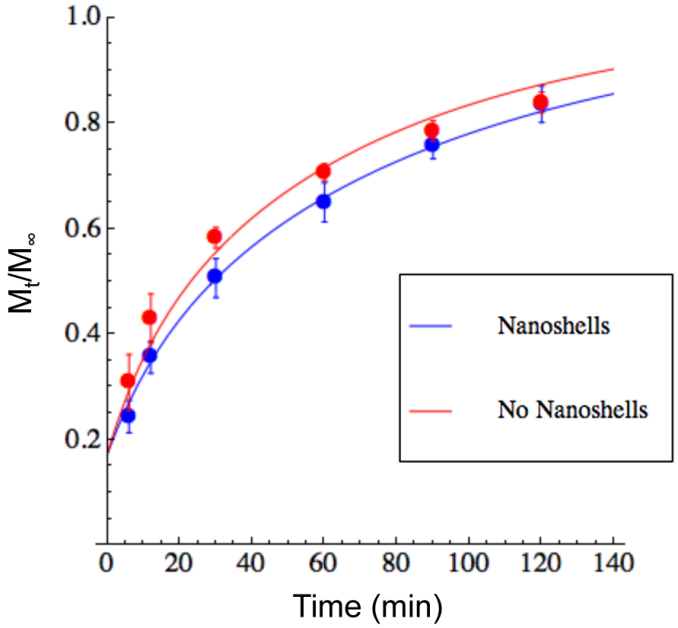

Figure 2.13. Release of trypsin inhibitor from hydrogels with (blue) and without (red) nanoshells. Experimentally measured release data are shown as individual data points, and the theoretical release profiles (based on release data fitted to Equation 2.4) are shown as solid lines.

2.5.3. Poly(NIPAAm-co-AAm) Hydrogel Deswelling

Hydrogel deswelling results, illustrated in Figure 2.14, show that these gels collapsed from 39-45 ^{o}C, a temperature range slightly above physiologic temperature.

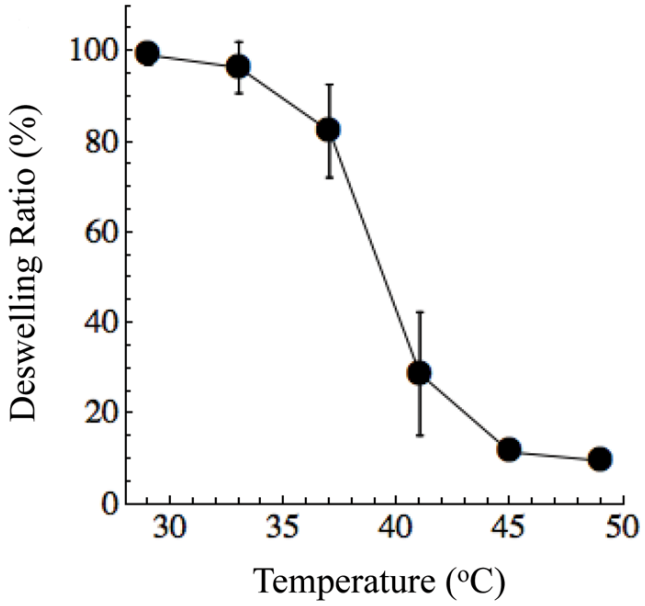

Figure 2.14. LCST Determination. Deswelling of NIPAAm-co-AAm hydrogels as a function of temperature. These hydrogels collapse from 39-45°C. Deswelling ratio was calculated using Equation 2.9.

Additionally, deswelling behavior of this material can be tuned by adjusting the monomer and crosslinker concentrations used, with the incorporation of more hydrophillic molecules (AAm and MBAAm vs. NIPAAm) raising the temperature at which the transition occurs and decreasing the overall amount of deswelling. This is illustrated in Figure 2.15, which compares the deswelling behavior of hydrogels containing a 95:5 and 90:10 molar ratio of NIPAAm:AAm (both with 1:750 molar ratio of crosslinker:monomers).

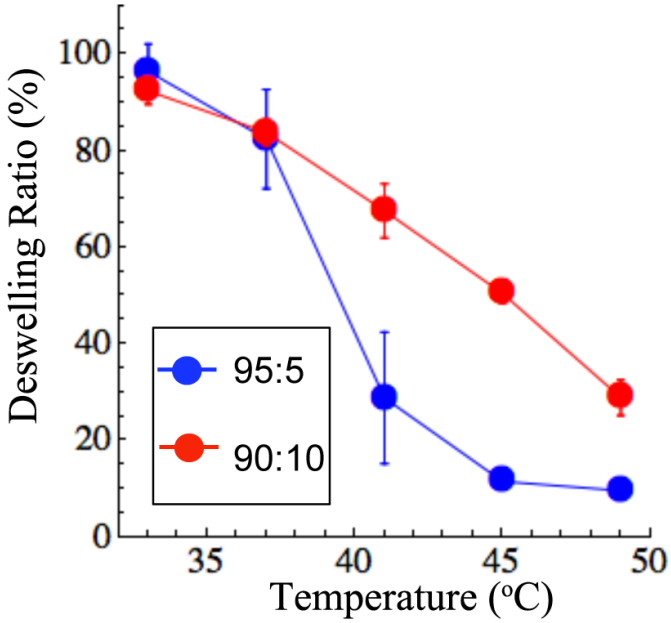

Figure 2.15. Thermal deswelling of poly(NIPAAm-co-AAm) hydrogels with 95:5 and 90:10 NIPAAm:AAm.

Next, hydrogel deswelling in response to NIR exposure was analyzed. Results are shown in Figure 2.16. Both gels with and without nanoshells display similar behavior when incubated at 50 °C, indicating that the presence of nanoshells does not inhibit hydrogel collapse. When exposed to the NIR laser, gels with nanoshells deswell similarly to the gels incubated at 50 °C, while gels without nanoshells exhibit minimal deswelling in response to the laser. This proves that both the presence of nanoshells and exposure to an NIR laser are required to drive gel deswelling.

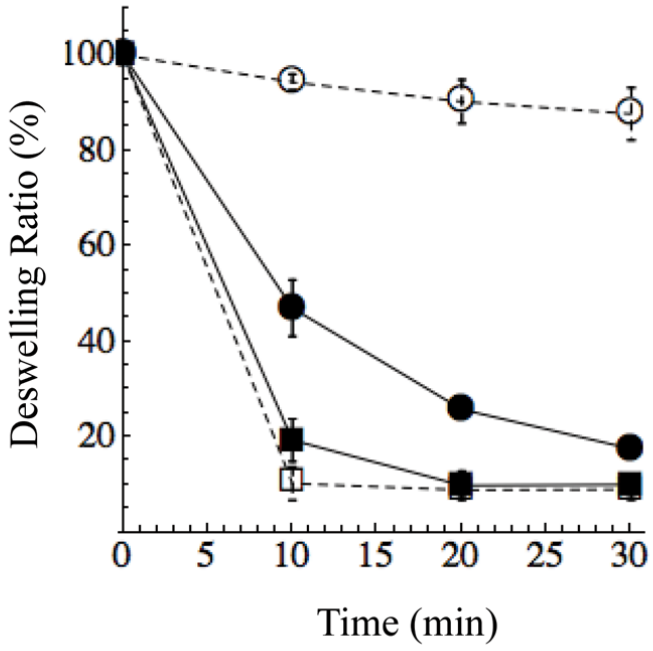

Figure 2.16. Deswelling in response to temperature changes and irradiation. Deswelling of NIPAAm-co-AAm hydrogels with (solid lines) and without (dashed lines) nanoshells by either incubation in a 50 ^{o}C water bath (squares) or exposure to a NIR laser (808 nm, 8 W/cm^2) (ciricles). Both materials displayed similar deswelling behaviors when incubated above material LCST, while only hydrogels with the nanoshells showed deswelling in response to NIR irradiation. Deswelling ratio was calculated using Equation 2.10.

2.6. Conclusions

In this chapter, a poly(NIPAAm-co-AAm)-gold nanoshell composite material was synthesized. This material had an LCST of around 39-45 ^{o}C, meaning it was swollen at physiologic temperature. Expulsion of absorbed water and collapse of the material was found to follow both incubation at 50 ^{o}C and exposure to a NIR laser. With these results, we moved forward to use this optically induced phase transition to trigger drug release from the material, as described in Chapter 3.

3. Drug Loading and Release from Poly(NIPAAm-co-AAm)-Gold Nanoshell Composites[2]

In this chapter, the ability to load and trigger release of therapeutic molecules from the bulk nanoshell-hydrogel composites described in Chapter 2 is investigated. The composite material was loaded with two different cancer therapeutics, and release of both these therapeutics from the material in response to NIR exposure was assessed. A schematic of this process is illustrated in Figure 3.1. Subsequently, the cellular uptake and biological efficacy of a delivered chemotherapeutic was analyzed *in vitro* in a murine colon carcinoma cell line.

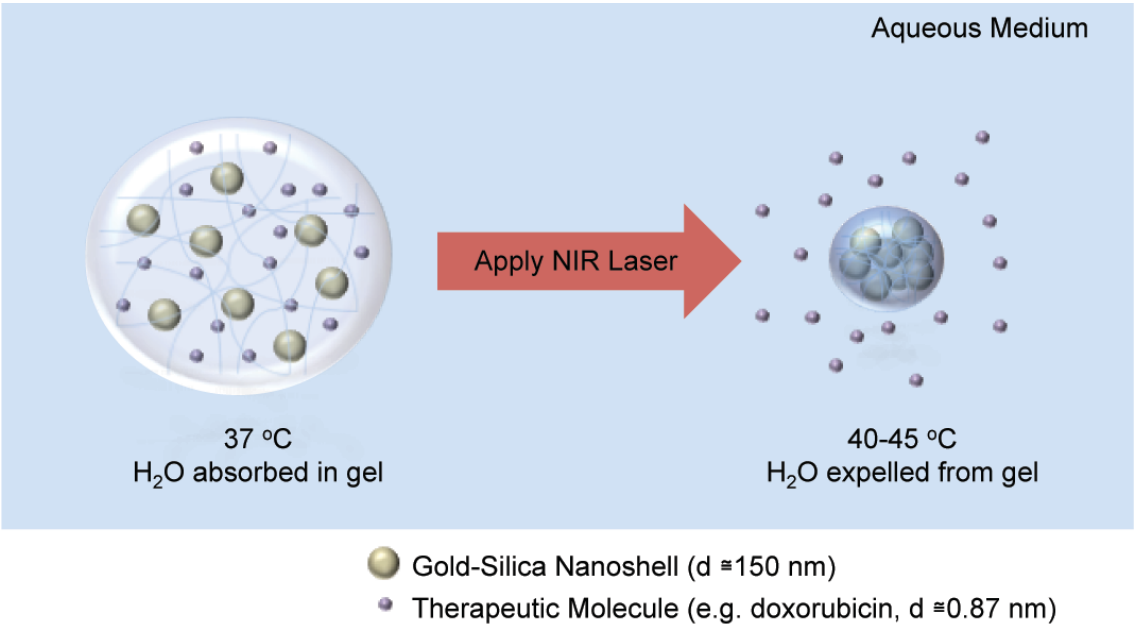

Figure 3.1. Schematic of drug delivery from bulk hydrogel-nanoshell composites.

---

[2] Portions of this chapter are adapted from: Strong L.E., Dahotre S.N, and West, J.L. Hydrogel-nanoparticle composites for optically modulated cancer therapeutic delivery. *J. Control. Release.* 178(8): 63-68 (2014).

3.1. Drug Payload

Release of two therapeutics: a chemotherapeutic (doxorubicin) and a biologic therapeutic (siRNA targeting EphA2) were assessed. These are both used in the treatment of various cancers and also represent opposite ends of the delivery spectrum in terms of molecular size and hydrophobicity. Doxorubicin is a hydrophobic small molecule (580 Da) chemotherapeutic indicated in a wide variety of cancers including hematopoietic malignancies; carcinomas of the breast, lung, ovary, stomach, and thyroid; and sarcomas of bone and soft tissue (Rubin and Williams, 2001). The primary mechanism of action is intercalation with DNA during replication, causing inhibition of topoisomerase II binding and arrest of cell replication (Fornari et al., 1994). Side effects of doxorubicin include myelosuppression, mucositis, and cardiac toxicity; furthermore, these side effects often cause patients to cease doxorubicin therapy, even if the drug is effective against their malignancy (Saltiel and McGuire, 1983).

The second therapeutic analyzed was a short DNA duplex used as a model molecule for siRNA. Typical siRNAs are double-stranded with sticky ends and molecular weights of 12-15 kDa. This study employed a 21 base pair (12,850.5 kDa) oligonucleotide equivalent in sequence to an siRNA targeting the EphA2 protein (target sequence 5'-AATGACATGCCGATCTACATG-3') (Duxbury et al., 2004). EphA2 is a receptor tyrosine kinase known to be upregulated in many cancers; its functions include signaling involved in cell-cell contacts, cell migration, and angiogenesis (Gale and Yancopoulos, 1999). Down regulation of EphA2 has been shown to reduce tumorigenicity in preclinical studies of several cancer types, including pancreatic and

breast carcinomas (Landen et al., 2005). A comparison of these two therapeutics is shown in Table 3.1.

Table 3.1. Comparison of Doxorubicin and siRNA.

	Doxorubicin	siRNA
Drug type	Chemical	Biologic
Size	580 Da	13-15 kDa
Chemical Properties	Hydrophobic	Hydrophillic
Intracellular Transport	Passive diffusion	Endosomal
Mechanism of Action	Inhibition of topoisomerase II	Prevents translation of complimentary mRNA sequences
Benefits for controlled delivery	Minimize off-site toxicity	Increase serum stability
Detection methods	Absorbance (485 nm) or fluorescence (585 nm)	Absorbance at 260 nm

3.2. Materials and Methods

All reagents were purchased from Sigma-Aldrich and used as received, unless otherwise noted. All water used in synthesis, purification, and testing was treated by a Milli-Q system (≥18.0 MΩ·cm resistivity).

3.2.1. Therapeutic Loading

Hydrogels with and without nanoshells were dried under vacuum for at least 48 hr prior to drug loading. The dry weights of the hydrogels were recorded. One set of hydrogels was then soaked in a 0.5 mg/ml (862 μM) solution of doxorubicin in TBS at 4^{o} C for 24 hr. Absorbance readings of loaded hydrogels at 485 nm were used to determine the loaded concentration of doxorubicin, with absorbance readings of non-drug loaded hydrogels used as blanks. A separate set of hydrogels was soaked in a 0.22 mg/ml (17 μM) solution of a 21-bp DNA duplex (Integrated DNA Technologies, inc.) in duplex

buffer (30 mM HEPES, 100 mM potassium acetate, pH 7.5; Integrated DNA Technologies, inc.) at 4 ^{o}C for 24 hr. DNA duplex loading was estimated by measuring the concentration of DNA in the soak solution before and after hydrogel soaking.

3.2.2. Therapeutic Release

Loaded hydrogels, both with and without nanoshells, were placed in TBS (doxorubicin hydrogels) or duplex buffer (DNA duplex hydrogels) and then exposed to an NIR diode laser (Coherent) at 808 nm, 8 W/cm^2 for 30 min. In addition, control hydrogels with nanoshells were kept at room temperature (~22 ^{o}C) for 30 min to evaluate release due to passive diffusion. Every 5 min, a buffer sample was analyzed for drug content via absorbance measurements (doxorubicin, 485 nm; DNA, 260 nm). Release profiles from these three groups were analyzed using an ANOVA with Tukey's HSD.

3.2.3. Analysis of Delivered dsDNA

To ensure that the heating of the gel during the material transition did not denature the dsDNA oligo, the delivered product was run on a native poly(acrylamide) gel. A 20% poly(acrylamide) gel was synthesized by mixing a 19:1 molar ratio of AAm:MBAAm in tris-acetate-EDTA (TAE) buffer. The gel had a volume of ~20 ml and was polymerized by the addition of 300 µl 10% APS (w/v in H_2O) and 30 µl TEMED. The gel was loaded with a 10 bp ladder, the annealed dsDNA oligo as a positive control, and dsDNA oligo obtained from irradiating a loaded composite gel at for 30 min (808 nm, 8 W/cm^2). The gel was run at 120 V for 3 hr and subsequently stained for visualization using both SYBR Gold and SYBR Green (Life Technologies). For staining,

gels were incubated in 150 ml of a 1X solution of each stain in TAE buffer for 15 minutes at room temperature.

3.2.4. *In vitro* Validation

Murine colon carcinoma cells (CT-26.WT cells, ATCC) were cultured in RPMI 1640 media (ATCC) supplemented with 2 mM L-glutamine, 10 mM HEPES, 1 mM sodium pyruvate, 4.5 g/L glucose, 1.5 g/L sodium bicarbonate, 1% penicillin, 1% streptomycin, and 10% fetal bovine serum (FBS). Cultures were maintained at 37 ^{o}C with 5% CO_2.

Cells were seeded in fibronectin-coated 24-well culture plates at a density of 75,000 cells/well. After 24 hr, either a doxorubicin-loaded composite hydrogel or a non-loaded composite hydrogel was placed in a transwell insert (PET membrane, 0.4 μm pore size, Becton, Dickinson and Co.) and covered with media. The hydrogels were then exposed to the NIR laser (808 nm, 8 W/cm^2, 10 min) after which the hydrogel and insert were removed, leaving behind only the delivered drug in the culture media, and the cells were incubated for an additional 24-48 hr. Additional groups included cells that were exposed to loaded composite hydrogels for both 10 min (equivalent time as NIR exposure) and 24 hr as controls, as well as cells which were exposed to 5.4 μg of free dox/well (approximately the amount of doxorubicin that was released from one gel following 10 min of irradiation, results in a drug concentration of ~9.3 μM). After 24 hr, cellular uptake of doxorubicin was assayed by fluorescent microscopy (560 nm excitation, 645 nm emission) using an Axiovert 135 inverted fluorescent microscope (Zeiss). Doxorubicin fluorescent intensity was quantified using ImageJ (NIH) and

analyzed using a Student's t-test. After 48 h, cell proliferation was assessed using a CellTiter96® AQueous proliferation assay (Promega). Using this absorbance-based assay, cell proliferation was normalized to the proliferation of non-treated cells, and proliferation changes among the groups were analyzed using an ANOVA with Tukey's HSD.

3.3. Results

3.3.1. Therapeutic Loading

In separate studies, a chemotherapeutic (doxorubicin) and a biologic therapy (dsDNA, as a model for siRNA) were passively absorbed into the material, with amounts of drug loaded shown in Table 3.2.

Table 3.2. Drug Loading of Hydrogel Composites.

With Nanoshells		Without Nanoshells		
Doxorubicin	dsDNA	Doxorubicin	dsDNA	
466.5 ± 2.6	221.0 ± 13.1	418.3 ± 5.1	209.7 ± 0.9	μg drug loaded / g gel
17.4 ± 1.7	9.0 ± 0.5	15.6 ± 2.0	6.6 ± 0.6	μg of drug per hydrogel disk

3.3.2. Therapeutic Release

Doxorubicin delivery after NIR irradiation indicated that the material with encapsulated nanoshells displayed increased release over controls for all times $t > 0$ (Figure 3.2). After 30 min, delivery of doxorubicin from the irradiated composite hydrogels was approximately 2 times higher than irradiation of hydrogels without nanoshells. (329 μg/g compared to 158 μg/g).

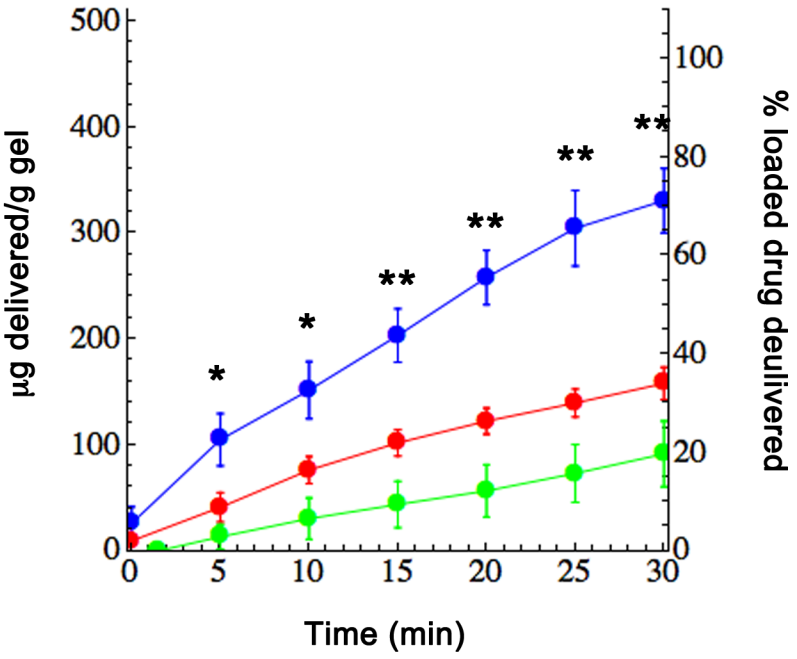

Figure 3.2. Release of doxorubicin from poly(NIPAAm-co-AAm)-nanoshell composite hydrogels. Gels containing nanoshells exposed to an 808 nm laser at 8 W/cm^2 (blue) delivered significantly more drug than gels without nanoshells exposed to the same laser settings (red) and gels with nanoshells left at room temperature as a control (green). *p<0.05, **p<0.01.

Delivery of dsDNA delivery from irradiated composites was nearly 5 times higher than irradiated hydrogels without nanoshells (197.8 µg/g vs 39.68 µg/g) after 30 minutes (Figure 3.3). Overall, 71% of loaded doxorubicin was released from the composite hydrogels after 30 minutes of irradiation, compared to 93% loaded dsDNA. At time points longer than 30 min it is predicted that more doxorubicin will slowly release from the composite due to passive diffusion, however at this point the phase transition of the hydrogel is complete so there will no longer be a convective flow of drug from the material. Additionally, differences in passive diffusion out of the composite were seen for

the two drugs. A larger amount of doxorubicin diffused out of the composite compared to the dsDNA (158 μg/g over 30 minutes vs. 39.68 μg/g). This is likely due to the overall size of the two drugs, with the larger size of the dsDNA therapeutic slowing its diffusion.

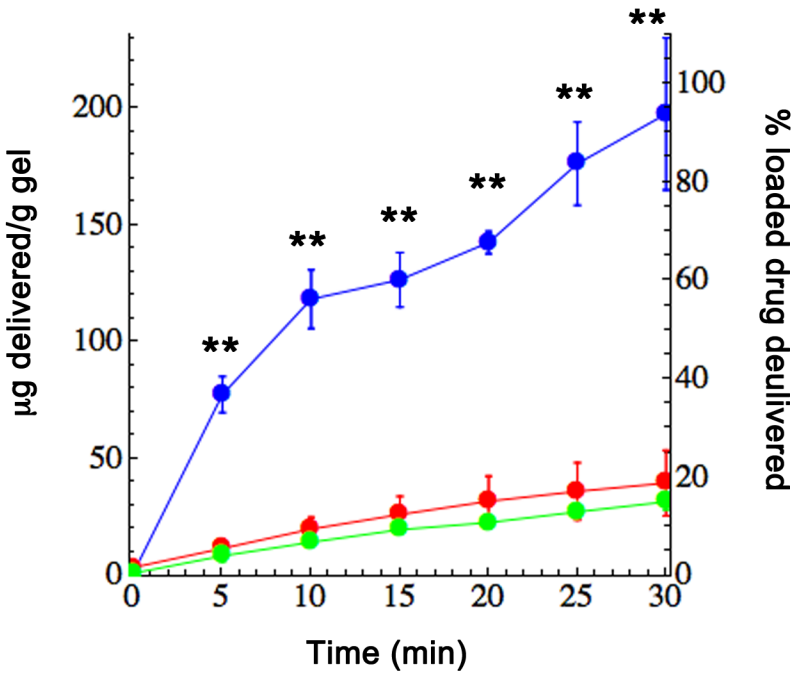

Figure 3.3. Release of DNA duplexes from poly(NIPAAm-co-AAm)-nanoshell composite hydrogels. Gels containing nanoshells exposed to an 808 nm laser at 8 W/cm^2 (blue) delivered significantly more drug than gels without nanoshells exposed to the same laser settings (red) and gels with nanoshells left at room temperature as a control (green). **p<0.01.

In a separate study using doxorubicin-loaded composite hydrogels, NIR light exposure was cycled on and off over a 30 min period (10 min off, 10 min on, 10 min off) to further demonstrate the dependence of release kinetics on NIR exposure, as seen in Figure 3.4.

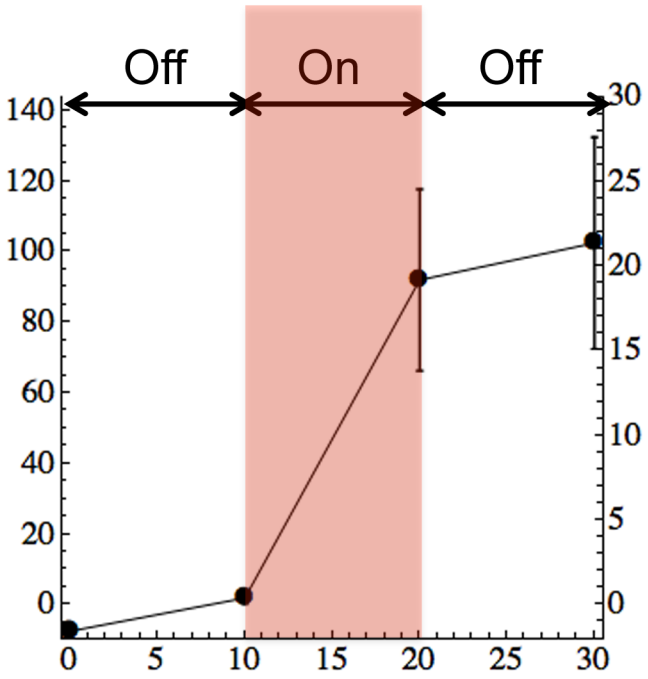

Figure 3.4. NIR exposure effects release kinetics. Delivery of doxorubicin from composite hydrogels exposed to cyclic NIR irradiation (10 min off, 10 min on, 10 min off) shows that the rate of release from the composite greatly increases in response to NIR exposure.

3.3.3. Analysis of Delivered dsDNA

The integrity of the delivered dsDNA was assessed using gel electrophoresis. After gel electrophoresis, the delivered DNA was stained with both SYBR gold and SYBR green. SYBR gold stains all DNA content, while SYBR green preferentially stains dsDNA. The gel was then imaged under UV fluorescence, with the results shown in Figure 3.5.

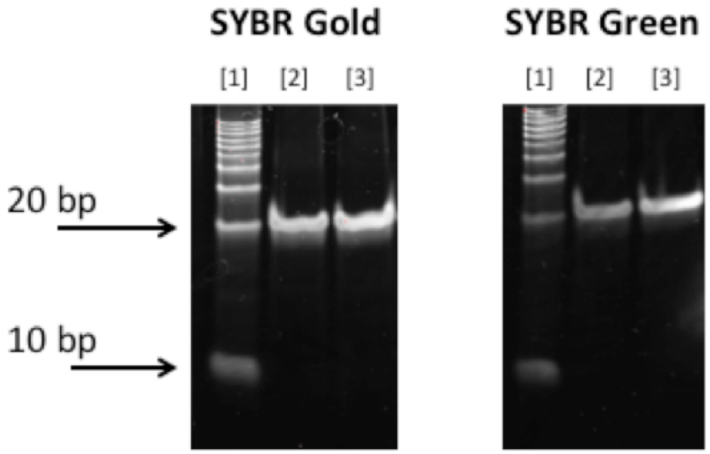

Figure 3.5. PAGE of delivered DNA. Gel electrophoresis of [1] 10 bp ladder, [2] annealed dsDNA olignucleotide, and [3] dsDNA olignucleotide delivered from hydrogel-nanoshell composite via NIR irradiation. Delivered dsDNA ran as a single band at 21 bp, the same size as the annealed dsDNA control.

Results from Figure 3.5 showed that the delivered dsDNA ran as a single band at 21 bp, the same size as the annealed dsDNA control. Under SYBR Gold staining, there were no bands present below the band at 21 bp, which would have indicated the presence of lower MW ssDNA. This suggests the delivered dsDNA oligo was in its double-stranded form.

3.3.4. *In vitro* Validation

To evaluate cellular uptake and biological efficacy, doxorubicin was released from these hydrogel composites and allowed to act on cultured colon carcinoma cells. After 24 hr, cells exposed to irradiated hydrogels showed increased intracellular doxorubicin as compared to cells exposed to non-irradiated hydrogels (Figure 3.6[A-C]). Cells that were exposed to the irradiated hydrogels containing doxorubicin showed a 30% decrease in proliferation (Figure 3.6[D]) in response to doxorubicin exposure, whereas cells cultured

with a non-irradiated doxorubicin composite exhibited minimal changes in proliferation, indicating that the loaded doxorubicin was available to cells only when hydrogels were forced to undergo their thermal phase transition. Further, cells exposed to free doxorubicin showed a similar decrease in proliferation as was seen in the irradiated composite group. Cells exposed to irradiated gels that were not loaded with drug did not exhibit any decrease in proliferation.

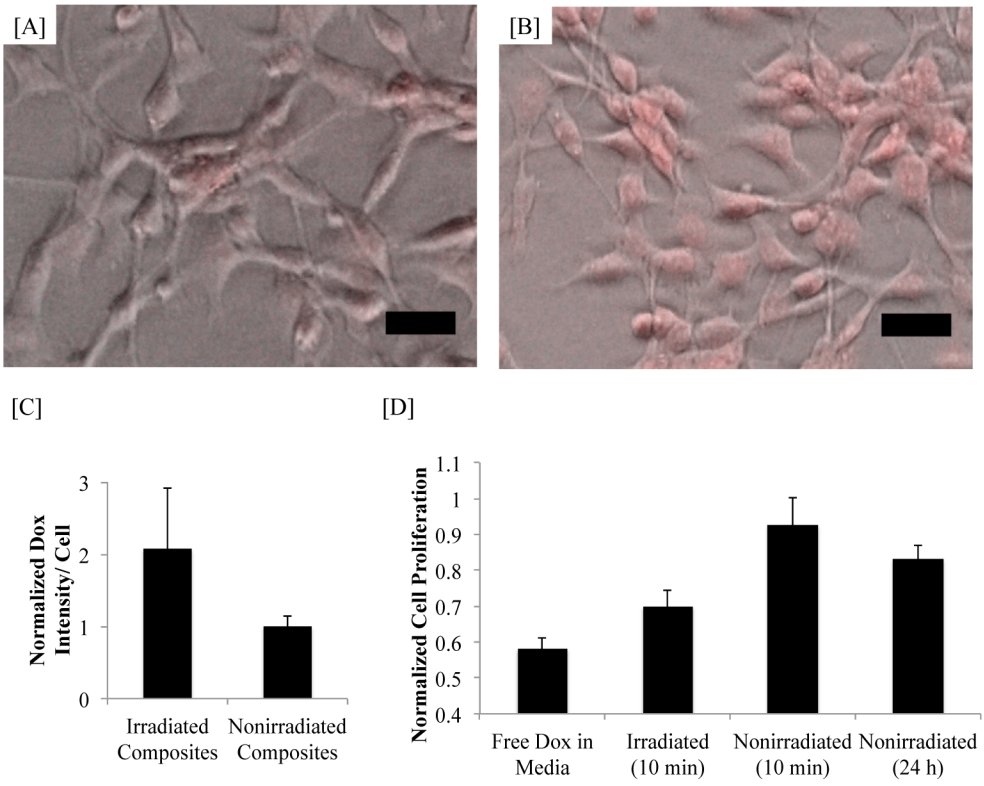

Figure 3.6. Doxorubicin delivery to CT26-WT cells. [A] Phase images overlayed with doxorubicin fluorescent signal of cells exposed to irradiated composite hydrogels [A] and non-irradiated composite hydrogels [B]. Scale bars = 50 μm. [C] Quantification of intracellular doxorubicin fluorescence. Cells exposed to irradiated gels have a significantly higher doxorubicin signal than cells exposed to non-irradiated gels ($p<0.05$). [D] Changes in cell proliferation due to doxorubicin delivery from composite gels. Cells exposed to irradiated gels showed a significant decrease in proliferation ($p<0.05$)

compared to cells exposed to non-irradiated gels, even approaching the response of cells exposed to free doxorubicin.

3.4. Discussion

The goal of the studies described in Chapters 2 and 3 of this dissertation was to design and investigate materials for an optically-triggered cancer therapeutic delivery platform. Materials used in such a platform need to act to (1) encapsulate a therapeutic cargo to limit tissue exposure before desired delivery, and (2) trigger release of this cargo at a specific time and location. The first goal was accomplished by the utilization of a thermally-responsive poly(NIPAAm-co-AAm) hydrogel. This material acts similarly to a sponge, allowing therapeutic molecules to be absorbed within its pores. In addition, this hydrogel was found to have an LCST slightly above 37 ^{o}C, thereby existing in a swollen state at human body temperature, but going through the desired phase change at temperatures easily achievable with minimal biological consequences.

The second goal, triggering the phase transition, was accomplished by the encapsulation of gold-silica nanoshells within the hydrogel. When exposed to light in the NIR range, the nanoshells elicited a temperature increase of the surrounding material. This caused the hydrogel material to collapse and rapidly expel large amounts of water and absorbed therapeutic, demonstrating the capability of optically triggering this material phase transition and subsequent drug delivery.

The loading and release of this therapeutics from the system showed some differing characteristics. For loading of both doxorubicin and dsDNA, a higher amount of drug could be loaded into the composite hydrogels with nanoshells compared to the

polymer-only hydrogels. Overall, a higher concentration of doxorubicin (836 μM) was loaded into the hydrogels than the DNA duplexes (17 μM). This is because doxorubicin is a much smaller molecule, and can therefore easily diffuse into the hydrogel material during loading. However, this same property causes doxorubicin to passively diffuse out of the material much faster than the DNA, leading to higher levels of non-triggered delivery (158 μg/g gel doxorubicin release seen at room temperature vs 40 μg/g dsDNA release). In addition, despite its small size, an overall lower percentage of doxorubicin delivery is seen over 30 min when compared to dsDNA (71% doxorubicin delivered following irradiation, as compared to 93% dsDNA delivered). This is likely due to the chemical nature of the therapeutic being delivered. Hydrophillic molecules are more advantageous for this system, as the material phase transition is based upon the hydrophobic effect, with the hydrophobic polymer material phase separating from its aqueous environment. Therapeutics molecules that are more hydrophobic will have increased affinity to the polymer material, causing them to remain encapsulated within the hydrogel material following water expulsion, as illustrated in Figure 3.7.

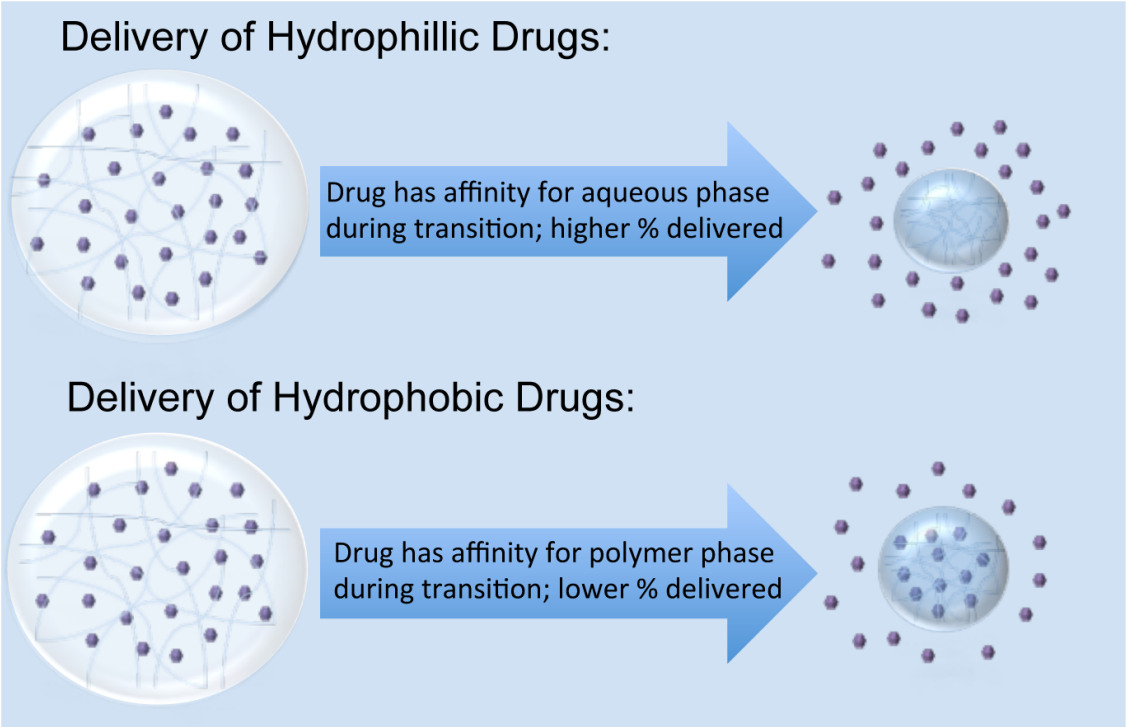

Figure 3.7. Delivery of hydrophillic vs. hydrophobic drugs. More hydrophobic drugs have a higher affinity for the polymer phase during transition than hydrophillic drugs. This causes some amount of hydrophobic drug to remain in the polymer phase following the transition, leading to a lower percent of encapsulated drug delivered.

3.5. Conclusions

These studies validate the potential for this composite material to be used for controlled delivery of cancer therapeutics. Towards translation of this material into *in vivo* applications, the composites could be synthesized as injectable-sized particles rather than bulk discs. This would allow for a platform of similar size as liposomal drug formulations, thus allowing for passive targeting of intravenously administered particles to tumor tissue due to the enhanced permeation and retention effect (Matsumura and Maeda, 1986), as illustrated in Figure 3.8.

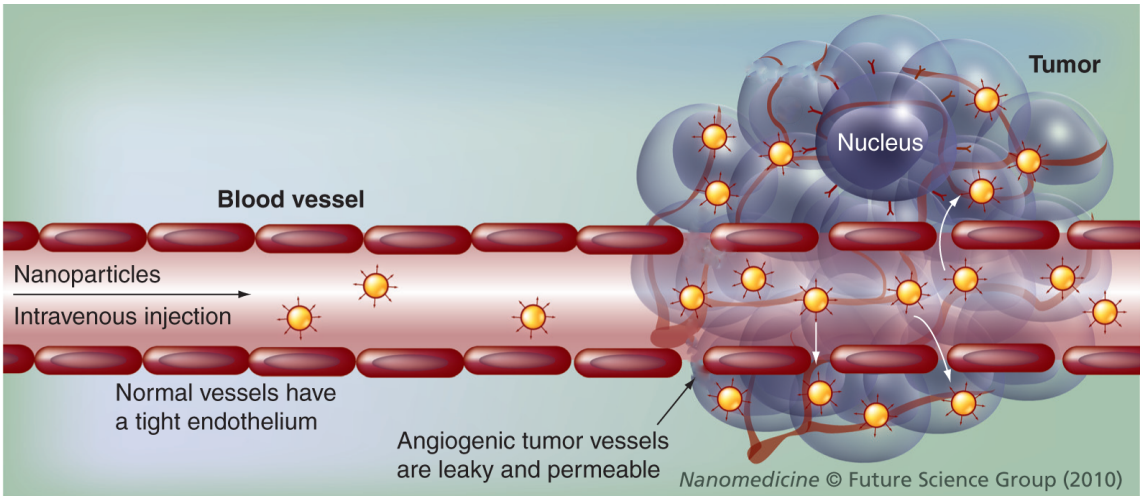

Figure 3.8. Nanoparticle accumulation due to the EPR effect. Intravenously injected nanoparticles passively accumulate in tumor tissue due to leaky tumor vasculature and poor lymphatic drainage. Adapted from (Dong and Mumper, 2010).

After accumulation of particles in tumor tissue, release of drug from the carrier would then be triggered by external NIR exposure. The next two chapters of this dissertation will discuss the synthesis of such a platform.

4. Hydrogel-Nanoshell Composite Particles: Synthesis Using the Hydrogel Template Method

In the previous two chapters of this dissertation, a composite material for optically-triggered drug delivery was synthesized and validated, demonstrating that NIR absorption by nanoshells can drive phase changes in poly(NIPAAm-co-AAm) hydrogels, and thus trigger increased drug delivery. The next goal was to synthesize this material as individual particles smaller than 1 micron. These composite particles will be of a similar size to the nanoshells used in the studies discussed in Section 2.1.3.2, with only a thin layer of hydrogel added to the nanoshell surface; therefore the particles should be able to be injected intravenously and should passively accumulate in most types of tumor tissue due to the EPR effect. Once the particles reach the tumor site, an NIR laser will be applied to the tumor. As previously described, optical absorption by the nanoshells will cause a rapid heating of the embedded nanoshells, which in turn should trigger a collapse of the polymer coating and release of absorbed drug molecule directly at the tumor site. Figure 4.1 below illustrates this process.

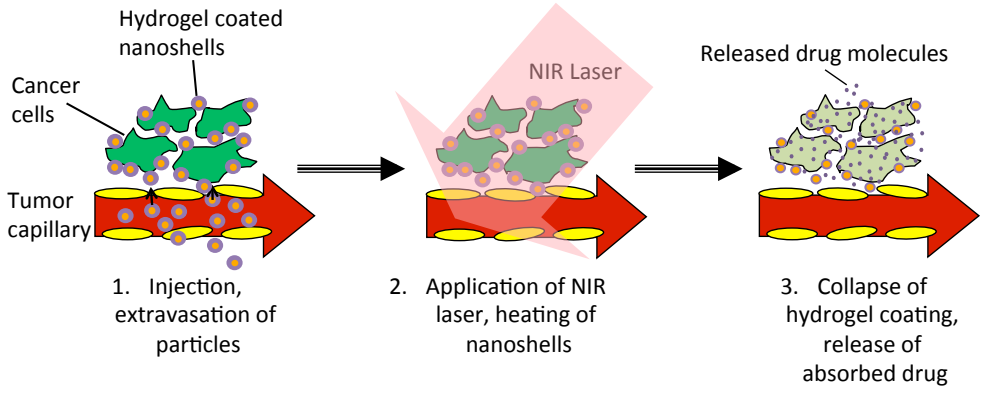

Figure 4.1. Schematic of hydrogel-nanoshell composite particle therapy. (1) Injected particles will circulate and passively accumulate into tumor tissue. (2) An applied NIR

laser causes rapid heating of the embedded nanoshells. (3) The resulting temperature increase causes release of absorbed drug molecules from the thermally responsive coating directly at the tumor site.

This platform has the inherit ability to cause destruction of the tumor by two mechanisms simultaneously. The encapsulated nanoshells can be used to generate sufficient heating to cause hyperthermic therapy, as well as allow for a burst release of a pharmaceutical payload. Further, numerous studies have shown enhanced efficacy of chemotherapeutic treatments when combined hyperthermic treatments (Hildebrandt et al., 2002, Hahn, 1979, Marmor, 1979). In fact, combining hyperthermia and drugs has been shown to elicit a more than additive response for multiple classes of chemotherapeutic agents, including platinum drugs, alkylating agents, nitrosources, and antibiotics (Issels, 2008).

In addition to platforms consisting of thermally-responsive hydrogel-nanoparticle composites, composites consisting of temperature-sensitive liposomes or elastin-like polypeptides and gold nanoparticles have been studied. The following section briefly outlines these platforms.

4.1. Platforms Utilizing Liposomes and ELP Coatings

4.1.1. Temperature-Sensitive Liposomes

In addition to thermally-responsive hydrogels, temperature-sensitive liposomes (TSLs) have been investigated for drug delivery applications, with some formulations reaching clinical trials (Dromi et al., 2007). Many TSLs utilize dipalmitoyl phosphatidylcholine (DPPC) lipids, which display an acyl-chain melting phase transition at 41 ^{o}C (Ponce et al., 2006). When transitioning from below to above 41 ^{o}C, DPPC

transitions from a solid (crystalline) phase to a liquid phase, resulting in leakage of the liposome's contents (Ponce et al., 2006). Additionally, this release can be enhanced by incorporating micelle-forming lysolipids, such as monostearoyl phosphatidylcholine (MSPC), into the lipid bilayer (Needham et al., 2000).

Recent work by Qin et al. aimed to combine a TSL with gold nanoparticles attached to the surface (Qin et al., 2011). The characteristics of this system are described in Figure 4.2. This system was tested with doxorubicin and was found to retain the encapsulated drug at 40 ^{o}C for 3 days and instantaneously release over 70% of the encapsulated drug upon exposure to a 532 nm laser. Further research is being done to tether hollow gold nanoshells, which have a surface plasmon peak in the near infrared range, instead of solid gold nanoparticles, to allow the system to be used in clinical applications (Qin et al., 2011). Other groups have looked at remote control release from thermo-sensitive liposomes by separate injections of liposomes and gold nanorods (Agarwal et al., 2011).

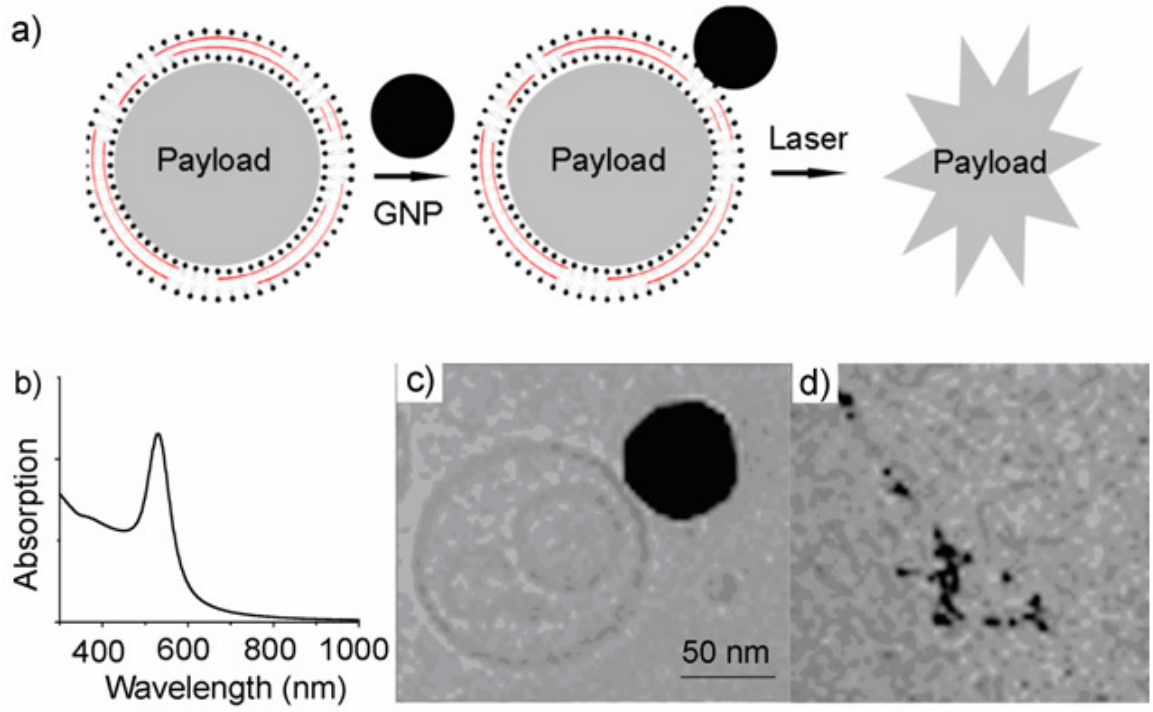

Figure 4.2. Properties of thermally responsive lipsome-gold nanoparticle complexes. [A] Schematic of drug release process. [B] UV-vis absorption spectrum of the gold nanoparticles used. [C] Cryo-TEM image of a liposome tethered to a gold nanoparticle [D] Cryo-TEM image of a liposome-nanoparticle complex after irradiation with a 532 nm laser. From (Qin et al., 2011).

4.1.2. Elastin-Like Polypeptide Coatings

Additionally, composite particles consisting of gold nanoparticles and ELPs have been investigated. Huang et al. developed an optically responsive ELP-gold nanorod system (Huang et al., 2008). A novel 22 kDa cysteine containing ELP was conjugated to NIR absorbing gold nanorods by gold-thiol bonds (Huang et al., 2008). The transition temperature (T_t) of the ELP was determined to be 33.4 ^oC; above this temperature the particles aggregated together resulting in an increase in optical density. NIR irradiation of these particles resulted in an optical response due to a conformational change in the ELP (Huang et al., 2008).

4.2. Synthesis of Nanoscale Hydrogel Particles

While the studies described above utilized liposomes or ELPs as the thermally-sensitive component, several methods have been developed to synthesize nanoscale particles consisting of synthetic polymers. Many of these methods are based on soft lithography techniques (Jeong et al., 2010). Soft lithography is generally characterized by the creation of an elastomeric stamp or mold using microfabrication techniques developed in the electronics industry (Jeong et al., 2010). Two such techniques include Particle Replication In Nonwetting Templates (PRINT) (Rolland et al., 2005) and the hydrogel template method (Acharya et al., 2010a). In this chapter, the hydrogel template method will be adapted to synthesize poly(NIPAAm-co-AAm)-gold nanoshell composite particles.

4.2.1. PRINT

The PRINT method developed by the DeSimone group uses photocurable perfluoropolyether (PFPE) molds to emboss a prepolymer solution onto a highly fluorinated surface (Rolland et al., 2005). Such surfaces are nonwetting to organic materials, thereby allowing for synthesis of individual particles, as seen in Figure 4.3 (Rolland et al., 2005).

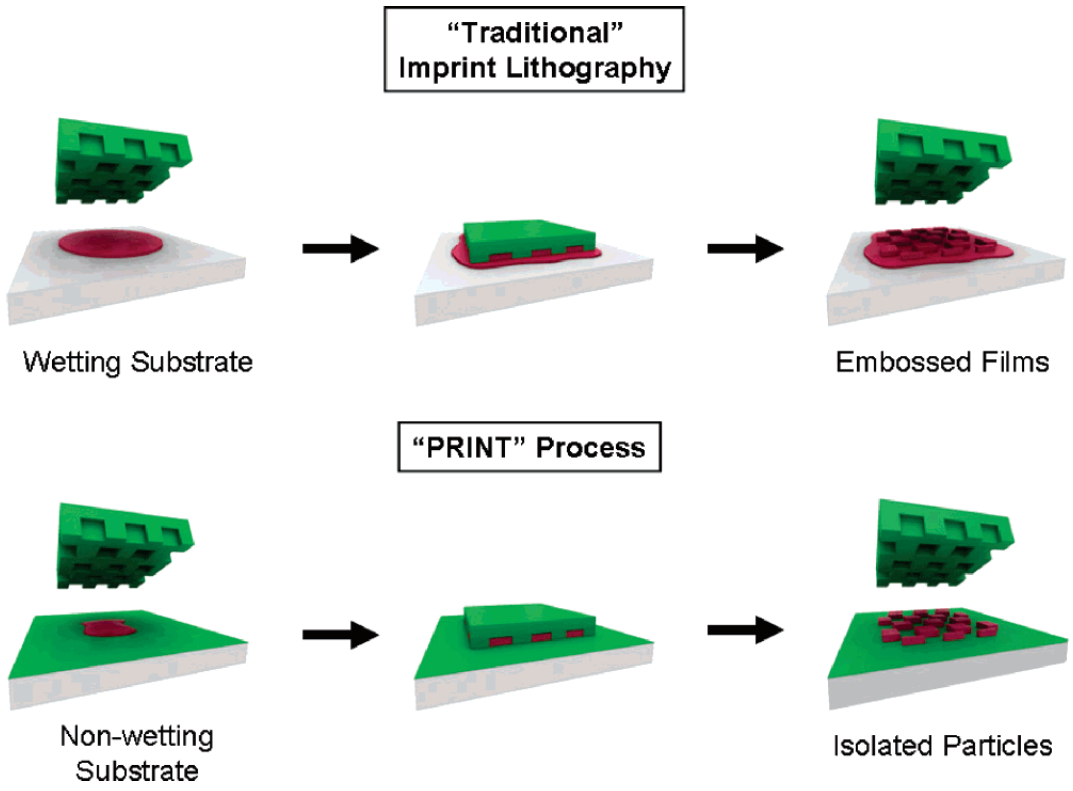

Figure 4.3. PRINT compared to traditional imprint lithography. In traditional imprint lithography, the affinity of the liquid precursor to the surface of the substrate results in a scum layer. In PRINT, the non-wetting surface causes the liquid precursor to be confined only in the wells of the mold, resulting in the synthesis of isolated particles. From (Rolland et al., 2005).

This method has been used to synthesize various different particles made of materials such as poly(D-lactic acid), PEG hydrogels, and proteins, with sizes ranging from 80 nm to 20 μm (Rolland et al., 2005, Kelly and DeSimone, 2008). Particles have been synthesized to be pH sensitive (Petros et al., 2008, Parrott et al., 2010), and have been loaded with chemotherapeutics (Petros et al., 2008) and contrast agents (Parrott et al., 2012, Nunes et al., 2010).

4.2.2. Hydrogel Template Method

A novel method for synthesizing homogenous polymer particles was recently reported by the Park group (Acharya et al., 2010a, Acharya et al., 2010b). This method relies on the use of a hydrogel template made of a material such as gelatin (Acharya et al., 2010a). These gelatin templates can be easily constructed using common microfabrication techniques. They are mechanically stable enough to act as a mold yet undergo a sol-gel transition upon heating, allowing dissolution of the mold after particle formation is complete (Acharya et al., 2010a). This process can be used to make polymer particles from 200 nm to larger than 50 μm. The hydrogel template process is summarized in Figure 4.4.

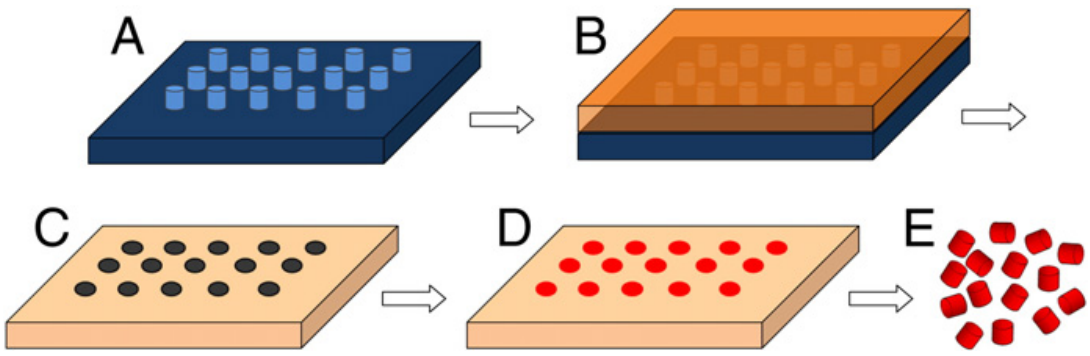

Figure 4.4. The hydrogel template method for particle synthesis. [A] A silicone wafer master is created with vertical posts of desired particle size. [B] A warm aqueous gelatin solution is poured on top of the master. [C] The gelatin is cooled to solidify and peeled off the master to expose cavities. [D] Cavities are filled with polymer mixture and dried to remove organic solvent. [E] Mold is dissolved in warm H_2O, and particles are collected by centrifugation or filtration. From (Acharya et al., 2010a).

An initial study examined the versatility of the synthesis method by fabricating poly(lactic-co-glycolic)acid (PLGA) particles of various sizes (from 200 nm up to 50 μm) and of various shapes, as shown in Figure 4.5 (Acharya et al., 2010a).

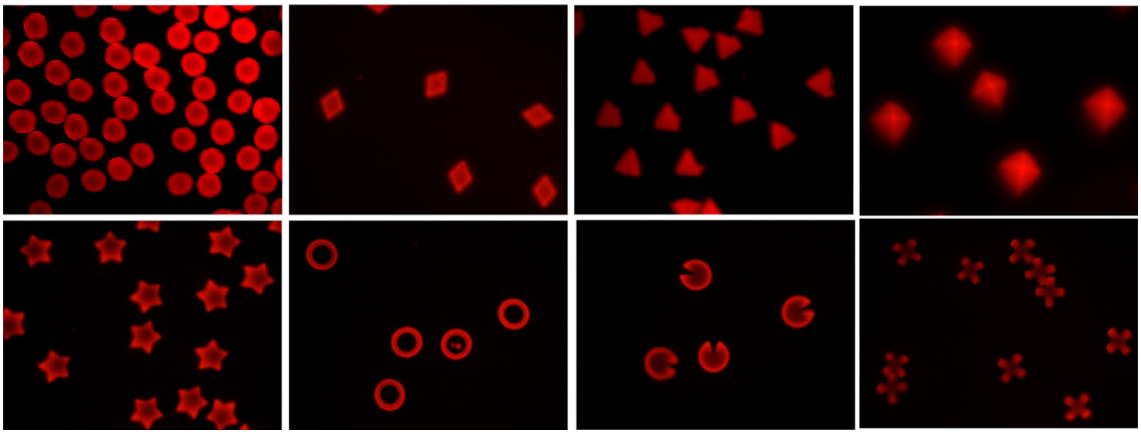

Figure 4.5. Various shapes of particles synthesized from the hydrogel template method. Particle size is 50 μm. From (Acharya et al., 2010a).

A further study by Acharya et al. analyzed drug release from degrading PLGA microparticles (Acharya et al., 2010b). These particles displayed extremely high drug loading capabilities (>50% w_{drug}/w_{PLGA}) and delivered ~80-100% of loaded drug within 20-25 days. Release kinetics were dependent on surface area, diffusion coefficient, and concentration gradient (Acharya et al., 2010b).

4.3. Materials and Methods

All reagents were purchased from Sigma-Aldrich and used as received, unless otherwise noted. Polydimethylsiloxane (PDMS) templates were received from Dr. Ghanashyam Acharya from The Methodist Hospital Research Institute. All water used in synthesis, purification, and testing was treated by a Milli-Q system (≥18.0 MΩ·cm resistivity).

4.3.1. Synthesis of PDMS Templates

PDMS templates were synthesized analogously to methods described previously (Acharya et al., 2010a, Lu et al., 2014). Briefly, a photoresist was spun-coated to a height of 500 nm and baked. The photoresist was then exposed using E-beam lithography in a predetermined pattern consisting of an array of circular features 500 nm in diameter. Thus, a master was created consisting of an array of wells of a 500 nm diameter and height. This master template was then coated with Sylgard 184 elastomer (Dow Corning) and cured for 2 hr at 70 ^{o}C. The PDMS template was then carefully removed from the master template, yielding a template consisting of cylindrical features 500 nm in diameter and height.

4.3.2. Synthesis of Hydrogel Templates

The hydrogel template method described in Section 4.1.2 was used to synthesize 500 nm poly(NIPAAm-co-AAm) hydrogels with embedded nanoshells. The PDMS templates used contained 500 nm cylindrical (*i.e.*, 500 nm in diameter and 500 nm in height) vertical posts, with each 2-inch square template containing an array of 5 x 10^{8} posts. Next, 4 ml of a warmed (50-55 ^{o}C) 20% w/v aqueous Gelatin Type A solution was poured over the PDMS template. After allowing the gelatin to solidify by incubating at 4 ^{o}C for 15 min, the gelatin was peeled from the PDMS template, revealing a second template with circular wells of 500 nm diameter and 500 nm height.

4.3.3. Hydrogel Template Particle (HTP) Synthesis

After template synthesis, a monomer solution containing NIPAAm, AAm, and MBAAm in H_2O was made analogously to that made Section 2.1.2 (1.56 M NIPAAm, 82 mM AAm, and 2.18 mM MBAAm in H_2O). In addition, gold-silica nanoshells were added to this solution at a concentration of 1.5 x 10^{10} particles/ml, as at this concentration it was estimated that 1.5 nanoshells would be loaded in each well of the template. Aliquots of 100 µl were made of this monomer suspension, and polymerization was then initiated by addition of 2.5 µl APS (10% w/v in H_2O) and 0.5 µl TEMED. After rapid mixing by vortexing, 50 µl of this solution was pipetted onto a gelatin template and whisked across using a razor blade at a 45^o angle to completely fill the template wells. The particles were allowed to polymerize for 2 hr at room temperature.

After polymerization, hydrogel templates were dissolved in H_2O (with 0.1% w/v NaN_3 to prevent microbial contamination) and incubated at 50-55^{o}C for 30-60 min. The hydrogel-nanoshell composite particles (HNCPs) were then purified by 2 rounds of centrifugation (2000 x g, 5 min) and then passed through a 5 µm polycarbonate membrane filter. Poly(NIPAAm-co-AAm) hydrogel particles without nanoshells (NHPs) were synthesized analogously without adding nanoshells to the monomer solution. A schematic of this process is shown in Figure 4.6.

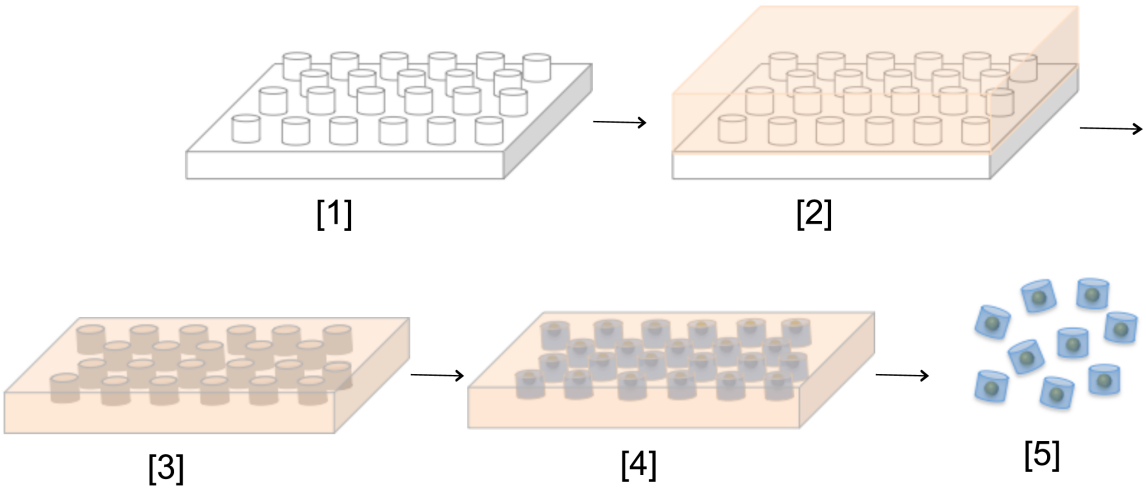

Figure 4.6. Particle synthesis based on hydrogel template method. [1] Master created with cylindrical posts 500 nm (diameter) by 500 nm (height). [2] Warm gelatin poured over master. [3] Cooled gelatin peeled off of master to reveal cavities 500 nm (diameter) by 500 nm (height). [4] Monomer solution and gold-silica nanoshells poured into cavities. Polymerization is initiated by APS/TEMED. [5] After polymerization, gelatin template is dissolved in warm water and HNCPs are collected by centrifugation.

4.3.4. Hydrogel Template Particle (HTP) Characterization

After synthesis, HNCPs were characterized using electron microscopy. A FEI Tecnai G^2 Twin TEM was used for visual inspection of the poly(NIPAAm-co-AAm) polymer as well as any embedded gold nanoshells.

DLS was used to determine changes in particle size in response to increased temperatures and NIR irradiation. DLS measures the Brownian motion of particles in a liquid to extrapolate their hydrodynamic radius (Malvern Instruments, 2014). Both HNCPs and NHPs were sized using a Brookhaven 90-Plus Particle Size Analyzer under three different conditions: at 25 ^{o}C, at 50 ^{o}C, and after being exposed to NIR irradiation (808 nm, 5 W/cm^2, 5 min). For the NHPs, the refractive index of poly(NIPAAm) was used (1.52) (Reufer et al., 2009). For the HNCPs, the refractive index of gold at 660 nm

(the incidence of the detection laser) was used (0.169 + 3.821*i*) (Schulz and Tangherlini, 1954, Schulz, 1954). Hydrodynamic diameters at 25 ^{o}C, 50 ^{o}C, and post NIR irradiation were compared using an ANOVA with Tukey's HSD.

4.4. Results

4.4.1. TEM Characterization

TEM images of gold-silica nanoshells and HNCPs are compared in Figure 4.7, indicating that the HNCPs having a thin polymer coating around the gold nanoshells. Since samples must be fully dehydrated before imaging, this coating is much smaller than it would be in its hydrated state.

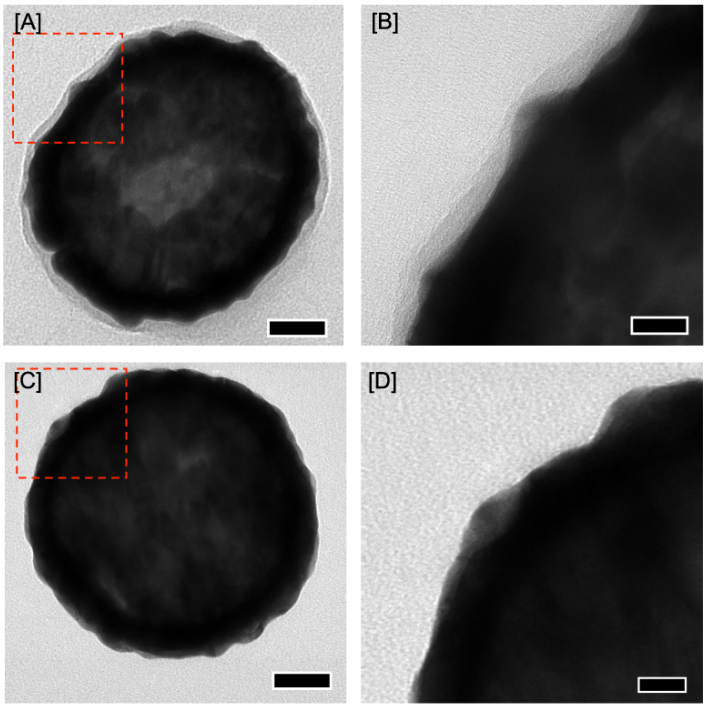

Figure 4.7. Analysis of HTPs by TEM. **[**A] TEM image of an HNCP compared to [C] TEM images of a bare nanoshell. Scale bar = 30 nm. [B] Higher magnification of this coating as compared to [D] the bare nanoshell surface. Scale bar = 10 nm.

4.4.2. Thermal Analysis via Dynamic Light Scattering

Changes in the hydrated sizes of both HNCPs and NHPs in response to increased temperatures as well as NIR irradiation was analyzed using DLS, with results summarized in Figure 4.8. NHPs have a significantly smaller diameter when incubated at 50 ^{o}C, while the HNCPS have a significantly smaller diameter when either incubated at 50 ^{o}C or exposed to NIR irradiation (as determined by ANOVA with Tukey's post hoc test, n=3).

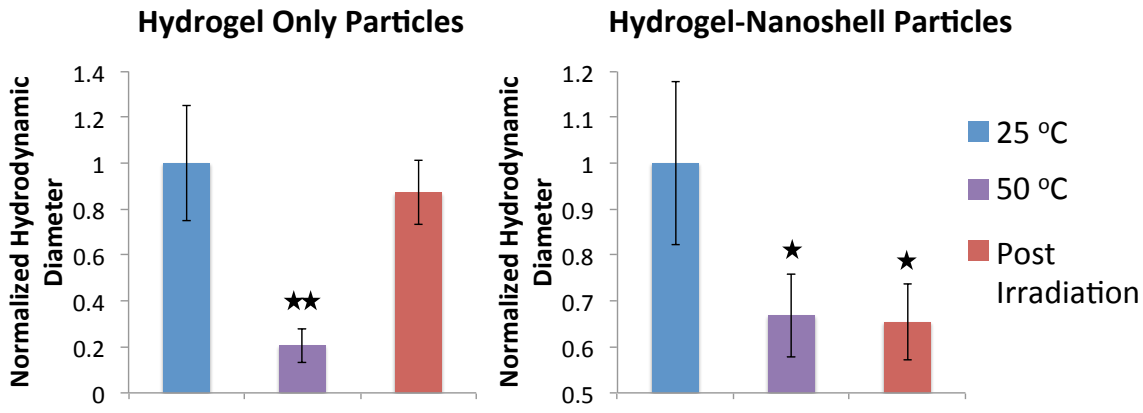

Figure 4.8. Analysis of HNCP thermal deswelling. Hydrodynamic diameters of hydrogel-only and hydrogel-nanoshell composite particles as measured by DLS. Measurements are normalized to particle size at 25^{o}C. Hydrogel-only particles deswell in response to increased temperature, while hydrogel-nanoshell particles deswell in response to either increased temperature or exposure to NIR irradiation. (*$p<0.05$, **$p<0.01$).

While DLS provides a technique to determine the size of sub-micron particles in a hydrated state, the measurements are dependent on many factors, including the material refractive index (Malvern Instruments, 2014), and the HNCPs consist of two different materials with drastically different refractive indices. In addition, DLS measurements assume particles are spherical, whereas these particles are cylindrical (Malvern

Instruments, 2014). Due to these limitations, the hydrodynamic diameters measured are most likely not the particle's true size, so measurements for each particle type are normalized to its measurement at 25 ^{o}C.

Additionally, when the particle sizes of the HNCPs in the collapsed state were measured, two separate size populations emerged, as displayed in Figure 4.9. A population at a smaller diameter represented single particles, while a second population centered around a larger diameter likely resulted from the aggregation of multiple particles. The material phase transition that causes polymer collapse will also act as a driving force for aggregation due to the hydrophobic effect. For the data displayed in Figure 4.8, only the "single particle population" of these measurements was used.

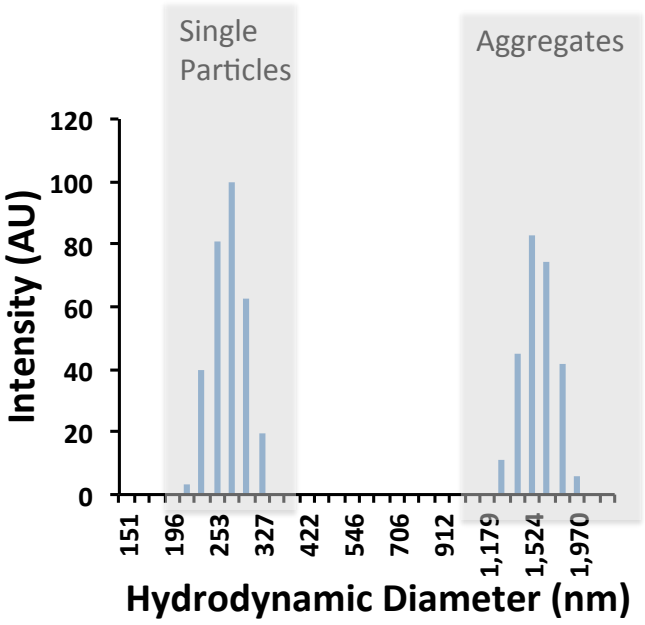

Figure 4.9. Typical size distribution of HNCPs in their collapsed stage after irradiation. The particles exhibited two distinct populations, hypothesized to be single particles vs. particle aggregates.

4.5. Discussion and Conclusions

In this chapter, the composite material developed in Chapters 2-3 of this dissertation was synthesized as nanoscale particles by using a dissolvable gelatin template. Image analysis using TEM indicates that the resulting particles consist of a nanoshell core surrounded by thin polymer layer. The hydrodynamic diameter of these particles decreases in response to either incubation at 50 ^{o}C or exposure to NIR irradiation, proving that these particles retain the same thermal properties as the bulk material. This indicates the potential of this material to be used as an injectable-sized platform for therapeutic delivery.

One potential disadvantage of using this synthesis method is that it does not allow for direct control over how many nanoshells are loaded into each well of the gelatin template, and therefore how many nanoshells are in each HNCP. While each template was loaded with a nanoshell concentration corresponding to ~1.5 nanoshells/well, this will result in an HNCP population with a distribution of loaded nanoshells, with zero, one, or even two or more nanoshells per composite particle. This distribution may also be contributing to the heterogeneity of the DLS measurements, where often multiple size populations could be detected.

For this delivery platform, a 1:1 ratio of hydrogel:nanoshell would allow for maximal volume for drug loading (due to only having one nanoshell per particle) with each composite particle maintaining its NIR nanoshell trigger. To achieve such, a second synthesis method in which a hydrogel network is grown off of individual nanoshells,

therefore resulting in this 1:1 ratio, was explored. This method will be described in the next two chapters of this dissertation.

5. Hydrogel Coated Nanoshells: Synthesis Using Surface Initiated- Atom Transfer Radical Polymerization

In addition to the molding techniques discussed in Chapter 4, controlled radical polymerization (CRP) methods have been researched for the synthesis of near-monodisperse polymer nanoparticles. These methods allow for tight control over the spatial location of generated free radicals, thus resulting in desirable polymer properties such as high control over molecular weights and end functionalities (Coessens et al., 2001). Several different types of CRP techniques have been investigated for synthesizing thermally-responsive hydrogel coatings onto individual particles including reversible addition-fragmentation chain transfer (RAFT) (Shan et al., 2004, Shan et al., 2005, Nupponen and Tenhu, 2007, Yusa et al., 2007), surfactant-free emulsion polymerization (SFEP) (Kim and Lee, 2006, Kim and Lee, 2007, Kim and Lee, 2008), surface initiated-atom transfer radical polymerization (SI-ATRP) (Frimpong and Hilt, 2008, Wei et al., 2008, Chakraborty et al., 2010, Chirra et al., 2012), and other methods (Morones and Frey, 2009, Singh and Lyon, 2007). These techniques are summarized in Table 5.1 below. Additional studies have focused on the investigation of aerosol-based fabrication of poly(NIPAAm)-metal nanoparticle composites (Byeon and Roberts, 2012), and synthesis of poly(NIPAAm)-based hydrogels and gold nanoparticles simultaneously yielding uniform nanoscale composites (Zhu et al., 2012).

Table 5.1. Radical Chain Polymerization Techniques (Odian, 2004, Barner-Kowollik et al., 2001, Xu et al., 2009).

Surfactant-Free Emulsion Polymerization (SFEP) -Initiator soluble in aqueous phase -Produces free radicals that are surface-active of polymer particles -Polymerization occurs on surface of polymer droplets in oil phase	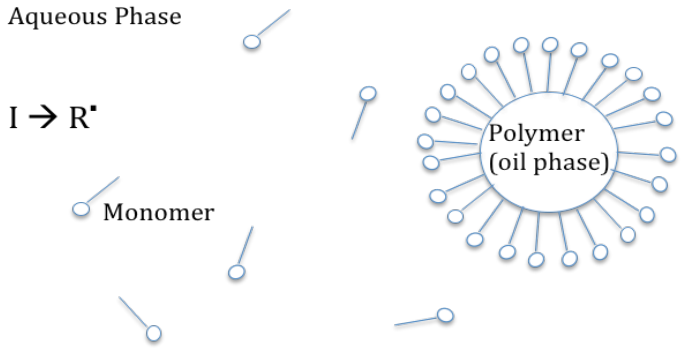
Reverse-Addition Fragmentation Polymerization (RAFT) -Requires initiator in presence of chain-transfer agent -Living polymerization technique	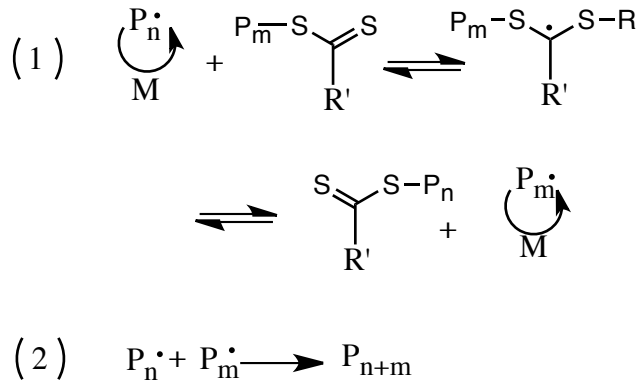
Atom Transfer Radical Polymerization (ARTP) -Requires a transition metal catalyst, nitrogen based ligand, and alkyl-halide	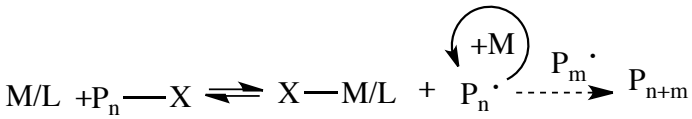 M = Transition Metal L = Nitrogen-based Ligand X = Br or Cl

5.1. Controlled Polymerization of Poly(NIPAAm)

5.1.1. Surfactant-Free Emulsion Polymerization

The work of Kim et al. investigated SFEP of poly(NIPAAm-co-AAc) onto gold nanoparticles and gold-silica nanoshells for drug delivery applications (Kim and Lee, 2006, Kim and Lee, 2007, Kim and Lee, 2008). This synthesis method used a 94:6 wt% ratio of NIPAAm:AAc and MBAAm as a crosslinking agent. This process was carried out on 60 nm gold nanoparticles (Kim and Lee, 2006) and 120 nm gold-silica nanoshells (Kim and Lee, 2008). In addition, studies using SFEP poly(NIPAAm-co-AAc) as a template for the growth of large (60-150nm) gold nanoparticles have also been investigated (Kim and Lee, 2007). In the study utilizing gold-silica nanoshells, field emission scanning electron microscopy (FE-SEM) images showed uniform particle sizes as well as contrast effects showing particle cores with a complete hydrogel coating (Kim and Lee, 2008). Energy-dispersive X-ray spectroscopy (EDX) analysis showed large peaks indicating gold atoms as well as no peaks for the hydrogel polymer, as predicted given the low atomic numbers of the hydrogel elements. Higher resolution TEM images show the complete hydrogel shell growth around the particle, as well as differences in hydrogel thickness that could be obtained by minor variations in the monomer and initiator amounts or reaction time. UV-Vis spectroscopy showed minimal changes in the absorption profile of the bare gold-silica nanoshells and hydrogel-coated nanoshells. DLS studies show that the hydrodynamic radius of the hydrogel particles decreasing with increasing temperature, an indication of collapse of the hydrogel (Kim and Lee, 2008).

However, one drawback of this polymerization method is the encapsulation of multiple particles into one hydrogel matrix. The results of this study are summarized in Figure 4.2.

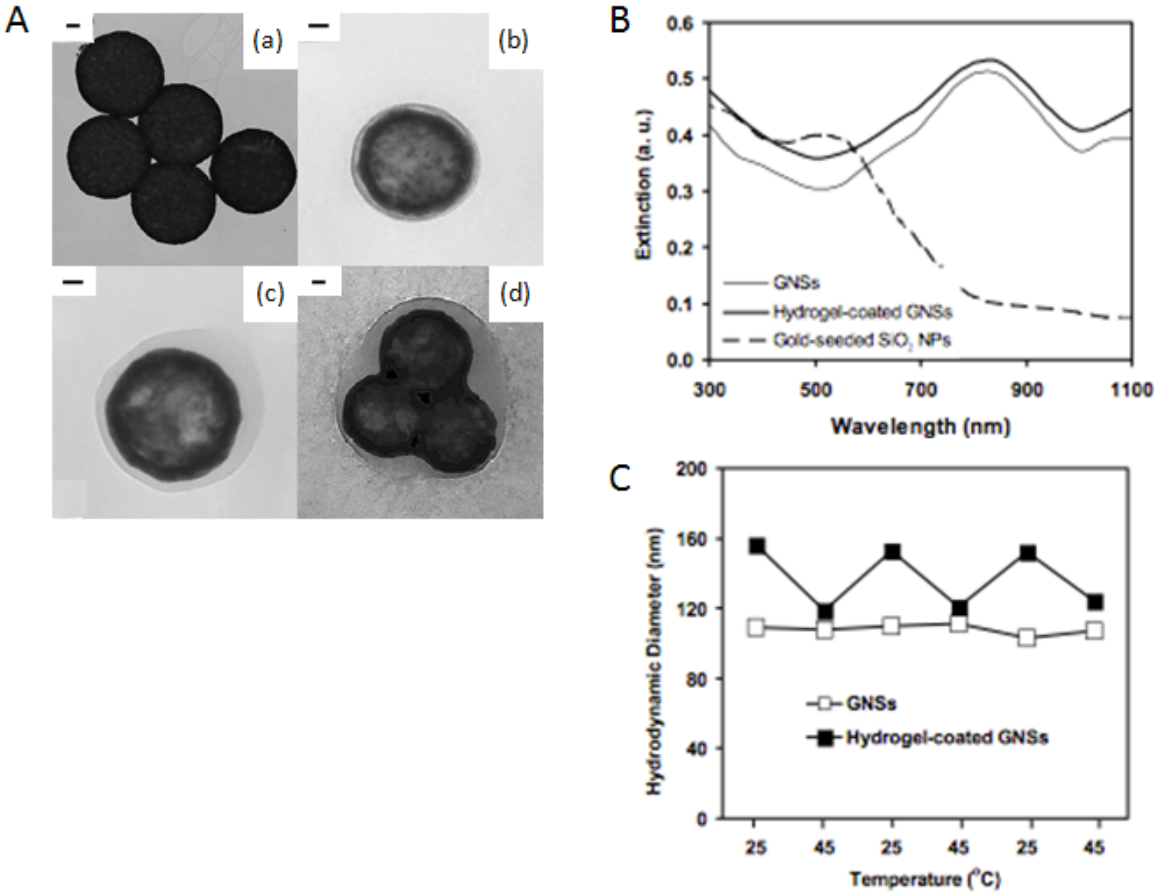

Figure 5.1. Hydrogel coating by surfactant-free emulsion polymerization (SFEP). [A] TEM images of (a) bare nanoshells (diameter~120 nm); (b) thin hydrogel-coated nanoshells (diamter~160 nm); (c) thick hydrogel-coated nanoshells; and (d) multiple encapsulated nanoshells. [B] UV-Vis spectra of gold-seeded silica cores, bare nanoshells, and hydrogel coated nanoshells. [C] Hydrodynamic diameters of bare nanoshells and hydrogel-coated nanoshells as a function of temperature. Adapted from (Kim and Lee, 2008).

5.1.2. Surface-Initiated Atom Transfer Radical Polymerization

Controlled radical polymerization methods such as RAFT, SFEP, and ATRP primarily differ in their method of radical generation. In ATRP, free radical generation

stems from an organic halide undergoing a reversible redox process catalyzed by a transition metal compound, commonly a cuprous halide (Odian, 2004, Xu et al., 2009). The ATRP process is described below in Equations 5.1-5.3:

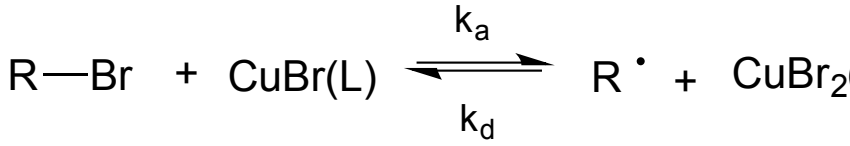

Equation. 5.1

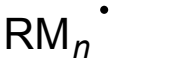

Equation. 5.2

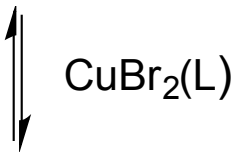

Equation. 5.3

where L is a complexing ligand that helps solubilize the CuBr catalyst in the organic reaction system; k_a and k_d are rate constants for activation and deactivation of the halide initiator; CuBr is the catalyst which undergoes an electron transfer to generate a free radical, R$^{\bullet}$, which then serves to initiate polymerization; M is the monomer; and

$CuBr_2(L)$ is the persistent (metallo)radical that reduces the steady-state concentration of propagating radicals and minimizes normal termination of living polymers (Odian, 2004).

ATRP is capable of producing well-defined polymers with low polydispersities ($M_w/M_n<1.3$), causing it be utilized in applications requiring precisely controlled polymerization (Coessens et al., 2001). This control is based on two principles: (1) initiation should be fast in order to provide a constant concentration of growing polymer chains, and (2) the majority of dormant polymer chains should retain the ability to grow due to the dynamic equilibrium between the dormant species and growing radicals (Xu et al., 2009). When the concentration of propagating radicals is low compared to dormant species, as is seen throughout most of the polymerization process, termination processes are suppressed, allowing for uniformity of polymer growth (Xu et al., 2009). Another advantage is this synthesis allows for mild polymerization conditions; one study by Xia et al. finds that poly(NIPAAm) with a polydispersity of 1.1-1.2 and degree of polymerization of up to 300 can be achieved at room temperature in solvents such as 2-propanol or tert-butyl alcohol (Xia et al., 2005).

Additionally, if the organic halide initiator can be immobilized onto a substrate, polymers can be grafted from the substrate to yield a uniform surface coverage (Xu et al., 2009). Several ATRP initiators have been modified with functional groups to allow for immobilization on various surfaces, including silane-containing initiators for immobilization on silica based surfaces and thiol-containing initiators for immobilization on gold surfaces. In this process, know as surface initiated- atom transfer radical

polymerization (SI-ATRP) polymer growth can be controlled to occur only at distinct spatial locations where the initiator has been immobilized.

Poly(methyl methacrylate) (PMMA) was the first polymer to be synthesized using surface initiated-atom transfer radical polymerization (Edmondson et al., 2004). In this 1998 study, Ejaz et al. immobilized the ATRP initiator 2-(4-chlorosulfonylpenyl) ethyl trimethoxysiline onto an oxidized silicon substrate using the Langmuir-Blodgett (LB) technique and then grew PMMA chains off these sites (Ejaz et al., 1998). Masci et al. reported the first successful polymerization of poly(NIPAAm) using ATRP and mild reaction conditions (room temperature with *N,N*-dimethylformamide [DMF] as the solvent) (Masci et al., 2004).

The formation of poly(NIPAAm)-based polymer brushes off of various surfaces has been widely researched and reported (Edmondson et al., 2004, Wei et al., 2008, Chakraborty et al., 2010, Vasani et al., 2011, Shivapooja et al., 2012). However, synthesis of crosslinked hydrogel networks using SI-ATRP has been considerably less explored (Chirra and Hilt, 2010). A brief discussion of previous instances of poly(NIPAAm)-based hydrogel synthesis via SI-ATRP follows.

5.1.2.1. SI-ATRP of Poly(NIPAAm)-Based Hydrogels on 2D Surfaces

In a recent study by Chirra et al., microcontact printing (μCP) was used to pattern areas of an ATRP initiator (bromoisobutyrate-terminated undecyl disulfide) onto gold films (Chirra et al., 2009). From this, a poly(NIPAAm) hydrogel crosslinked by various (ethylene glycol)-dimethacrylate based molecules were grown. The combination of μCP and ATRP allowed for tight control of polymer growth in both the *XY* (μCP) and *Z*

(ATRP) directions. Analysis via atomic force microscopy (AFM) showed that increasing reaction times increased the overall thickness of the poly(NIPAAm) hydrogel, as shown in Figure 5.2.

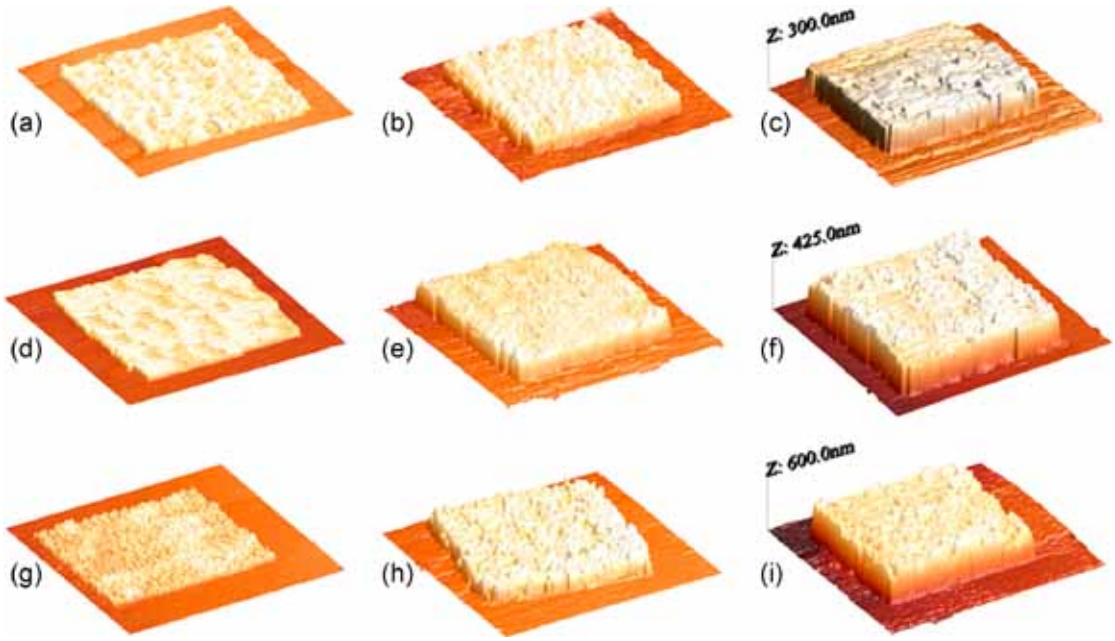

Figure 5.2. Normalized AFM images of poly(NIPAAm) hydrogels crosslinked with ethylene glycol dimethacrylate (EGDMA) (a-c), PEG-200-dimethacyrlate (70:30 mol%) (d-f), and PEG-400-dimethacrylate (90:10 mol%) (g-i). Each pattern is 25 μm long. The EGDMA gels were synthesized for (a) 25 hr, (b) 36 hr, and (c) 48 hr; the PEG200DMA gels for (d) 5 hr, (e) 16 hr and (f) 20 hr; and the PEG400DMA gels for (g) 4.5 hr, (h) 16 hr and (i) 36 hr. From (Chirra et al., 2009).

Further analysis of this system looked at the thermal response of these surface patterned hydrogels (Chirra and Hilt, 2010). As shown in Figure 5.3, increasing the temperature of these patterns decreased the pattern thickness (as measured by AFM). Additionally, hydrogel thickness is also dependent on crosslinking density with lower density and larger crosslinking molecules (PEG600DMA vs PEG400DMA) allowing for

an increased mesh size of the hydrogel, and therefore increased swelling ability and increased thickness (Chirra and Hilt, 2010).

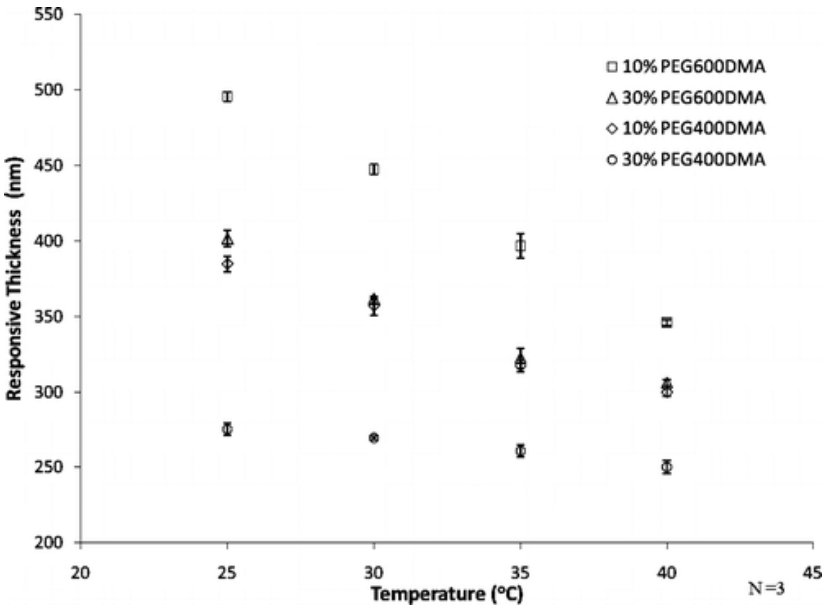

Figure 5.3. Hydrogel thickness (as determined by AFM) at solution temperatures. In addition, amount and type of crosslinker employed also has a large effect on hydrogel thickness. From (Chirra and Hilt, 2010).

5.1.2.2. SI-ATRP of Poly(NIPAAm)-Based Hydrogels on 3D Surfaces (Particle Coatings)

Synthesis of hydrogel coatings using SI-ATRP has also been investigated as tight control of hydrogel thickness can be achieved, providing for monodisperse particles. Wei et al. used this method to create a poly(NIPAAm) coating on NIR absorbing gold nanorods (Wei et al., 2008). This study used gold nanorods with an aspect ratio of 4.4±0.4 and a peak longitudinal plasmon resonance at 843 nm. A disulfide-containing initiator was immobilized onto the gold nanorod surface followed by *in situ* polymerization of poly(NIPAAm). TEM characterization of the particles indicated a core/shell structure was formed, and it was noted that the thickness of the coating could

be tuned by the polarity of the solvent, with more polar solvents yielding thicker coatings. DLS showed an increase in hydrodynamic diameter at temperatures from 32-37^{o}C, indicating the hydrogel coatings had collapsed and become more hydrophobic, causing the particles to precipitate out of solution and aggregate. In addition, a drug loading experiment with the antibiotic norvancomycin showed increased release when the particles were irradiated with an 808 nm laser (Wei et al., 2008).

This method has also been employed using iron oxide nanoparticles. Frimpong et al. demonstrated growth of a PNIPAAm hydrogel with poly(ethylene glycol) 400 dimethacrylate (PEG400DMA) crosslinks using SI-ATRP on iron oxide particles of 6-10 nm diameters (Frimpong and Hilt, 2008). First, particles coated with either oleic acid or citric acid underwent a ligand exchange reaction to coat the surface in bromide-containing initiator molecules. Next, an ATRP reaction was carried out to form a poly(NIPAAm-PEG400DMA) coating. High-resolution TEM analysis indicated the resulting particles consist of an ordered crystalline core next to an amorphous polymer shell less than 5 nm thick. DLS analysis showed larger hydrodynamic diameters of these particles at temperatures at 20-30 ^{o}C, while smaller hydrodynamic diameters were observed at temperatures above the hydrogel LCST (Frimpong and Hilt, 2008).

Similar studies synthesizing hydrogel coatings via SI-ATRP have also been reported (Li et al., 2004, Li et al., 2007, Dong et al., 2008), however aggregation issues due to interparticle interactions during the growth of the hydrogel coatings and multiple processing steps often lead to low yields (Li et al., 2007, Chirra et al., 2012). To remedy this, Chirra et al. proposed a novel solution in which gold nanoparticles are first stabilized

in a flexible hydrogel matrix prior to initiator immobilization and polymer growth (Chirra et al., 2012). This scheme, named "Isolate, functionalize, and release" or "ISOFURE", is summarized in Figure 5.4. This ISOFURE scheme served as an inspiration for the synthesis process described in this chapter.

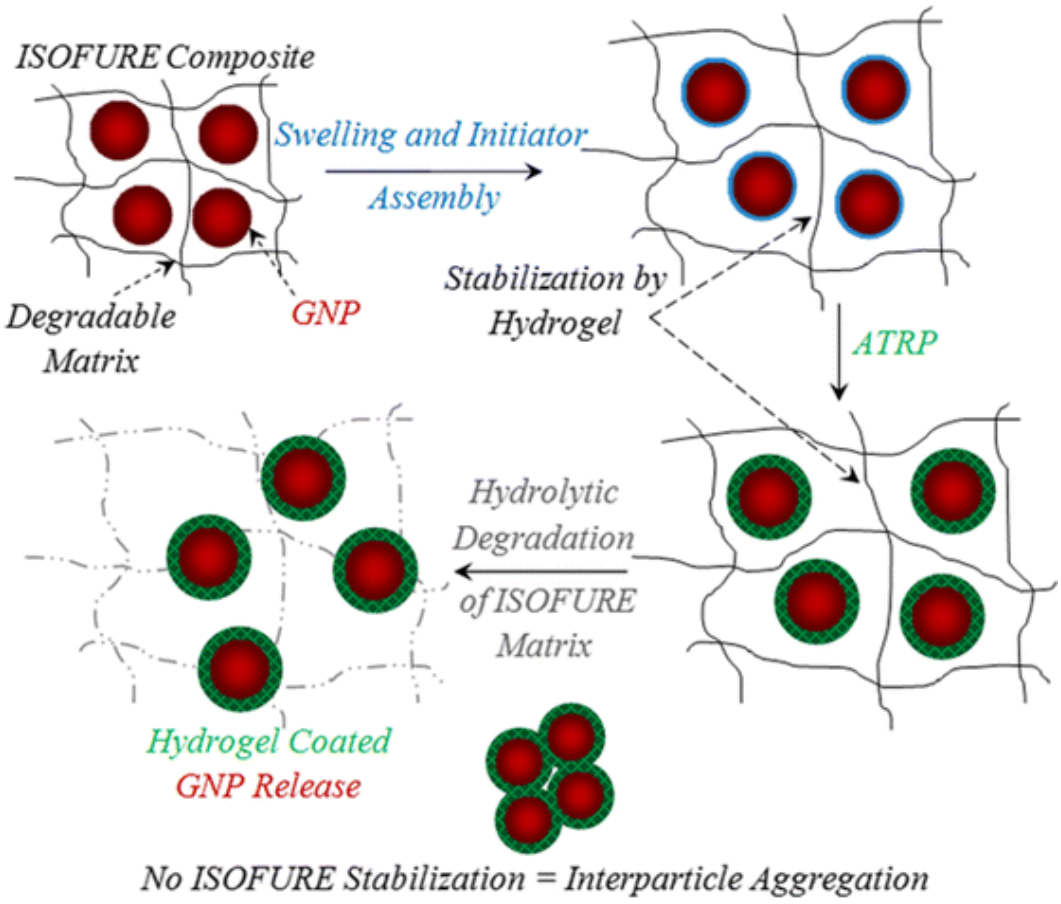

Figure 5.4. Schematic of ISOFURE. Gold nanoparticles are first encapsulated in a hydrolytically degradable poly(ethylene glycol diacrylate-co-isobutyl amine) hydrogel. The hydrogel network is then swelled, allowing initiator assembly and ATRP of a poly(NIPAAm)-based hydrogel coated to take place within the network. After polymerization, the poly(ethylene glycol diacrylate-co-isobutyl amine) matrix is degraded via hydrolysis and the poly(NIPAAm)-coated gold nanoparticles are collected. From (Chirra et al., 2012).

5.2. Materials and Methods

All reagents were purchased from Sigma-Aldrich and used as received, unless otherwise noted. All water used in synthesis, purification, and testing was treated by a Milli-Q system (≥18.0 MΩ·cm resistivity).

In the ISOFURE method described previously, the sacrificial matrix was poly(ethylene glycol diacrylate-co-isobutyl amine). This hydrogel was synthesized using free radical polymerization requiring the addition of chemical initiators (APS and TEMED). Additionally, while this matrix was hydrolytically degradable, degradation was a slow process that took up to 72 hr (Chirra et al., 2012). For these reasons, a Ca^{2+}-alginate hydrogel was chosen for the sacrificial matrix, which allows for milder crosslinking conditions and a faster reversal of gelation.

Alginate is a water-soluble polysaccharide consisting of mannuronic and guluronic acid residues (Figure 5.5A). Alginate is widely available commercially, commonly extracted from species of brown algae and packed as a salt with cations such as Na^{+}. If two gluruonic acid residues are aligned side by side, a hole emerges which is the ideal for cooperative binding of calcium ions (George and Abraham, 2006). Gelation and crosslinking of alginate occurs in the presence of a divalent cation such as Ca^{2+}, where the Ca^{2+} displaces the sodium ions associated with the gluruonic acid residues. This in turn induces stacking of multiple gluruonic acid residues and physical crosslinking of multiple alginate chains (Figure 5.5B). The resulting material is a stable hydrogel that maintains its shape and resists stress (George and Abraham, 2006).

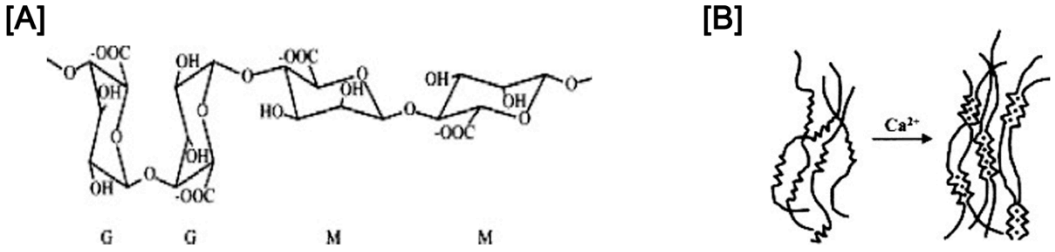

Figure 5.5. Structure of Ca^{2+}-alginate gels. [A] Chemical structure of alginate shown as two guluronic acid residues (G) and two mannuronic acid residues (M). [B] The addition of calcium ions causes cooperative binding of multiple gluruonic acid residues resulting in physical crosslinking of alginate chains into a stable hydrogel network. Adapted from (George and Abraham, 2006).

Alginate hydrogels are commonly formed as "beads" by dripping a solution of sodium alginate into a solution containing calcium ions, commonly $CaCl_2$ (Kuo and Ma, 2001). Additionally, these hydrogels can be quickly degraded by the addition of a calcium-chelating agent, such as ethylenediaminetetraacetic acid (EDTA). These reactions are mild enough to be used to encapsulate and release cells (Bonaventure et al., 1994).

5.2.1. Ca^{2+}-Alginate Encapsulation

Gold-silica nanoshells were synthesized using the methods outlined in Chapter 2. Next, a 50 ml solution containing 1.5 wt% sodium alginate and nanoshells at an O.D. of 2 (5.8×10^9 nanoshells/ml) was prepared in H_2O. This solution was then added dropwise to 100 ml of 1 wt% $CaCl_2$ in H_2O under rapid stirring. This resulted in the formation of many small Ca^{2+}-alginate-nanoshell hydrogel "beads". The reaction mixture was stirred for 15 min after which the Ca^{2+}-alginate-nanoshell "beads" were collected by filtration and rinsed 3 times with H_2O.

5.2.2. Initiator Immobilization

Next, the initiator bis[2-(2'bromoisobutryloxy)ethyl]disulfide (subsequently referred to as Br-initiator; ATRP solutions, Pittsburg, PA) was immobilized onto the surface of the gold-silica nanoshells via gold-thiol interactions. First, a 50 ml solution containing 20 mM Br-initiator and 10 mM tris(2-carboxyethyl)phosphine (TCEP) (Thermo Fisher Scientific) in 1:1 EtOH:H_2O was incubated at RT for 60 min. This step serves to reduce the disulfide bond in the Br-initiator, resulting in two molecules with terminal thiol groups that can then assemble onto the gold-silica nanoshells through gold-thiol interactions, as illustrated in Figure 5.6.

For immobilization onto the gold-nanoshell surface, the Ca^{2+}-alginate-nanoshell hydrogels were soaked in this Br-initiator/TCEP solution and rocked overnight at 4 ^{o}C. The next day, the gels were washed 3 times with EtOH followed by 3 times with H_2O to remove any non-immobilized molecules.

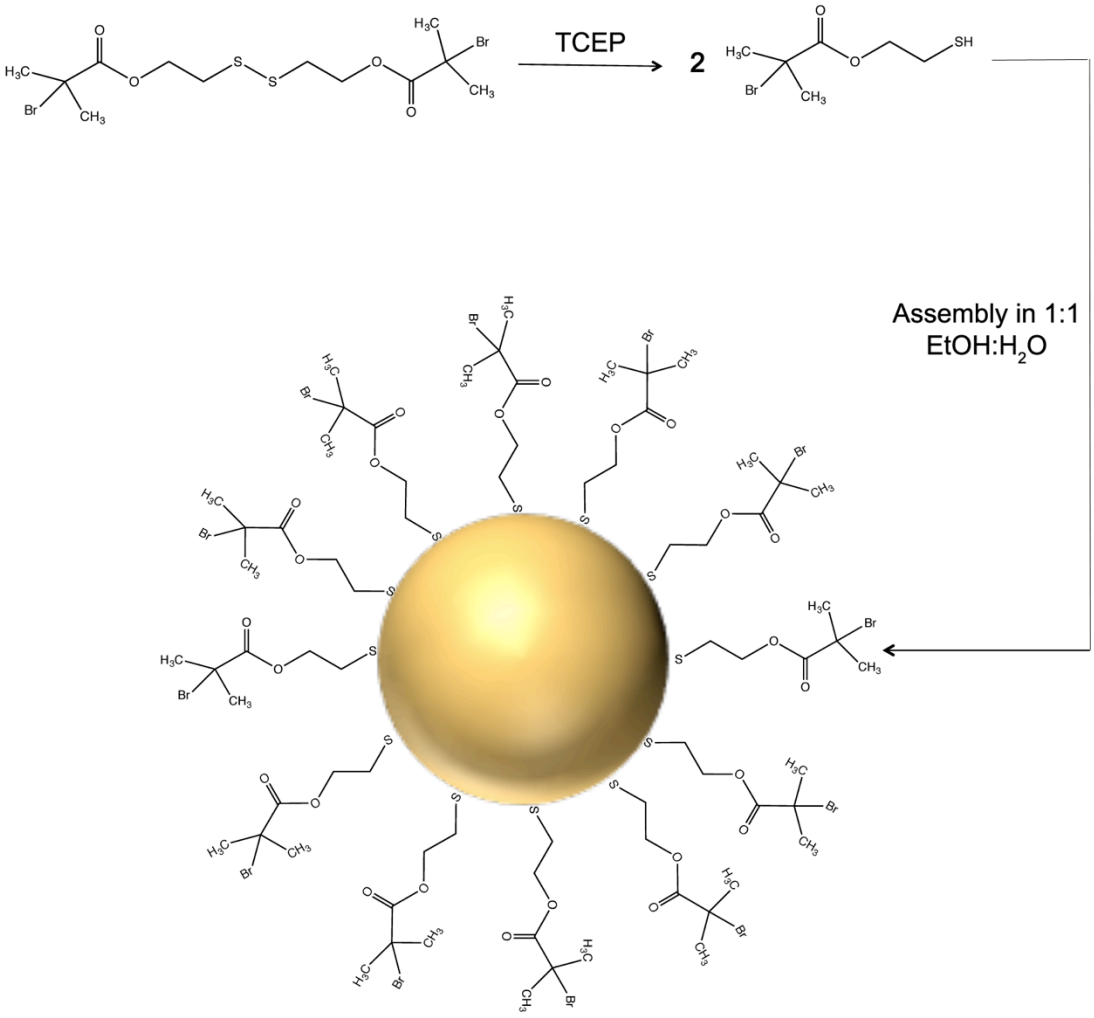

Figure 5.6. Immobilization of Br-initiator onto gold-silica nanoshells. The disulfide bond within the Br-initiator molecule is first reduced using TCEP, and the resulting molecules are then assembled onto the nanoshell surface via gold-thiol interactions.

5.2.3. Polymerization using ATRP

The Ca^{2+}-alginate hydrogels containing the Br-initiator immobilized nanoshells were soaked in a 100 ml solution of 98:2 MeOH:H_2O (v/v) in a three-neck round bottom flask. Under rapid stirring, the flask was evacuated and Ar gas was bubbled through the

solution for 30 minutes to remove dissolved O_2. After 30 min, the ATRP reaction components described in Table 5.2 were added to the flask. For this polymerization reaction, the same 95:5 NIPAAm:AAm and 1:750 MBAAm:monomers ratios as have been previously described were used. The flask was again evacuated and Ar was bubbled for an additional 30 min. The reaction mixture was then stirred at 1000 rpm for 18 h.

Table 5.2. ATRP reaction components.

Component	Concentration	Purpose
NIPAAm	23.75 mM	Monomer
AAm	1.25 mM	Monomer
MBAAm	0.0333 mM	Crosslinker
CuBr	0.2 mM	Catalyst
2,2'-bipryidine	0.6 mM	Complexing ligand
$CuBr_2$	0.02 mM	Persistent (metallo)radical

After 18 h, the reaction was stopped by opening the flask to air. The Ca^{2+}-alginate hydrogels were collected by filtration, and then rinsed 5 times with MeOH followed by 5 rinses with H_2O to remove any unreacted components.

5.2.4. Dissolution of Ca^{2+}-Alginate and Particle Collection

After the ATRP reaction, the Ca^{2+}-alginate hydrogel was dissolved and the encapsulated poly(NIPAAm-co-AAm)-coated gold nanoshells (NCNS) were collected. The Ca^{2+}-alginate-nanoshell beads were soaked in 50 ml of 100 mM EDTA in TBS. This solution was vortexed for 1 min and then rocked at RT for 30 min to allow for sufficient chelation of the Ca^{2+} ions and dissolution of the Ca^{2+}-alginate hydrogels. The NCNS were then collected via 2 rounds of centrifugation (735 x g, 15 min) and the solution was passed through a 5 μm polycarbonate membrane filter. This entire synthesis process is summarized in Figure 5.7.

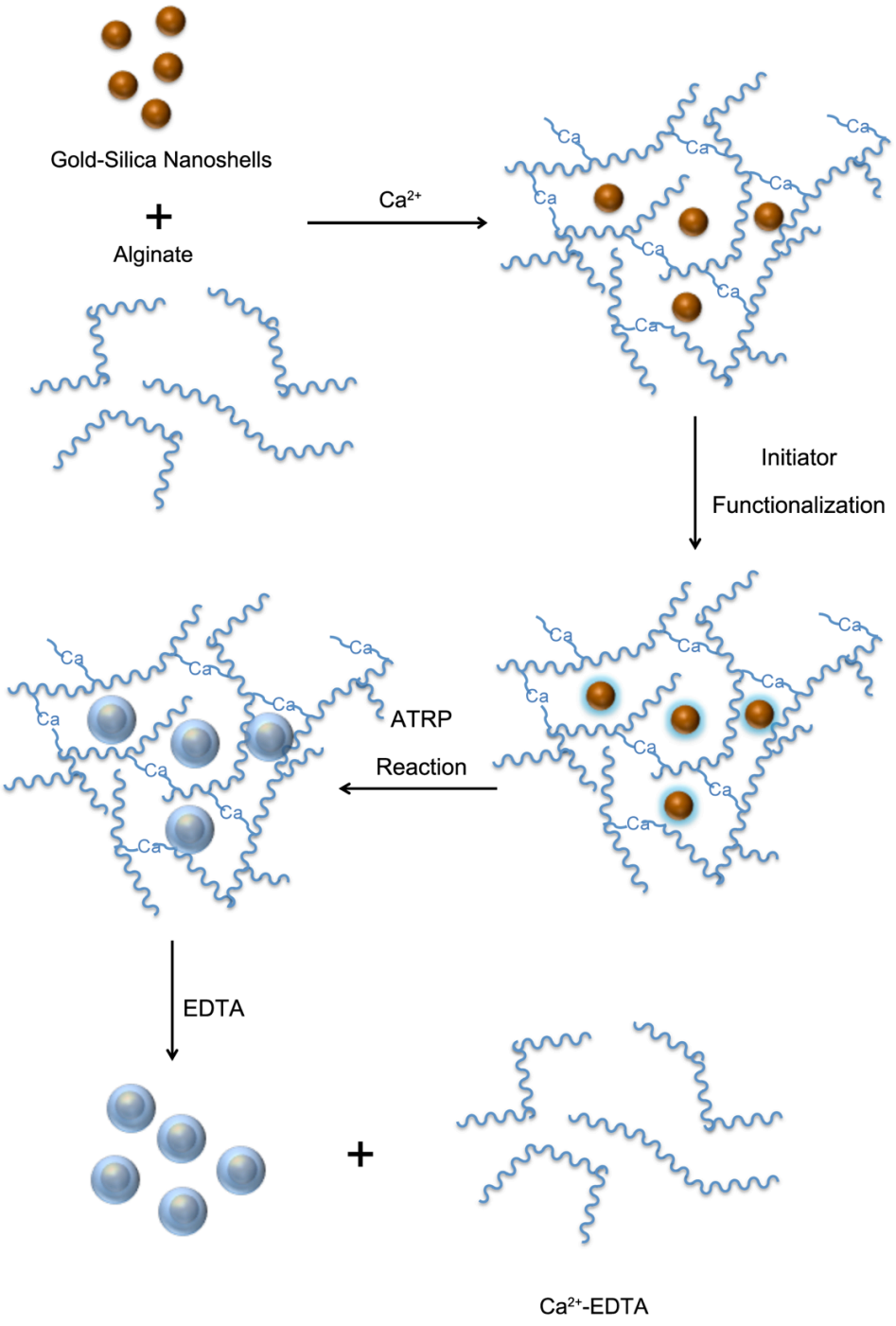

Figure 5.7. Synthesis of NCNS via SI-ATRP. Nanoshells are first encapsulated in Ca^{2+}-alginate hydrogels. Within this hydrogel matrix, initiator immobilization onto the nanoshells and ATRP growth of poly(NIPAAm-co-AAm) is carried out. After polymerization is complete, the Ca^{2+}-alginate is dissolved by the addition of EDTA and the NCNS are collected.

5.2.5. Particle Characterization

Bare nanoshells, initiator-functionalized nanoshells, and NCNS were characterized using UV-Vis spectroscopy, DLS, zeta potential analysis, and TEM. Extinction spectra from 400-1000 nm were collected using a Cary 50 Varian spectrophotometer. DLS and zeta potential were measured using a Malvern Zetasizer Nano ZS. For DLS measurements, the refractive index of gold at 633 nm (the incidence of the detection laser) was used ($0.2 + 3.32i$) (Schulz and Tangherlini, 1954, Schulz, 1954), and the Z-average size is reported. An FEI Tecnai G^2 Twin was used for TEM imaging.

5.2.6. Multiphoton Imaging of NCNS

Since gold-silica nanoshells display two-photon induced photoluminescence (Park et al., 2008, Coughlin et al., 2014), multiphoton microscopy was employed to visualize the NCNS in their hydrated state. To visualize both the gold-silica nanoshell core and hydrogel coating simultaneously, a FITC-tagged dextran was soaked into the hydrogel coating.

NCNS were pelleted and soaked in an aqueous solution containing 1 mg/ml FITC-dextran (3000 MW, Life Technologies) at 4 ^{o}C for 7 days. The particles were then purified by two rounds of centrifugation (735 x g, 15 min). Next, FITC-dextran loaded NCNS and non-loaded NCNS were encapsulated in poly(ethylene glycol diacrylate) (PEGDA) hydrogels to constrain passive particle movement during imaging. Particles were suspended in a 20 wt% solution of PEGDA (6 kDa) at an O.D. of 0.6 (1.4×10^9 particles/ml). A photoinitiator solution was prepared containing 2,2-dimethyoxy-2-

phenylacetophenone in N-vinylpyrrolidone at a concentration of 300 mg/ml. Next, 2 μl of this photoinitiator solution was added to 100 μl of the PEDGA-NCNS suspension and exposed to UV light for 60 s to allow for crosslinking of a PEGDA network with encapsulated NCNS.

NCNS with and without FITC-dextran were then imaged using an Olympus FV1000 Multiphoton microscope with a Chameleon femtosecond Ti:Saph laser (Coherent, 680-1080 nm). The gold-silica nanoshells were imaged by exposure at 810 nm and collection from 575-630 nm, while signal from the FITC-dextran was imaged by exposure at 920 nm and collection from 495-540 nm.

5.2.7. Thermal Deswelling Analysis

DLS measurements were used to investigate changes in particle size in response to increased temperatures as well as NIR irradiation. Measurements were taken at various temperatures (25 ^{o}C, 37 ^{o}C, 45 ^{o}C, 50 ^{o}C, 55 ^{o}C, and 60 ^{o}C) as well after particles were exposed to NIR irradiation (Coherent Diode, 808 nm, 4 W/cm^2, 2 min). Temperatures were maintained for at least 15 min before a reading was taken. Z-average hydrodynamic diameters of all groups were compared using an ANOVA with Tukey's HSD (*$p<0.05$).

5.3. Results

5.3.1. Particle Characterization

The extinction spectra of bare nanoshells, initiator-functionalized nanoshells, and NCNS are shown in Figure 5.8. Bare nanoshells were found to have a peak extinction at 785 nm. This spectrum did not change significantly for the initiator-functionalized and NIPAAm-coated nanoshells; only a slight peak broadening towards the red was observed.

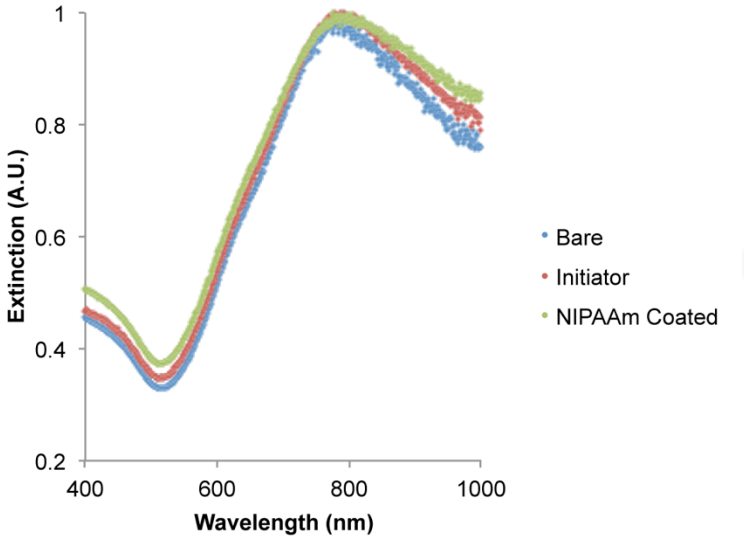

Figure 5.8. Extinction spectra of bare, initiator functionalized, and NIPAAm coated nanoshells.

Bare, initiator-functionalized, and NIPAAm-coated nanoshells were analyzed using both DLS and zeta potential measurements (Figure 5.9). A slight increase in hydrodynamic diameter was seen between the bare and initiator-functionalized nanoshells (158.6 nm vs. 187.8 nm), with a much larger size seen with the NCNS (337.4 nm). Similarly, an increase in surface charge was observed when functionalizing the nanoshells with the Br-initiator molecule (-48.5 mV for bare nanoshells vs. -27.0 mV for initiator-functionalized nanoshells).

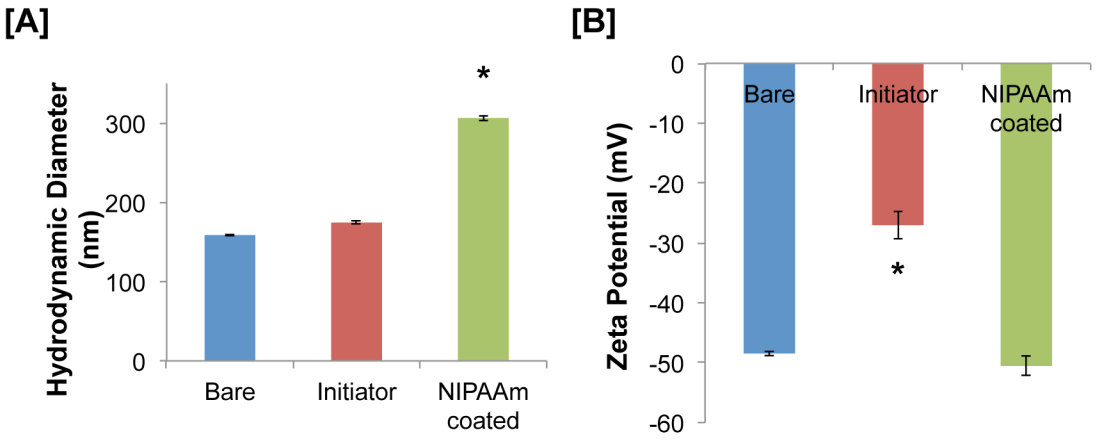

Figure 5.9. [A] DLS and [B] zeta potential measurements of bare, initiator functionalized, and NIPAAm coated nanoshells.

Figure 5.10 shows TEM images of bare, initiator-functionalized, and NIPAAm-coated nanoshells. Both the bare and initiator-functionalized nanoshells look very similar, as the initiator molecule is too small to be visible. However, the NCNS display a thin polymer coating around the electron dense gold nanoshell. These images were taken under vacuum, and therefore the hydrogel layer was fully dehydrated, leading the hydrogel coating appearing much thinner than it did under DLS analysis.

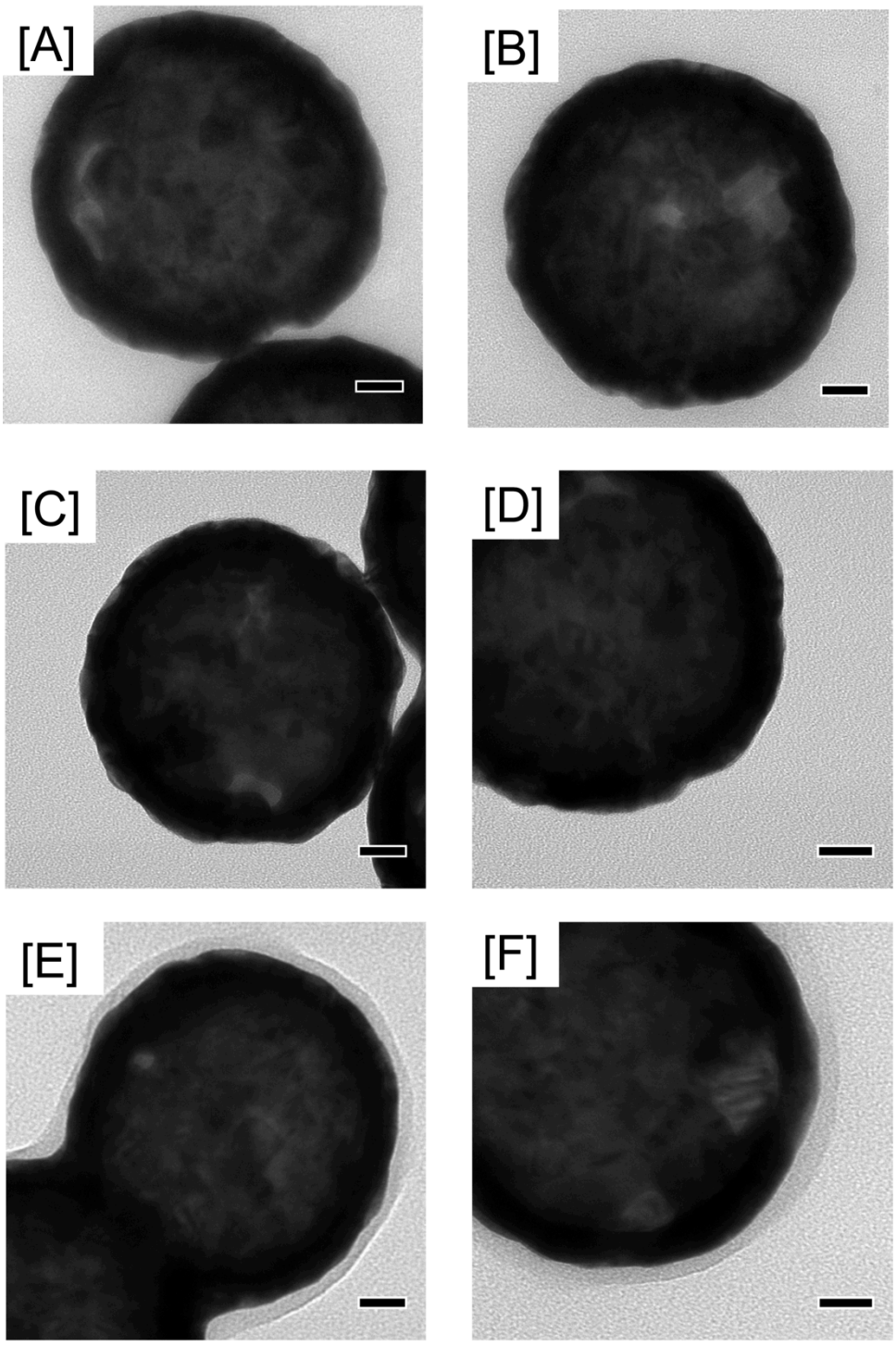

Figure 5.10. Representative TEM images of [A-B] bare, [C-D] initiator functionalized, and [E-F] NIPAAm coated nanoshells. Scale bars = 20 nm.

5.3.2. Multiphoton Imaging

In order to observe the NCNS in their hydrated state, multiphoton microscopy was employed (Figure 5.11). NCNS loaded with FITC-dextran [Figure 5.11A-D] displayed colocalized signals from both 2-photon induced luminescence of the gold-silica nanoshells (red, D) and fluorescence from the FITC-dextran loaded coating (green, C). Non-loaded NCNS (Figure 5.11E,F) displayed the signal from the gold-silica nanoshells (red, H) but minimal green signal (G) as no FITC-dextran was present.

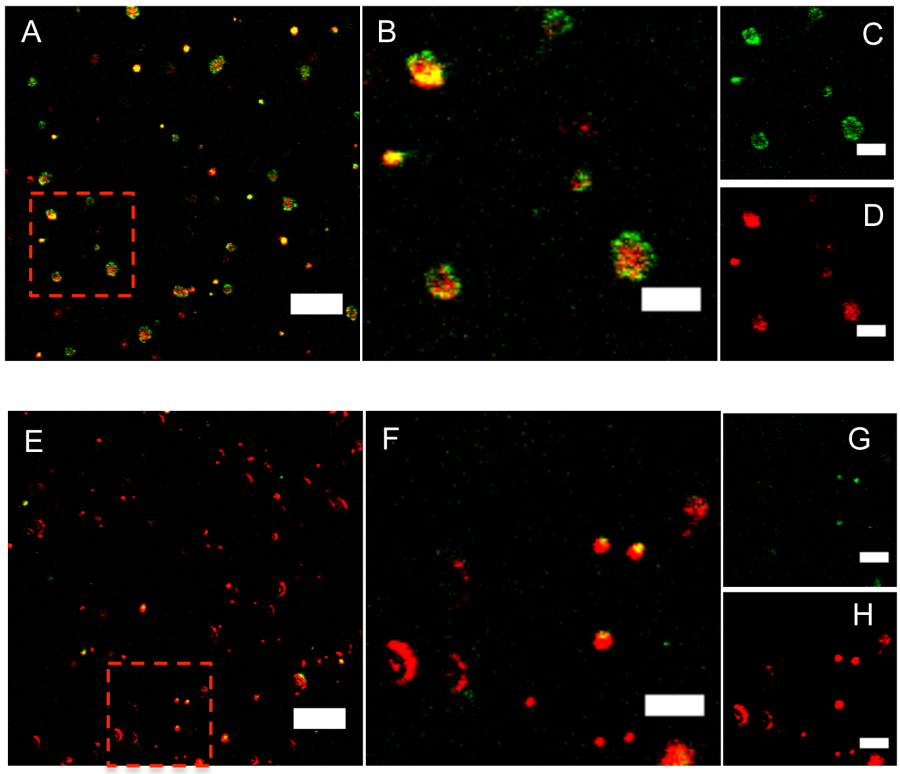

Figure 5.11. Multiphoton images of FITC-loaded NCNS [A-D] and non-loaded NCNS [E-H]. [A] Signal from the gold-silica nanoshells core (red) overlayed with signal from FITC-dextran (green) indicates colocalization of both sigals. [E] Non-loaded NCNS display gold-nanoshell signal (red) with minimal FITC signal (green). [B-D; F-H] Inset indicated by red box in [A,E] showing FITC-dextran signal [C,G], gold-nanoshell signal [D,H], and overaly of both signals [B,F]. Scale bars = 15 μm (A,E) and 5 μm (B-D, F-H).

5.3.3. Thermal Deswelling Analysis

The Z-average size, intensity-weighted size, and polydispersity index (PDI) of all sample groups are displayed in Table 5.3. Particle sizes ranged from 326 nm at 25 ^{o}C to 270-280 nm after incubation at 60 ^{o}C or exposure to NIR irradiation, indicating that these particles display the same thermal properties as was seen in the bulk hydrogel-nanoshell composites described in Chapter 2. Figure 5.12 illustrates particle size dependence on temperature.

Table 5.3. Particle size dependence on temperature and NIR exposure.

Group	Z-Average (nm)	Intensity-weighted Average (nm)	PDI	n=
25 ^{o}C	326.33 ± 16.51	333.96 ± 28.34	0.190 ± 0.030	8
37 ^{o}C	312.84 ± 14.40	301.13 ± 15.68	0.205 ± 0.003	3
45 ^{o}C	305.27 ± 11.20	294.53 ± 11.38	0.186 ± 0.002	3
50 ^{o}C	297.06 ± 10.84	286.34 ± 11.60	0.184 ± 0.012	3
45 ^{o}C	288.97 ± 10.49	279.27 ± 18.51	0.159 ± 0.034	3
60 ^{o}C	280.32 ± 5.62	273.51 ± 8.06	0.172 ± 0.009	3
Post Irradiation	270.65 ± 16.21	253.48 ± 14.30	0.219 ± 0.029	4

Further, no significant size differences were seen between particles incubated at 25 ^{o}C or 37 ^{o}C, indicating the particles will be in their swollen state under physiological conditions. Particles exposed to NIR irradiation have a smaller diameter ($p<0.02$) compared to particles at 25 ^{o}C or 37 ^{o}C, indicating these particles have undergone the phase transition, releasing water from the poly(NIPAAm-co-AAm) coating (Figure 5.13).

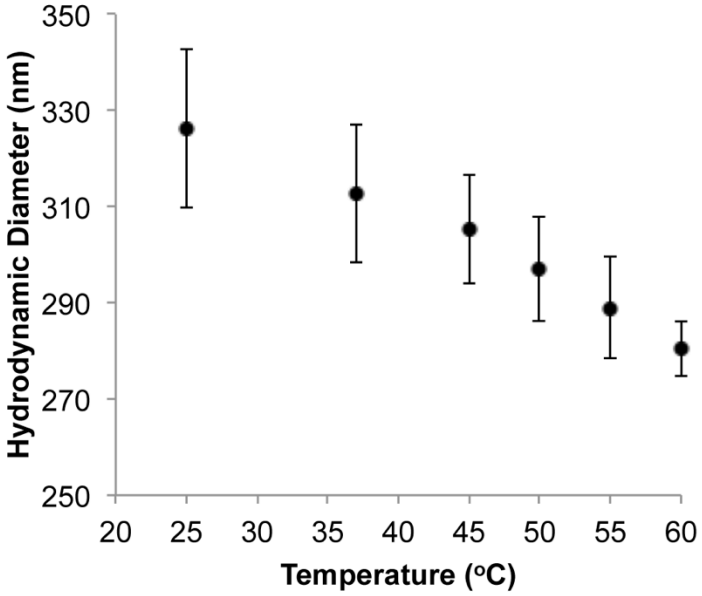

Figure 5.12. Z-Average particle hydrodynamic diameter vs. temperature.

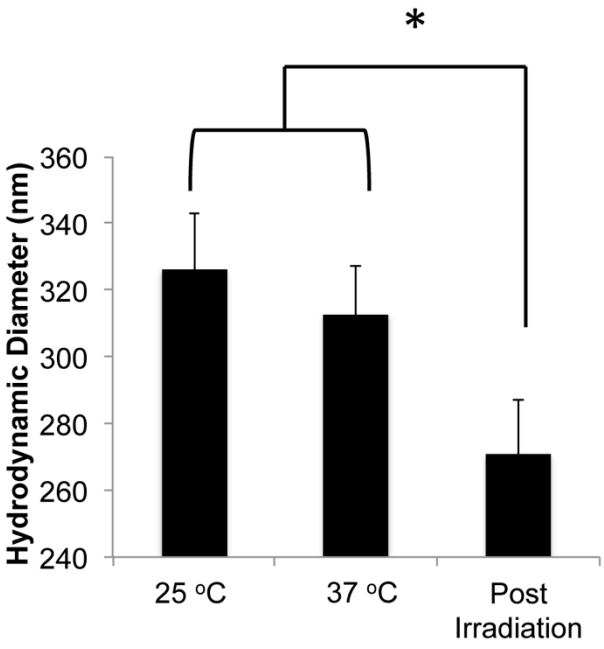

Figure 5.13. Z-average hydrodynamic diameters of particles at 25 °C, 37 °C, and after exposure to NIR irradiation. Particles at 25 °C and 37 °C are not significantly different in size, but are both significantly larger than particles exposed to NIR irradiation. (*$p<0.01$, ANOVA).

As was discussed in Chapter 4, these DLS measurements are dependent on many factors, including particle geometry and material refractive index, and therefore may not truly represent the particle's real "size". Furthermore, only a modest decrease in hydrodynamic diameter (~60 nm) was observed in response to elevated temperatures or NIR irradiation. While the collapse of the hydrogel coating may be very extensive, these modest changes in overall particle size are due to the fact the majority of the particle's volume is made up the incompressible nanoshell.

5.4. Discussion and Conclusions

In this chapter, the composite material developed in Chapter 2 of this dissertation was synthesized as a thin poly(NIPAAm-co-AAm) hydrogel coating onto individual gold-silica nanoshells using a controlled polymerization technique known as SI-ATRP. Analysis by DLS showed that particles increased in size from ~160 nm to over 300 nm with the addition of this coating. Further analysis by TEM indicates that these particles consist of an electron dense gold nanoshell core surrounded by a thin polymer layer. Further, the hydrodynamic diameter of these particles decreases in response to elevated temperatures and NIR irradiation, as was seen in the bulk composite material. Further, the size of these particles (~330 nm) should allow for use as an injectable platform.

Both the SI-ATRP method used in this chapter and the hydrogel-template method described in Chapter 4 are capable of synthesizing of injectable-sized hydrogel-nanoshell composite particles. A detailed comparison of these two methods can be found in Table 5.2. While the hydrogel template method allows for fabrication of particles in a wide

variety of shapes and sizes, it is limited by its lack of control over the number of nanoshells per hydrogel particle and difficulties regarding batch-size scale-ups.

Table 5.4. Comparison of composite particle synthesis methods.

	Hydrogel-nanoshell composite particles (HNCPs, Ch. 4)	Poly(NIPAAm)-coated nanoshells (NCNS, Ch. 5)
Synthesis	Composite particles polymerized in microfabricated hydrogel template	Hydrogel synthesized off nanoshell surface via immobilized initiator molecule
Particle geometry	Can synthesize particles of any geometry that can be microfabricated into a mold	Limited to geometry of metal nanoparticle core (sphere)
Nanoshell loading	Nanoshell distribution within particle population not controlled	Single nanoshell per composite particle
Scale-up considerations	Synthesis done on 2D surface—difficult to scale up	Synthesis done in solution—ease of scale up

As the NCNS synthesized by SI-ATRP consist of a single nanoshell per hydrogel particle and are synthesized in solution, rather than a 2D surface, which facilitates scaling up the number of particles synthesized per reaction, these particles were further investigated for their drug loading and release capabilities. Next, the ability to load these particles with a cancer therapeutic (doxorubicin), release of this drug upon NIR irradiation, and *in vitro* validation of this platform using a murine colon carcinoma model was assessed. The results of these investigations will be discussed in Chapter 6.

6. Hydrogel Coated Nanoshells: Drug Loading and Release, *in vitro* Validation

Successful tumor-targeted drug delivery carriers must meet four basic requirements: (1) *retain* (the drug during circulation), (2) *evade* (the body's defenses), (3) *target* (the tumor tissue/vasculature), and (4) *release* (the drug, specifically at the tumor site) (Needham, 1999). The NCNS developed in Chapter 5 were designed to *retain* drug in the poly(NIPAAm-co-AAm)-hydrogel coating, *target* tumor tissue through the EPR effect (as they are synthesized as sub-500 nm particles), and *release* the drug payload upon NIR exposure. Furthermore, it is hypothesized that the poly(NIPAAm-co-AAm)-hydrogel coating will act to help stabilize the particles and *evade* clearance from the bloodstream similarly to the PEG brushes utilized on many nanoparticle platforms.

In previous studies utilizing gold-silica nanoshells, the particle surface is passivized the addition of PEG brushes to the nanoparticle surface. This coating serves several purposes, including preventing the nanoparticles from aggregating in the presence of physiological salt concentrations. Additionally, when these particles are injected *in vivo* this coating serves to minimize plasma protein adsorption. Furthermore, it has been shown that PEG coatings not only limit adsorption of blood proteins, but this in turn also results in a decrease in particle phagocytosis by macrophages (Zahr et al., 2006). *In vivo*, this prevents early clearance via the RES system, allowing for longer circulation times and increased tumor accumulation of particles.

This chapter further evaluates the ability of NCNS to act as a drug delivery carrier. First, the stability of the particles under physiological salt conditions as well as

material cytotoxicity was evaluated. Next, the ability to load doxorubicin into the NCNS and trigger its release by NIR light exposure was analyzed. Finally, the ability for this platform to deliver doxorubicin and elicit a therapeutic effect to colon carcinoma cells *in vitro* was confirmed.

6.1. Materials and Methods

6.1.1. Material Stability

The poly(NIPAAm-co-AAm) hydrogel coating on the NCNS was hypothesized to prevent particle aggregation under physiological salt concentrations similarly to the PEG coatings used in previous gold-silica nanoshell studies. Therefore, particle stability of bare nanoshells, PEG-coated nanoshells, and NCNS in 100 mM NaCl was assessed.

6.1.1.1. Synthesis of PEG-coated nanoshells

Gold-silica nanoshells (synthesis described in Section 2.4.1) were functionalized with PEG molecules via gold-thiol interactions. Methoxy-PEG-SH (mPEG-SH, 5000 Da, Laysan Bio) was dissolved in H_2O at a concentration of 10 μM. Next, 1 ml of this mPEG-SH solution was added to 9 ml of nanoshells at O.D. of 1.5 (4 x 10^9 particles/ml) and vortexed for 30 s. The solutions were then rocked overnight at 4 ^oC, and the next day the particles were purified from unreacted PEG molecules by centrifugation (735 x g, 5 min).

6.1.1.2. Analysis of Particle Stability

The quality of surface passivation can be assessed by analysis of particle behavior in a salt solution. When suspended in salt, nanoparticles that are not properly stabilized will form multi-particle aggregates, which in turn results in lowered peak extinctions. Therefore, UV-Vis spectroscopy was used to analyze the stability of nanoparticles with

different surface coatings. Bare nanoshells, PEG-passivated nanoshells, and NCNS were each suspended in 100 mM NaCl, and a UV-Vis spectrometer (Cary 50 Bio, Varian) was used to record the particle spectra every 60 min over 4 h. Stability was calculated for each time point by expressing the peak extinction at that time point as a percent of the peak extinction of that sample at the start of the test.

6.1.2. Material Cytotoxicity

In order to predict if any adverse reactions would occur *in vivo* upon exposure to the NCNS developed in Chapter 5, particle cytotoxicity was analyzed using the MTS assay, an established method for determining nanoparticle toxicity (Lewinski et al., 2008). This colormetric assay measures metabolic activity, as tetrazolium salt is cleaved in the mitrochondria of living cells to produce a dark-blue formazan product, and can therefore be used to estimate the degree of cell viability in a sample. Cytotoxicity was analyzed against two different cell lines: mouse embroyonic fibroblasts (NIH 3T3s), a generic cell line commonly used in many cytotoxicity assays, and human hepatocarcinoma cells (HepG2s), as these cells have similar responses to hepatocytes and liver uptake of these particles is expected. Furthermore, both these cell types are common cell lines used for establishing nanoparticle toxicity (Lewinski et al., 2008). Both cell types were cultured in Dulbecco's Modified Eagle Medium (DMEM) with 10% FBS, 100 U/l penicillin, and 100 mg/ml streptomycin. Cultures were maintained at 37 ^{o}C and 5% CO_2.

Cells were seeded at 4500 cells/well (3T3s) or 9000 cells/well (HepG2s) in 96-well plates. A lower concentration of 3T3 cells were seeded, as these fibroblasts are much

larger in size than the HepG2 cells. The next day, cells were exposed to particle concentrations of 0, 3750, 7500, or 15000 NCNS/cell with media/particle volumes of 120 μl/well, with each condition tested in triplicate. After 48 hr, 26 μl of MTS reagent (Promega) was added to each well and the cells were incubated for 45 min at 37 ^{o}C and 5% CO_2. Media samples were then centrifuged (735 x g, 5 min) in order to pellet any nanoparticles in the suspension. Absorbance readings of the supernatant were measured at 490 nm. Cell viability was then determined by measuring the average OD_{490} value for each treatment group and expressing the values as a percent of the average OD_{490} for the cell-only controls.

6.1.3. Therapeutic Loading and Release

Next, the ability to load and release doxorubicin from the NCNS was assessed. For loading, the NCNS were first pelleted by centrifugation (735 x g, 15 min) and resuspended in a 2 mg/ml solution of doxorubicin in TBS. This suspension was then rocked at 4 ^{o}C for 72 hr to allow for sufficient loading of the doxorubicin into the particles. After 72 hr, the doxorubicin-loaded NCNS were purified by 3 rounds of centrifugation (735 x g, 15 min). The amount of doxorubicin loaded into the particles was determined using UV-Vis spectroscopy. The doxorubicin-loaded particles displayed two distinct spectral peaks: a peak at 785 nm (the peak extinction of the NCNS) was used to determine the particle concentration, and a second peak at 485 nm was used to determine doxorubicin concentration.

For release studies, doxorubicin-loaded NCNS were suspended in TBS at an OD of 0.5 (1.2 x 10^9 particles/ml). 500 μl aliquots of this suspension were either (1) exposed

to an NIR laser (Coherent, 808 nm, 4 W/cm^2) for 3 min, (2) left at room temperature for 3 min, or (3) left at room temperature for 72 hr, with each condition tested in triplicate. After exposure, the suspension was filtered through a 0.22 μm polyethersulfone membrane (Genesse Scientific) to separate the doxorubicin-loaded NCNS from the free doxorubicin in the sample. Doxorubicin content of the samples was then determined by measuring absorbance at 485 nm. The amounts of doxorubicin delivered under the three conditions were analyzed by an ANOVA with Tukey's HSD.

6.1.4. *In vitro* Validation

Murine colon carcinoma cells (CT-26.WT cells, ATCC) were cultured in RPMI 1640 media supplemented with 2 mM L-glutamine, 10 mM HEPES, 1 mM sodium pyruvate, 4.5 g/l glucose, 1.5 g/l sodium bicarbonate, 100 U/l penicillin, 100 mg/ml streptomycin, and 10% FBS. Cultures were maintained at 37 ^{o}C with 5% CO_2. Cells were seeded at a density of 4000 cells/well in either fibronectin-coated 96-well plates (for cell proliferation assay and fluorescence imaging) or fibronectin-coated 8-well chamber slides (for darkfield imaging). Cells were allowed to adhere overnight before particle dosing, and each experimental group was assessed in triplicate.

6.1.4.1. Particle Dosing and NIR Exposure

Cells were exposed to six different experimental conditions: (1) NCNS loaded with doxorubicin, exposed to NIR irradiation, (2) NCNS loaded with doxorubicin (no irradiation), (3) NCNS, exposed to NIR irradiation, (4) 29 μg/ml free doxorubicin (~50 nM, equivalent to the amount of doxorubicin loaded in the particles in group 1), or (5) no treatment. Cells were exposed to particles at an OD of 0.25 (~15,000 particles/cell). For

darkfield imaging studies, cells were exposed to NCNS at an OD of 0.25 and either irradiated or not irradiated. For all cases exposed to NIR irradiation, cells were irradiated at 808 nm at 4 W/cm^2 for 3 min.

6.1.4.2. Analysis Using Fluorescence and Darkfield Microscopy

At 24 hr post particle dosing, cellular uptake of doxorubicin was assayed by fluorescent microscopy (560 nm excitation, 645 nm emission) using an Axiovert 135 inverted fluorescent microscope (Zeiss). Additionally, cells were stained with DAPI to visualize cell nuclei. Doxorubicin fluorescence intensity was quantified using ImageJ (NIH) and analyzed using an ANOVA with Tukey's HSD.

For darkfield imaging, cells were fixed at 1 hr post particle dosing (30 min post irradiation). Chamber wells were removed then cover slipped and imaged with an Axiovert 135 inverted fluorescence microscope (Zeiss) configured with a CytoViva darkfield condenser and EXFO X-Cite 120 Illumination System.

6.1.4.3. Analysis of Cell Viability

At 24 hr post particle dosing, cell viability was assessed using an MTS assay. Media in each well was removed and fresh media with MTS reagent (Promega) was added (100 μl media/ 20 μl reagent per well). After a 60 min incubation at 37 ^{o}C and 5% CO_2, absorbance readings of the media were taken at 490 nm. Absorbance readings were normalized to readings of the cell-only control (Group 5). Absorbance readings of the groups were compared using an ANOVA with a Tukey's post-hoc test.

6.2. Results

6.2.1. Material Stability

The stability of bare nanoshells, PEGylated nanoshells, and NCNS under 100 mM NaCl was analyzed over 4 hr, with representative extinction spectra of the three particles types displayed in Figure 6.1.

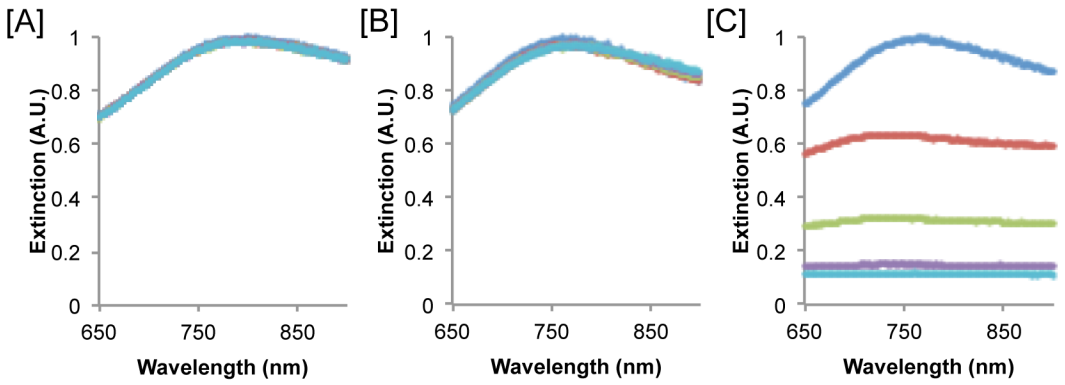

Figure 6.1. Extinction spectra of [A] NCNS, [B] PEGylated nanoshells, and [C] bare nanoshells after suspension in 100 mM NaCl for 0 hr (blue), 1 hr (red), 2 hr (green), 3 hr (purple) and 4 hr (turquoise).

For both the PEGylated and NCNS, the particle spectra did not change significantly over time, with peak absorption values maintaining over 95% of their original value over the 4 hr time period. The bare nanoshells, however, quickly aggregated and began to fall out of solution, as demonstrated by the rapid loss in peak absorption (Figure 6.2). These results suggest that the poly(NIPAAm-co-AAm) hydrogel coating of these particles is just as effective in preventing aggregation of particle under physiologically relevant salt concentrations as the PEG coatings commonly utilized on nanoshells.

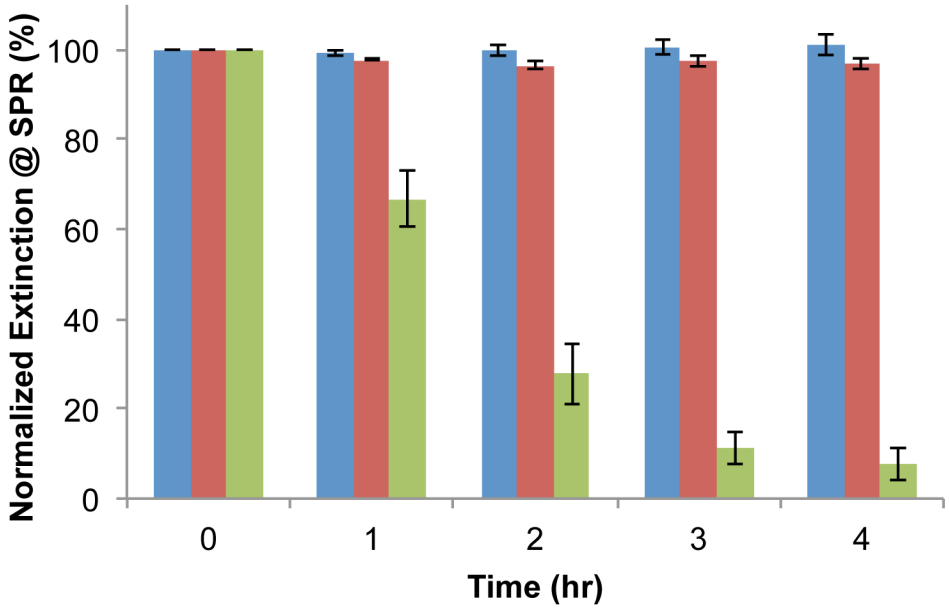

Figure 6.2. Changes in peak extinction of NCNS (blue), PEGylated nanoshells (red), and bare nanoshells (green) over a 4 hr suspension in 100 mM NaCl. Both PEGylated and poly(NIPAAm-co-AAm)-coated nanoshells remained stable over the 4 hr period as determined by minimal changes in their extinction spectra, while bare nanoshells aggregated and precipitated over time.

6.2.2. Material Cytotoxicity

Both 3T3s and HepG2s were exposed to a range of NCNS concentrations for 48 hr to determine if the poly(NIPAAm-co-AAm) coating induces any cytotoxic effects. Figure 6.3 displays cell viability at 48 hr in terms of percent viability as compared to untreated controls. Cell viability was greater than 90% in all groups, and no statistical differences were seen among any groups (ANOVA with Tukey's HSD), indicating that NCNS do not exhibit any material cytotoxicity.

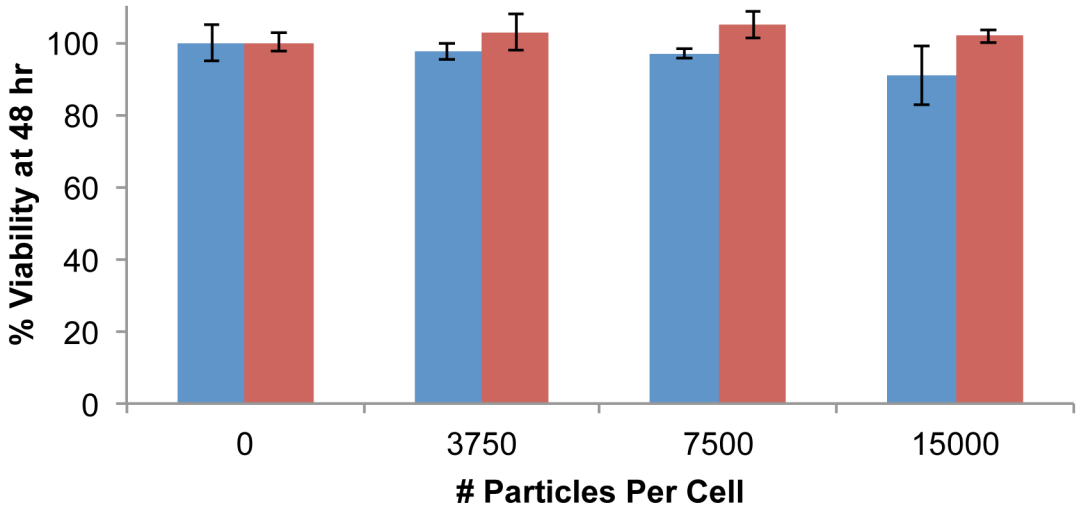

Figure 6.3. Material Cytotoxicity. Viability of 3T3 fibroblasts (blue) and HepG2s (red) exposed to increasing NCNS concentrations. Cell viability remained >90% in all groups and no statistical significance was observed among any groups by ANOVA.

6.2.3. Therapeutic Loading into Particles

Doxorubicin loading into the NCNS was assessed using UV-Vis spectroscopy. Spectra of NCNS at a concentration of 1.2 x 10^9 particles/ml and NCNS loaded with doxorubicin are shown in Figure 6.4A. The spectrum of the NCNS loaded contains two distinct peaks: one at 785 nm (as seen in unloaded NCNS) and one at 485 nm, as seen in the spectrum of doxorubicin. Furthermore, these two peaks can be separated by subtracting the NCNS spectrum from the NCNS + doxorubicin spectrum, yielding a spectrum with one peak which closely matches the spectrum of doxorubicin in solution (Figure 6.4B). From the two peaks in the NCNS + doxorubicin spectrum, both the number of particles [estimated using a Mie theory simulation (Averitt et al., 1999a) based on the peak at 785 nm] and the amount of doxorubicin loaded into the particles (estimated from the peak at 485 nm and using the concentration curve in Figure 6.4C) can

be calculated. Overall, doxorubicin loading was calculated to be 48.4 ± 0.3 μg of doxorubicin/10^9 particles, or approximately 5 x 10^7 doxorubicin molecules per particle.

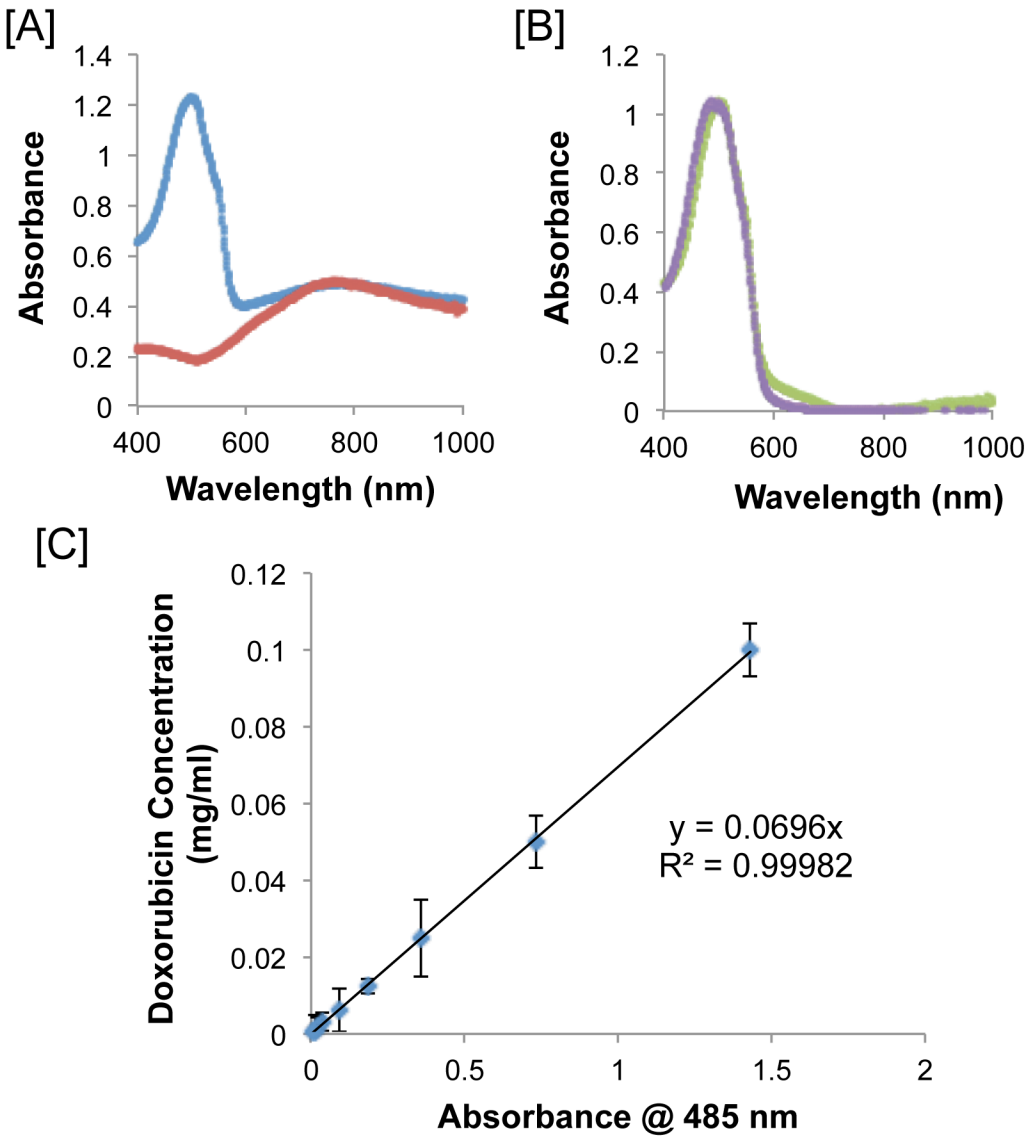

Figure 6.4. Loading of doxorubicin into NCNS. [A] Spectrum of NCNS + doxorubicin (blue) and NCNS at an OD of 0.5 (1.4 x 10^9 particles/ml, red). [B] The result of subtracting the NCNS spectrum from the NCNS + doxorubicin spectrum (green) closely matches the spectrum of doxorubicin at 0.07 mg/ml (purple). [C] Standard curve relating absorbance at 485 nm to concentration of doxorubicin in solution.

6.2.4. Therapeutic Release from Particles

Doxorubicin release from particles exposed to NIR irradiation or left at room temperature is displayed in Figure 6.5. Particles exposed to NIR irradiation released 22.2 ± 1.4 μg doxorubicin/10^9 particles, or approximately 46% of their payload. Minimal release was seen from particles that were not irradiated over the 3 min period. Additionally, only 6.6 ± 0.5 μg doxorubicin/10^9 particles, or less than 15% of the payload, was released from the particles after 72 hr at room temperature. Overall, these results indicate that 3 min of NIR irradiation is sufficient to trigger the delivery of a significant amount of doxorubicin from this delivery platform.

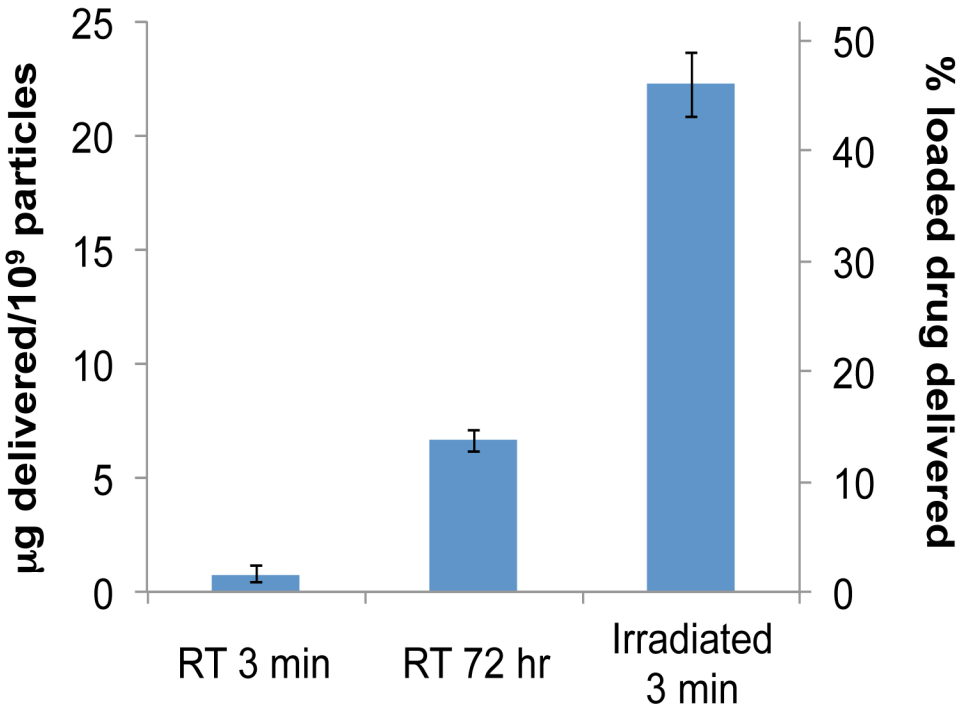

Figure 6.5. Delivery of doxorubicin from NCNS. After only 3 min of NIR irradiation, approximately 46% of the loaded doxorubicin is released from the particles. Release due to diffusion at room temperature is minimal, with less than 15% of the payload released over 72 hr.

6.2.5. *In vitro* Validation

6.2.5.1. Darkfield Microscopy

Due to the scattering properties of gold-silica nanoshells, these particles have been previously utilized as contrast agents for darkfield microscopy, a technique in which light strikes a sample at an angle so that only scattered light is captured (Loo et al., 2005). Since the poly(NIPAAm-co-AAm) hydrogel coating is fairly optically clear, it is hypothesized that the NCNS should retain similar scattering properties as seen in gold-silica nanoshells. Cells were exposed to NCNS for 60 min followed by fixation and darkfield imaging. Figure 6.6 clearly shows that NCNS can be visualized under darkfield microscopy. Non-irradiated NCNS (Figure 6.6A) appear as single particles dispersed throughout the entire sample, while irradiated NCNS (Figure 6.6B) tend to form more particle aggregates.

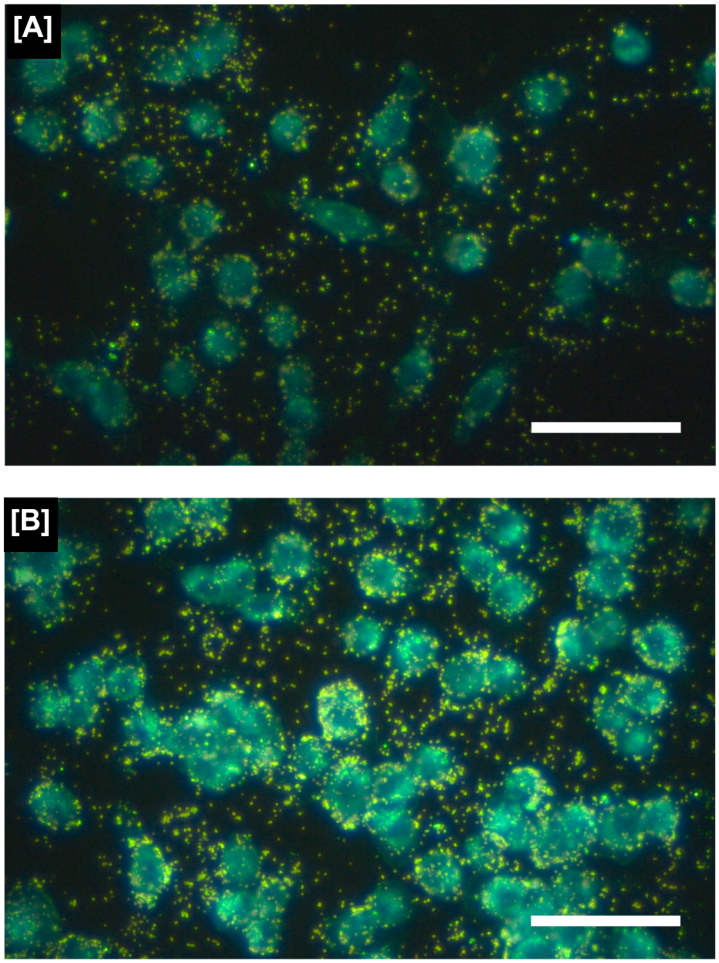

Figure 6.6. Darkfield microscopy images of NCNS distributed among CT.26WT cells. [A] Nonirradiated NCNS show a uniform distribution across the entire sample, whereas [B] irradiated NCNS tend to form multi-particle aggregates. Scale bars = 100 μm.

6.2.5.2. Doxorubicin Uptake

Fluorescence microscopy was used to analyze the amount of doxorubicin uptake by cells exposed to irradiated NCNS-doxorubicin particles, nonirraditaed NCNS-doxorubicin particles, and free doxorubicin at 24 hr post particle dosing. Figure 6.7 shows that cells exposed to irradiated NCNS-doxorubicin particles displayed nearly 3 times as much doxorubicin fluorescence per cell compared to the other two groups,

indicating that doxorubicin released from these irradiated particles efficiently enters the cells.

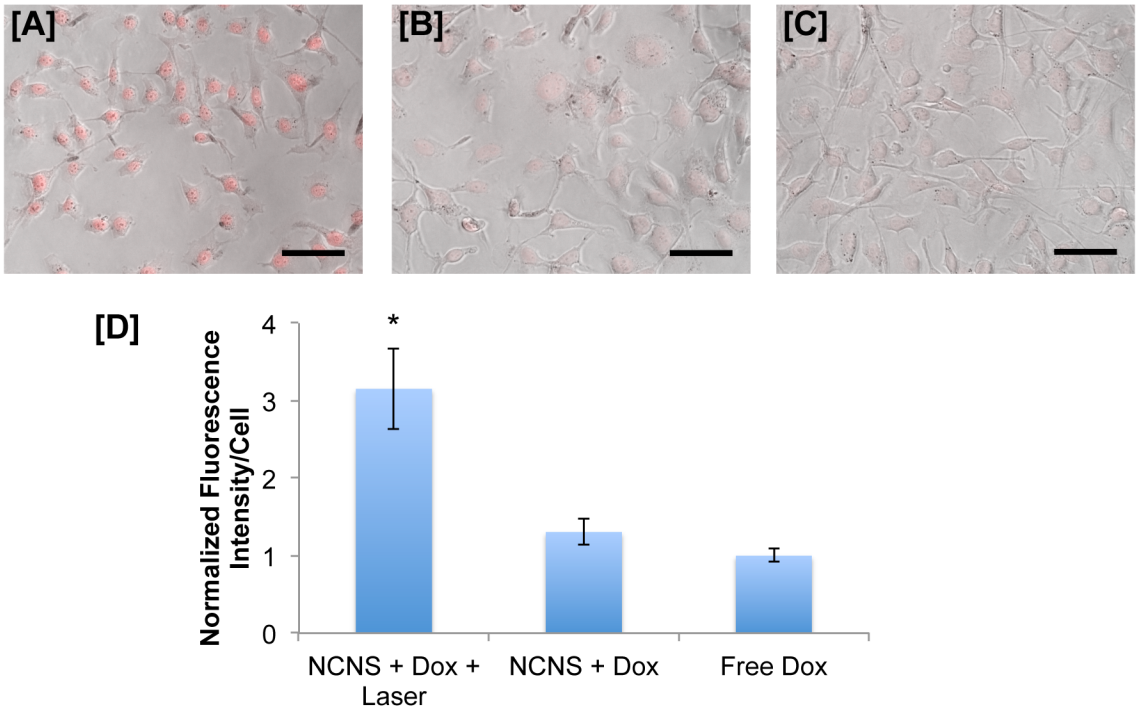

Figure 6.7. Uptake of doxorubicin by CT.26WT cells. [A-C] Phase contrast images overlayed with doxorubicin fluorescent signal for cells exposed to [A] irradiated NCNS-doxorubicin particles, [B] non-irradiated NCNS-doxorubicin particles, and [C] free doxorubicin. Scale bars = 100 mm [D] Quantification of doxorubicin fluorescence intensity per cell. Cells exposed to irradiated NCNS-doxorubicin particles showed almost 3x more doxorubicin fluorescence than the other groups (*$p<0.0001$, ANOVA).

Further analysis showed that the doxorubicin delivered by irradiated NCNS-doxorubicin particles is highly nuclear localized, as indicated by colocalization of both doxorubicin and DAPI fluorescence signals (Figure 6.8). Doxorubicin's main mechanism of action involves inhibition of topoisomerase-II, eventually causing permanent DNA damage and inhibition of cell proliferation (Tewey et al., 1984). This nuclear localization

of doxorubicin fluorescence suggests the drug is effectively entering the cells and available for inducing DNA damage.

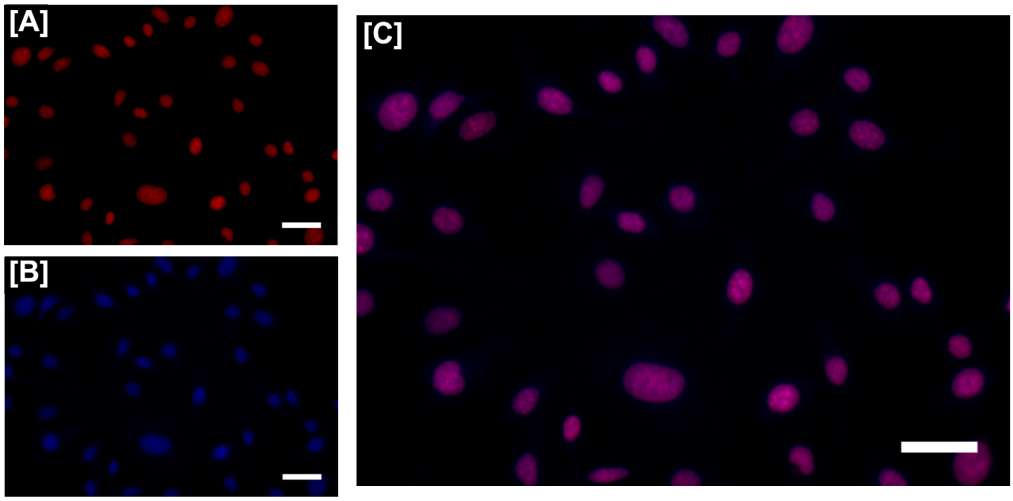

Figure 6.8. Cellular distribution of doxorubicin delivered from irradiated NCNS-doxorubicin particles. [A] Doxorubicin fluorescence signal localizes closely with [B] DAPI signal from cell nuclei, as demonstrated by an overaly of these two signals [C]. Scale bars = 50 μm.

6.2.5.3. Analysis of Cell Viability

To demonstrate that NCNS-doxorubicin particles can effectively deliver their therapeutic payload to CT.26WT cells upon NIR irradiation, cell viability was assessed 24 hr after particle dosing for the five conditions described in Section 6.1.4.1. Figure 6.9 displays these results. Cells exposed to NCNS-doxorubicin particles exposed to NIR irradiation resulted in almost a 90% decrease in cell viability compared to non-treated controls, whereas when these particles were not irradiated, but allowed to release doxorubicin via slow passive diffusion, only a 55% decrease was seen. Additionally, cells exposed to non-drug loaded NCNS that were irradiated did not show any changes in

viability, indicating the heating generated by these particles alone at this laser intensity and irradiation time was not sufficient to cause cell death.

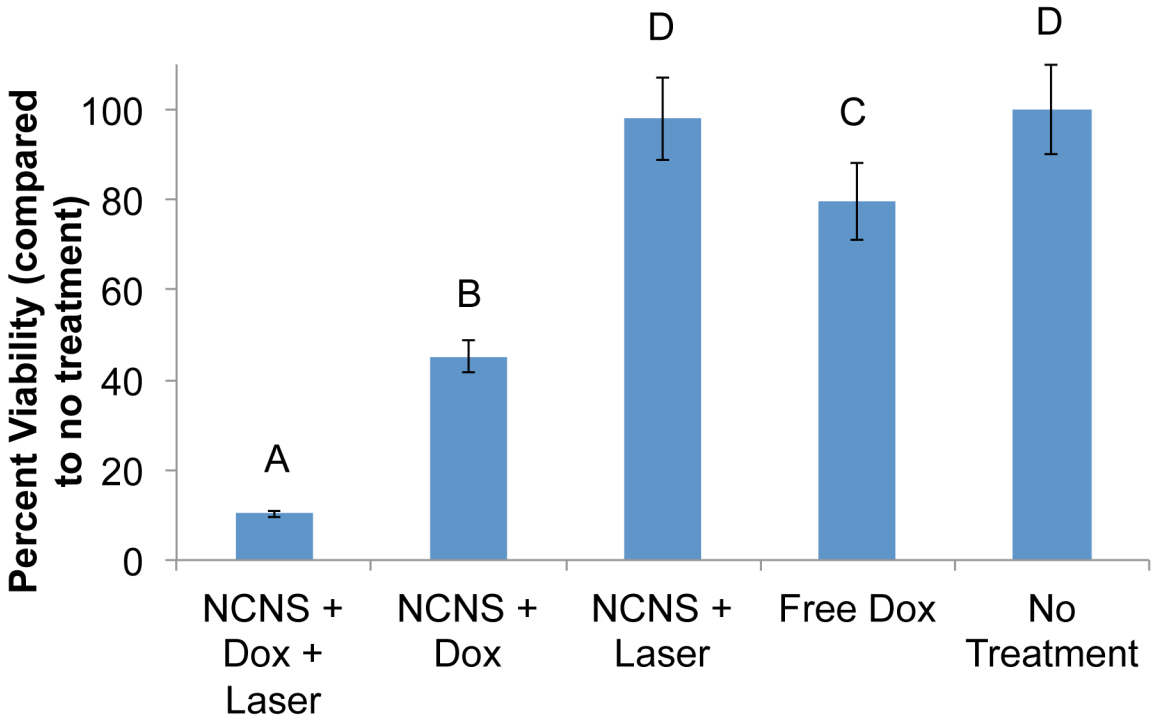

Figure 6.9. Changes in cell viability due to various treatment groups. Cells exposed to NCNS-doxorubicin particles triggered to release their doxorubicin payload by NIR irradiation showed increase loss is cell viability compared to cells exposed to NCNS-doxorubicin particles not exposed to NIR irradiation or free doxorubicin. Additionally, the heating caused by irradiating the NCNS alone was not sufficient to cause any cell death. Groups not connected by the same letter are statistically different from each other (ANOVA with Tukey's post-hoc).

6.3. Discussion and Future Directions

The studies presented in this chapter aimed to (1) validate that the NCNS developed in Chapter 5 are stable under physiological salt conditions and do not exhibit any material cytotoxicity, (2) analyze the loading capacity of these particles with the chemotherapeutic doxorubicin and trigger release of the drug in response to NIR

irradiation, and (3) investigate the ability of these doxorubicin-loaded NCNS to deliver their payload and elicit a therapeutic response *in vitro*.

The poly(NIPAAm-co-AAm) coating passivates the particle surface, preventing aggregation under salt conditions as effectively as the PEG coating traditionally used on gold nanoparticle platforms. Furthermore, these particles did not elicit any cytotoxicity against either fibroblasts or hepatic cells *in vitro*. The chemotherapeutic doxorubicin was loaded into the particles to a concentration of 5×10^7 drug molecules/particle, and 46% of the payload was released after just 3 min of NIR irradiation, whereas less than 15% was nonspecifically released over 72 hr. Furthermore, using darkfield microscopy it was seen that non-irradiated particles appear to be uniformly distributed throughout the sample, whereas irradiated particles tend to form larger particle aggregates. This is likely due to the hydrogel coating becoming more hydrophobic following its phase transition into a collapsed state, providing a driving force for aggregation in aqueous solutions.

Further analysis showed that this platform can effectively deliver its doxorubicin payload to colon carcinoma cells *in vitro*. Cells exposed to irradiated particles displayed nearly 3 times as much doxorubicin uptake as cells exposed to non-irradiated particles or free drug, as assessed by fluorescence microscopy. This in turn also resulted in a higher loss in cell viability. These differences may be due to the effects of the particle heating. Previous studies utilizing gold nanoshells have shown that nanoshell irradiation causes transient increases in membrane permeability (Hirsch et al., 2003, Day et al., 2010). As irradiation of this platform causing a release of high concentrations of drug molecules and induces an increase in membrane permeability at the same time, there is an increased

ability for drug molecules to enter the cell, causing increased uptake compared to non-irradiated particles or free drug controls.

Current and future efforts are focusing on investigating the *in vivo* efficacy of these doxorubicin-loaded NCNS. Such studies will be accomplished using mice with subcutaneous tumors. The maximum tolerated dose of doxorubicin in mice is ~5 mg/kg (MacKay et al., 2009), and the average weight of a mouse is ~30 g, translating to a maximum dose of 150 μg doxorubicin/mouse. Based on the loading of ~48 μg doxorubicin/10^9 particles achieved in this work, ~3.12 x 10^9 particles would be needed to achieve the maximum tolerated dose of free doxorubicin in mice. These particle concentrations are well below gold-silica nanoshell doses that have been previously used in mice (~10^{11} particles/mouse) (O'Neal et al., 2004), indicating relevant amounts of doxorubicin can be loaded into this platform. Further discussion of these investigations can be found in Section 8.3.1.

6.4. Conclusions

The work presented in Chapter 5 and 6 shows that the thermally-responsive composite material developed in Chapter 2 can be synthesized as injectable-sized particles. These particles retain the same properties as the bulk material: decreasing in size in response to both elevated temperatures or NIR irradiation. These particles can be loaded with doxorubicin and triggered to release their payload, and delivery from this platform results in an increased drug uptake compared to free drug, likely due to platform irradiation causing a transient increase in cell membrane permeability. In fact, under the laser conditions used, heating alone did not result in any cell death but appeared to

increase delivery of the drug payload. This transient increase in membrane permeability could be especially advantageous for drug molecules that cannot normally diffuse across a cell membrane, such as nucleic acid therapeutics. Chapter 7 of this dissertation further explores this irradiation-mediated membrane permeability for delivery of siRNA.

7. NIR Irradiation Mediated Uptake of siRNA

As was discussed in Section 1.2.1, nucleic acid-based therapeutics such as siRNA are large, anionic, and hydrophilic, and therefore cannot readily cross cell membranes via passive diffusion (Oh and Park, 2009). In order to improve delivery of such material, several viral-based delivery vehicles (commonly based on retroviruses and adenoviruses), as well as non-viral delivery vehicles (comprised of lipids, polymers, dendrimers, polypeptides, and nanoparticles), have been developed (Mintzer and Simanek, 2008). In addition, physical methods have been developed to compromise cell membrane integrity in order to increase delivery of genetic material, with a number of such approaches discussed in Table 7.1. However, most of these methods have severe drawbacks *in vivo*, including scale-up (seen with microinjection, where individual cells must be manipulated), tissue targeting and penetration (seen with the "gene gun" approach and sonoporation), and invasiveness (seen with electroporation).

Table 7.1. Summary of physical techniques used to increase cellular uptake of genetic material (Mehier-Humbert and Guy, 2005).

Physical Technique	Principle	Materials Required	Limitations *in vivo*
Microinjection	Manual injection into individual cells	Micropipette, microscope	Scale up—each cell must me manually manipulated
Gene Gun	High-velocity particle bombardment	"Gene gun", gold particles	Poor penetration across tissues
Electroporation	Electric field-induced cell membrane permeabilization	Electrodes, pulse generator	Toxicity, invasiveness (electrodes)
Sonoporation	Ultrasound-induced cell membrane permeabilization	Ultrasound probe, gas microbubbles	Efficacy, targeting only to disease sites

As has been previously discussed, the photothermal effects of gold-silica nanoshells are tightly localized to where NIR laser application and particles are combined. In addition, NIR permissibility across tissues allows for much deeper penetration depths than can be obtained by the "gene gun" approach. Therefore, the ability for irradiated gold-silica nanoshells to induce membrane permeability and augment cellular uptake of a nucleic acid therapy (siRNA) was investigated.

7.1. Effects of Gold-Nanoshell Irradiation on Cell Membranes

Previous studies of photothermal ablation using NIR absorbing nanoparticles suggest that heating due to the nanoparticle irradiation causes a loss in cell membrane integrity, leading to cell death. This phenomena was first reported in a study by Hirsch et al., in which SK-BR-3 carcinoma cells showed uptake of a fluorescent dextran molecule (MW 10,000) after incubation with gold-silica nanoshells and NIR irradiation for 7 min at 35 W/cm^2 (Figure 7.1) due to compromised cell membrane barriers (Hirsch et al., 2003).

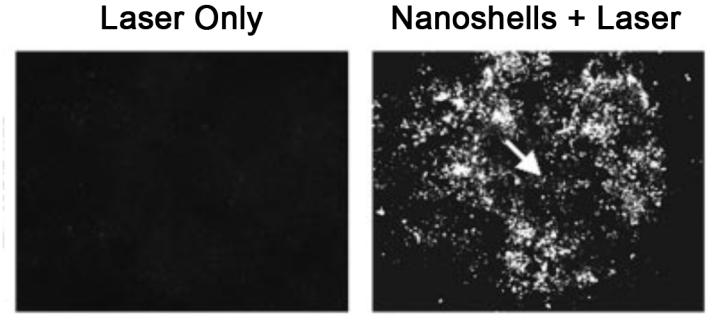

Figure 7.1. NIR irradiation increases cell membrane permeability. Cells irradiated in the presence of nanoshells (right) showed an increase in membrane permeability, as indicated by uptake of FITC-labeled dextran (10,000 MW). Cells exposed to NIR irradiation without nanoshells displayed minimal FITC-dextran uptake (left). Adapted from (Hirsch et al., 2003).

These changes in cell membrane integrity were further observed using NIR absorbing gold-gold sulfide nanoparticles exposed to a pulsed 810 nm laser (Day et al., 2010). Figure 7.2 shows time-lapse images of SK-BR-3 cells incubated with gold-gold sulfide nanoparticles exposed to NIR irradiation over 30 sec. Within 10 sec of exposure, membrane blebbling begins to occur, and further membrane damage as indicated by diffusion of a DiI membrane dye is seen after 30 sec (Day et al., 2010).

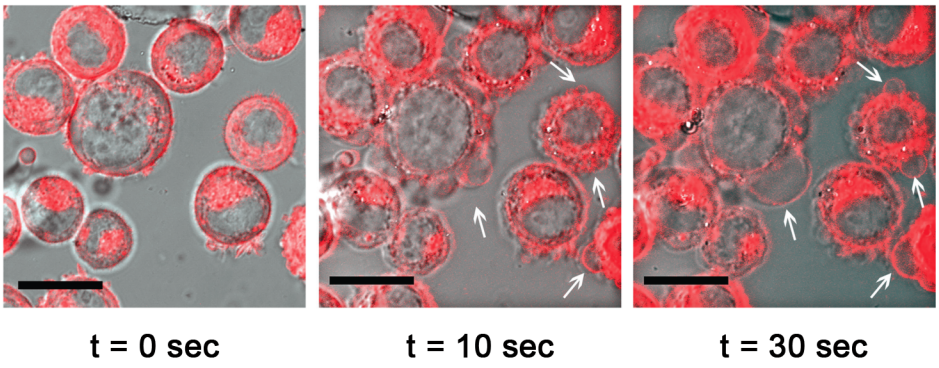

Figure 7.2. Cells incubated with gold-gold sulfide nanoparticles and exposed to a 50 mW femtosecond pulsed Ti:sapphire laser over 30 sec. A DiI membrane stain (red) shows membrane blebbing (indicated by arrows) occurring within 10 sec of laser exposure, with extensive membrane damage seen at 30 sec. Scale bars = 20 μm. Adapted from (Day et al., 2010).

Work in this chapter investigates whether this NIR irradiation induced cell membrane permeability can be exploited for the delivery of large, charged molecules, such as siRNA, which cannot diffuse through non-compromised cell membranes easily.

7.2. Materials and Methods

All reagents were purchased from Sigma-Aldrich and used as received, unless otherwise noted. All water used in synthesis, purification, and testing was treated by a Milli-Q system (≥18.0 MΩ·cm resistivity).

7.2.1. Cell Culture

Human prostate cancer cells (PC-3s) were cultured in Ham's F-12K media supplemented with 10% FBS, 100 U/l penicillin, and 100 mg/ml streptomycin. Cultures were maintained at 37 ^{o}C and 5% CO_2. For all studies cells were seeded at a density of 30,000 cells/well in 96-well plates.

7.2.2. Effects of Laser Power on Cell Viability

PC-3 cells were seeded at a density of 30,000 cells/well in 96-well plates and allowed to adhere overnight. The next day, gold-silica nanoshells at an O.D. of 4.5 (~1.3 x 10^9 particles/well) were added to the cell media and incubated for 30 min. Next, cells were irradiated with an 808 nm laser for 1 min at power densities of 2, 4, 6, 8, 10, or 20 W/cm^2. Cells were incubated for an additional 30 min, and viability staining was then assessed using calcein AM and ethidium homodimer-1 following the manufacturer's instructions (Life Technologies) and visualized using an Axiovert 135 inverted fluorescence microscope (Zeiss). Calcein AM is membrane permeable and cleaved by esterases found in live cells to produce a fluorescent green calcein product. Ethidium homodimer-1 cannot cross the membranes of live cells, but easily passes into dead cells with compromised membranes, binds to nucleic acids and fluoresces red.

7.2.3. Cellular Uptake of siRNA

Based on the laser power studies described, in Section 7.2.2, a laser power of 4 W/cm^2 and irradiation time of 1 min was chosen for transfection studies, as it was slightly below where cell death began to occur, and hypothesized that this power may cause

transient membrane permeability without causing cell death. Next, the ability for an siRNA molecule to be uptaken by cells under these conditions was assessed.

PC-3s were seeded at 30,000 cells/well in 96-well plates and allowed to adhere overnight. The next day, media containing nanoshells at an O.D. of 4.5 (~1.3 x 10^9 particles/well), 100 mM AF-488 tagged siRNA (Qiagen) was added to the cells and incubated for 30 min. Cells were then irradiated at 4 W/cm^2 for 1 min, and then incubated for an additional 30 min. After 30 min, the cells were rinsed 3 times with PBS, fixed using gluteraldehyde, stained with DAPI, and visualized with an Axiovert 135 inverted fluorescence microscope (Zeiss). Additionally, control groups where cells were exposed to both gold nanoshells and siRNA (without being irradiated by the NIR laser) or exposed to siRNA and irradiated (without nanoshells) were also analyzed. SiRNA uptake was quantified using the fluorescence intensity measurements using ImageJ (NIH) and compared using an ANOVA with Tukey's HSD.

7.3. Results

7.3.1. Effects of Laser Power on Cell Viability

The effects of laser power on cell viability were investigated by exposing cells incubated with nanoshells to increasing laser powers for 1 min, followed by analysis of cell viability using a live/dead assay. Results, shown in Figure 7.3, indicate that cells exposed to laser powers up to 4 W/cm^2 remained viable. Small numbers of dead cells were observed with a 6 W/cm^2 exposure, and increasing amounts of cell death were seen as laser powers were further increased. Based on these results, a laser power of 4 W/cm^2

was chosen for siRNA uptake studies, with the hypothesis it would elicit increased membrane permeability without causing cell death.

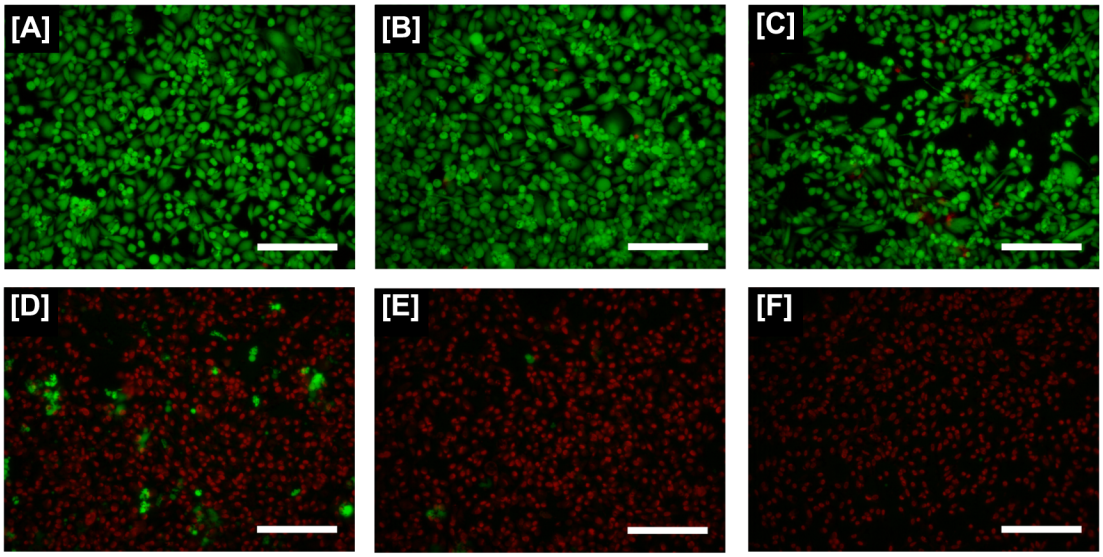

Figure 7.3. Effects of laser power on cell viability. Calcein AM (green, live) and ethidium homodimer-1 (red, dead) signal from cells exposed to 808 nm light at [A] 2, [B] 4, [C] 6, [D] 8, [E] 10, or [F] 20 W/cm^2 for 1 min. Increased cell death was observed with increased laser powers. Scale bars = 200 μm.

7.3.2. Cellular Uptake of siRNA

Cellular uptake of siRNA was analyzed by fluorescence microscopy 30 min after NIR laser exposure (Figure 7.4). Cells exposed to both nanoshells and NIR irradiation displayed fluorescence signal from the AF-488 tagged siRNA molecule, while minimal signal of this siRNA was seen in controls exposed to either nanoshells or NIR irradiation alone.

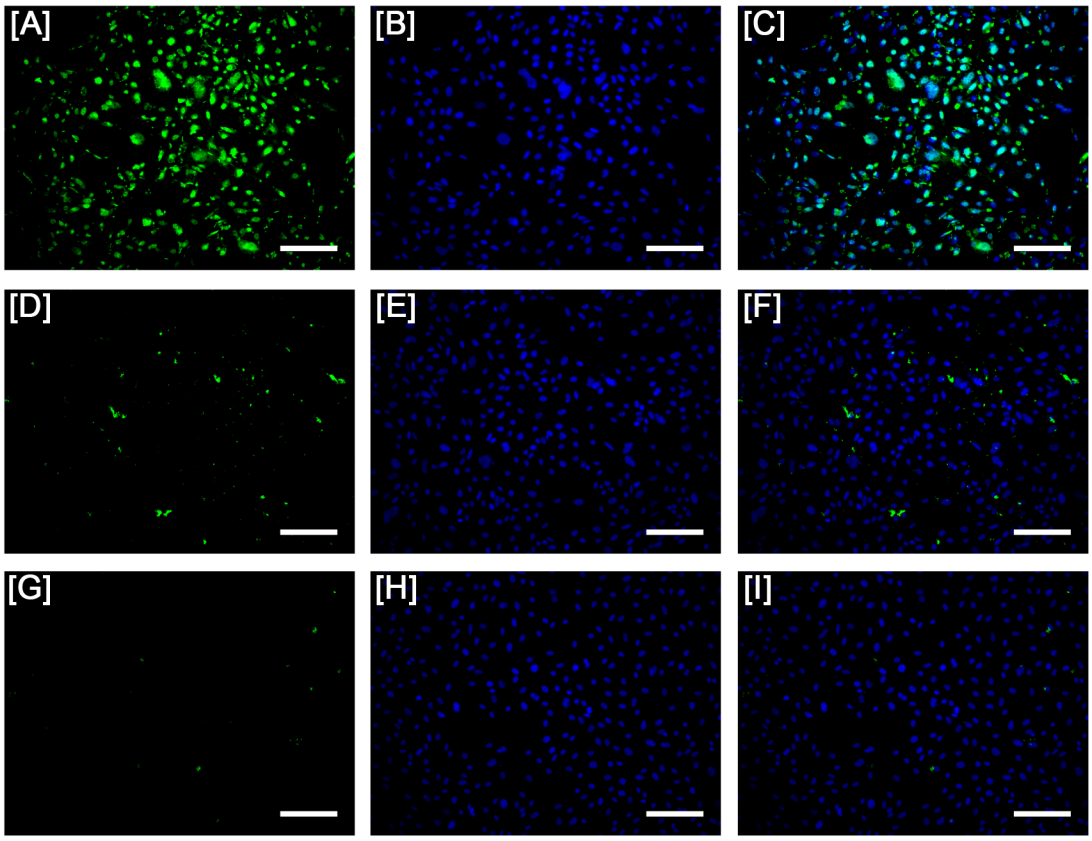

Figure 7.4. NIR irradiated nanoshells increase cellular uptake of siRNA. Cells exposed to both nanoshells and irradiation [A-C] showed increased signal of AF488-siRNA compared to nonirradiated cells exposed to nanoshells [D-F] and irradiated cells without nanoshells [G-I]. Images [A], [D], and [G] show signal from the AF488-siRNA, images [B], [E], and [H] show nuclear staining by DAPI, and images [C], [F], and [H] show and overlay of the two signals. Scale bars = 200 μm.

Uptake of siRNA was quantified by analyzing differences in AF-488 siRNA fluorescence intensity for the three groups. Cells exposed to both nanoshells and NIR irradiation showed over 25 times more siRNA uptake than the controls (Figure 7.5) indicating that this NIR irradiation induced membrane permeability causes increased delivery of siRNA molecules into cells.

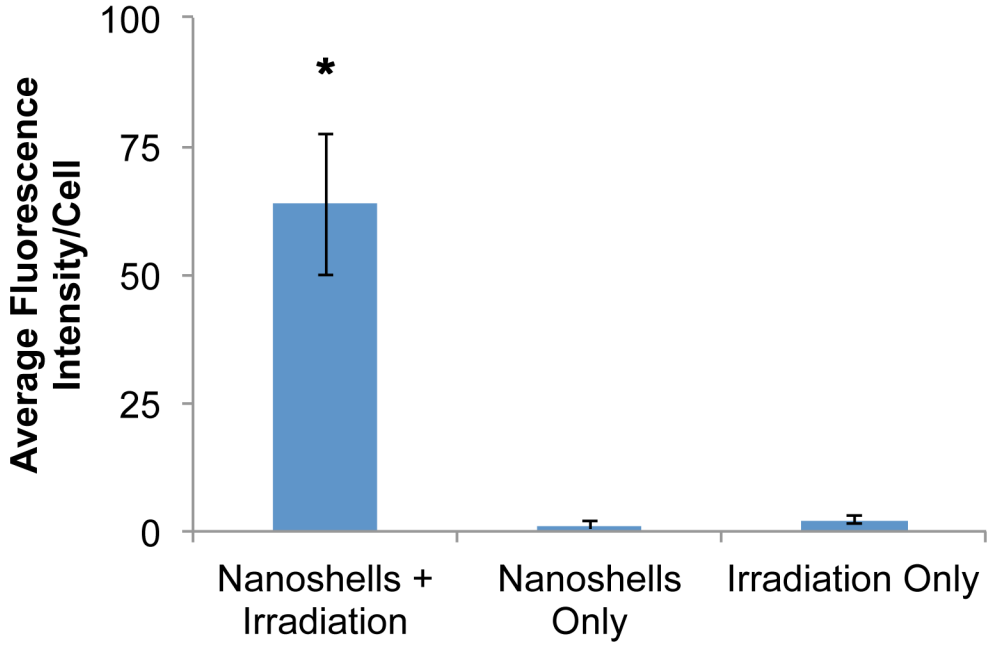

Figure 7.5. Quatification of AF488-siRNA fluorescence intensity. Cells exposed to NIR irradiated gold nanoshells displayed more than 25 times higher signal from the AF488-siRNA than nanoshell only and irradiation only controls. *p<0.001, ANOVA.

7.4. Conclusions and Future Directions

In this chapter, particle concentration and NIR laser settings were optimized in order to compromise cell membrane integrity without causing cell death due to heating. These setting elicited an increase in membrane permeability, which could be effectively exploited to delivery siRNA molecules which cannot easily diffuse through non-compromised cell membranes

Further studies should be performed to confirm the delivered siRNA molecules are functional and capable of knocking down protein expression of a target of interest. Additionally, while this study looked at co-delivery of nanoshells and free siRNA in cell media, further optimization should be done to load the siRNA into the NCNS developed

in Chapter 5 in order to create a single platform with both the therapeutic molecule (siRNA) and the membrane permeablizing agent (gold nanoshell).

8. Concluding Remarks and Future Directions

8.1. Introduction

Composite materials comprised of thermally responsive polymers and optically absorbing nanoparticles couple the ability of the nanoparticles to convert an external stimuli to heat with polymers that display sharp property changes in response to temperature changes, thus allowing for external control over polymer properties. Such systems have a variety of biomedical applications, including drug delivery. The goal of this dissertation was to develop an injectable-sized platform consisting of a thermally-responsive poly(NIPAAm-co-AAm)-gold nanoshell composite capable of externally-controlled, site-specific cancer therapy. Herein, the significance of the results of this dissertation will be presented and potential future studies and impact of this platform are discussed.

8.2. Summary of Work Presented and Significance

The platform in this dissertation was developed with two main goals in mind: (1) to encapsulate a therapeutic cargo as the platform circulated throughout the body, and (2) to trigger release of this cargo at a specific time and location. The first goal was accomplished by the utilization of a thermally-responsive poly(NIPAAm-co-AAm) hydrogel. This material acts similarly to a sponge, allowing therapeutic molecules to be absorbed within its pores. In addition, this hydrogel was found to have an LCST of 39-45 °C, thereby existing in a swollen state at physiologic temperature. The second goal was accomplished by the encapsulation of gold-silica nanoshells into the hydrogel. The nanoshells used in this thesis were tuned to have a peak absorption in the near-infrared

range, where biological tissue is most permissive to light. When exposed to light in this range, the nanoshells heated and elicited a temperature increase of surrounding material. This caused the hydrogel material to collapse and rapidly expel large amounts of water, demonstrating the capability of optically triggering this material phase transition.

Initial validation of this composite material was carried out using poly(NIPAAm-co-AAm) hydrogel discs (~4 mm in diameter) with encapsulated gold-silica nanoshells. This material could be loaded with a variety of therapeutic molecules ranging from small molecule chemotherapeutics (doxorubicin, ~580 Da) to large nucleic acid therapeutics (siRNA model molecule, ~14 kDa). NIR light exposure could effectively trigger release of both these molecules from the hydrogel material. Furthermore, doxorubicin delivered from this material could effectively enter cancer cells and elicit a therapeutic response. Overall, the work presented in Chapters 2-3 validated the potential for this composite material to be used for controlled delivery of cancer therapeutics.

Towards the translation of this composite material into *in vivo* applications, the composites were synthesized as injectable-sized particles rather than bulk discs. Chapters 4 and 5 investigated two different methods for the synthesis of such particles. In Chapter 4, a molding technique using a dissolvable gelatin template was used. In Chapter 5, surface initiated-atom transfer radical polymerization was employed to grow a layer of poly(NIPAAm-co-AAm) hydrogel onto individual nanoshells. Both methods successfully synthesized particles consisting of a nanoshell core surrounded by thin polymer layer, as analyzed by TEM. Furthermore, the hydrodynamic diameter of these particles decreased in response to either incubation at elevated temperatures or exposure to NIR irradiation,

proving that these particles retain the same thermal properties as the bulk material.

The hydrogel template method used in Chapter 4 did not allow for direct control over how many nanoshells were contained in each hydrogel particle, thus resulting in a heterogeneous particle population. Also, as each mold had to be manipulated individually, batch-size scale-ups proved difficult. For these reasons, particles synthesized using SI-ATRP were further explored for use as a drug delivery carrier in Chapter 6.

The hydrogel coating on the particles was found to act similarly to the PEG coatings commonly employed on metal nanoparticle platforms by effectively passivating particle surface and preventing aggregation under physiological salt concentrations. Additionally, the particles displayed no material cytotoxicity. Doxorubicin could be effectively loaded into the particles to concentration of ~5 x 10^7 doxorubicin molecules/particle, and NIR light exposure could trigger ~40% of the drug to release in just 3 min. Finally, the ability for this platform to deliver doxorubicin and elicit a therapeutic effect to colon carcinoma cells *in vitro* was confirmed. Notably, cells exposed irradiated doxorubicin-loaded particles should both increased doxorubicin uptake and loss of cell viability compared to free drug controls. It is hypothesized this is due to an increase in cell membrane permeability due to the particle heating, which in turn increases the ability of the drug to diffuse across the cell membrane compared to non-irradiated or free drug controls.

Finally, the ability for irradiated gold-silica nanoshells to induce membrane permeability and augment cellular uptake of a nucleic acid therapy (siRNA), which

normally does not diffuse across cell membranes easily, was further investigated in Chapter 7.

This ability to precisely control therapeutic delivery to malignant tissue would undoubtedly improve cancer management by overcoming the limitations of current therapies. The controlled release system designed would decrease the off-site toxicities of systemic chemotherapeutic regimens by minimizing drug exposure to non-malignant tissues, as well as increase the serum stability of fragile biologic therapeutics. Ultimately, this platform can be used to attack tumor tissue using two distinct mechanisms simultaneously: (1) photothermal heating and (2) delivery of multiple type of therapeutic molecules, providing a novel approach to effectively treat cancers when standard treatment modalities are not adequate.

8.3. Future Directions

8.3.1. *In vivo* Validation

Current and future efforts are focusing on investigating the *in vivo* efficacy of these doxorubicin-loaded NCNS. These studies are designed based on previous *in vivo* studies utilizing PEG-passivated gold nanoshells (see Section 2.1.3.2). In previous studies utilizing gold-silica nanoshells for photothermal therapy, the tumor is irradiated approximately 24 hours post nanoshell injection, as this is when nanoshell accumulation in tumor tissue is at a maximum (Gobin et al., 2007, Day et al., 2011). Because the hydrogel particles created in this study are of similar size to the PEGylated nanoshells used in these studies, a similar distribution is expected with tumor accumulation to be maximum 24 hours post injection, but a biodistribution study will be performed to

validate this hypothesis. If tumor accumulation is of these larger particles is limited, utilizing a smaller NIR absorbing particle type, such as gold-gold sulfide (Averitt et al., 1997) or hollow gold nanospheres (Lu et al., 2009), both of which are typically ~40 nm may be necessary.

After validation of particle accumulation in tumor tissue, a study comparing treatment using doxorubicin-loaded NCNS, non drug-loaded NCNS, and free doxorubicin will be performed. At 24 hours post-injection, mice will be exposed to an NIR laser (808 nm, 4 W cm^2, 3 min) as these conditions have been previously utilized in *in vivo* studies using gold-silica nanoshells (Day et al., 2011). After treatment, tumor growth and animal survival will be analyzed. It is hypothesized that mice treated with doxorubicin-loaded NCNS will show increased survival over the other groups due to the additive and potentially synergist treatment involving both heat and drug delivery.

8.3.2. Drug Combinations

The developed platform has the inherent ability to deliver a range of molecules, from small chemical drugs to large biologic therapeutics. It is the norm for most patients is to receive a cocktail of many different drugs rather than a single agent since combinations of drugs with different mechanisms of action show benefit in preventing drug resistant tumor cells (Chabner and Roberts, 2005). It is conceivable that this material could be loaded with multiple chemical therapeutics for delivery to a patient. Additionally, much research has been done showing an increased benefit of combining siRNA therapy with a chemotherapeutic such as doxorubicin, especially for multi-drug resistant cancers (Saraswathy and Gong, 2014); Table 8.1 details previous studies of

codelivery of doxorubicin and siRNA. The versatility of this platform for use with multiple types of therapeutics would allow for an ease of implementation of such regimens, ultimately leading to an improvement in cancer management.

Table 8.1. Studies of codelivery of doxorubicin and siRNA.

siRNA Target	Platform Material	Cancer Type	Admin-istration	Citation
MDR-1 (drug resistance)	Polymeric micelle (PEO-*b*-PCL)	MDA-MB-435/ LCC6MDR1 (MDR1 resistant breast carcinoma)	Intravenous injection (mice)	(Xiong and Lavasanifar, 2011)
MDR-1 (drug resistance)	PEI coated mesoporous silica nanoparticles	KB-V1 (MDR1 resistant cervical carcinoma)	*in vitro*	(Meng et al., 2010)
MDR-1 (drug resistance)	Phospholipid (DOPE)-PEI micelle	MCF-7 (breast carcinoma)	*in vitro*	(Navarro et al., 2011)
MDR-1 (drug resistance)	CdSe/ZnSe quantum dots	HeLa/Dox (doxorubicin resistant cervical cancer)	*in vitro*	(Li et al., 2012)
BCL-2 (anti-apoptosis)	Folate targeted polymeric micelle (PEI-*b*-PCL)	Rat C6 Glioma	Intratumoral injection (rats)	(Cheng et al., 2012)
BCL-2 (anti-apoptosis)	Nanostructured lipid carrier	A549 (lung carcinoma)	Inhalation (mice)	(Taratula et al., 2013)
BCL-xL (anti-apoptosis)	Polymersome (mPEG-*b*-PLA)	MKN-45, MKN-28 (gastric cancer)	*in vitro*	(Kim et al., 2013)
Survivin (anti-apoptosis)	mPEG-PLA/EPL polymer nanoparticles	B16-F10 (melanoma)	Intravenous (mice)	(Wang et al., 2013)
Nuclear Factor KB p65 (anti-apoptosis)	Polyglutamate brushes	HeLa (cervical cancer)	*in vitro*	(Zhao et al., 2013)

8.3.3. Clinical Translation

For translation of any optically-triggered platforms into a clinical setting, critical attention must be paid to laser-tissue interactions. NIR light was chosen as the optical trigger for this platform, as these wavelengths can penetrate soft tissue at a lower loss and lower risk of normal tissue damage compared to other wavelengths; NIR light can typically penetrate on the order of centimeters in soft tissue. This is because the main absorbers in soft tissue, water and proteins such as hemoglobin, do not significantly absorb light in this range. However, anatomical sites behind tissues such as bone or the chest wall may not be accessible to an external NIR light source. Additionally, intensity losses due to the scattering effects in tissue causes NIR light to become attenuated over long distances even in soft tissue, complicating treatment of deep-seeded tumors. In these cases, rather than exposing tumors to an external NIR source, use of a fiber optic probe that could be placed internally may be more appropriate. It is also important to note and adhere to the safety guidelines regarding maximum permissible exposures of lasers established by the Center for Devices and Radiological Health. In particular, there are limits regarding laser powers and exposure times acceptable for skin exposure in order to prevent skin burns and other adverse effects (Niemz, 2004). Additionally, there are several NIR fiber probes already approved for clinical use.

From past *in vivo* photothermal ablation studies, it has been found that a ~15 ^{o}C increase in temperature is required to cause cancer necrosis. This temperature increase can be tuned by both the nanoshell concentration in the tumor as well as the laser power used (with higher concentrations and laser powers leading to greater temperature

increases). The laser powers and durations used in this work (808 nm, 4 W/cm^2, 3 min) have been previously used for *in vivo* photothermal ablation studies and are below maximum permissible exposure values (O'Neal et al., 2004).

There are several potential sites for clinical application of an optically-triggered delivery platform. In the case of brain malignancies such as glioblastoma, photothermal therapy using gold nanoshells have shown promise as a potential treatment (Day et al., 2011, Day et al., 2012), and controlled drug delivery systems (Gliadel wafers) have shown much clinical success in this disease site (Westphal et al., 2003). One could envision a treatment scheme where chemotherapeutic-loaded particles were administered pre-surgery, and following resection tumor margins could be irradiated to prevent likelihood of recurrence. Alternatively, recent studies suggest combining regional hyperthermia with chemotherapy is more efficacious than chemotherapy alone in treating soft tissue sarcoma (Issels et al., 2010). A platform that combines both localized heating and chemotherapeutic delivery could be advantageous for such treatments. Additionally, while the platform in this work is designed to passively target tumor tissue through the EPR effect, active targeting of nanoparticles to tumor tissues via the addition of targeting moieties on the nanoparticle surface is a widely researched area today (Byrne et al., 2008). The hydrogel-coated nanoparticles developed could be functionalized with ligands such as antibodies, peptides, or aptamers, that selectively bind to antigens uniquely over-expressed in tumor tissue. Such an approach may be beneficial for the treatment of HER2+ breast cancer, in which nanoparticle platforms functionalized with antiHER2 antibodies have shown tremendous potential (Park et al., 2004, Lowery et al., 2006).

Ultimately, the platform developed in this work has the ability to overcome limitations of conventional cancer therapy, such as off-target effects, by tightly controlling therapeutic effects including heating and burst delivery of chemical or biological agents. In the future, such approaches have potential for providing a minimally-invasive treatment option with great therapeutic benefit.

9. References

ACHARYA, G., SHIN, C. S., MCDERMOTT, M., MISHRA, H., PARK, H., KWON, I. C. & PARK, K. 2010a. The hydrogel template method for fabrication of homogeneous nano/microparticles. *Journal of Controlled Release,* 141**,** 314-319.

ACHARYA, G., SHIN, C. S., VEDANTHAM, K., MCDERMOTT, M., RISH, T., HANSEN, K., FU, Y. & PARK, K. 2010b. A study of drug release from homogeneous PLGA microstructures. *Journal of Controlled Release,* 146**,** 201-206.

ADEN, A. L. & KERKER, M. 1951. Scattering of Electromagnetic Waves from Two Concentric Spheres. *Journal of Applied Physics,* 22**,** 1242-1246.

AGARWAL, A., MACKEY, M. A., EL-SAYED, M. A. & BELLAMKONDA, R. V. 2011. Remote Triggered Release of Doxorubicin in Tumors by Synergistic Application of Thermosensitive Liposomes and Gold Nanorods. *ACS Nano***,** 4919–4926.

AMERICAN CANCER SOCIETY 2010. Cancer Facts and Figures 2010. Atlanta: American Cancer Society.

ASAI, D., XU, D., LIU, W., GARCIA QUIROZ, F., CALLAHAN, D. J., ZALUTSKY, M. R., CRAIG, S. L. & CHILKOTI, A. 2012. Protein polymer hydrogels by in situ, rapid and reversible self-gelation. *Biomaterials,* 33**,** 5451-8.

AVERITT, R. D., SARKAR, D. & HALAS, N. J. 1997. Plasmon Resonance Shifts of Au-Coated Au_{2}S Nanoshells: Insight into Multicomponent Nanoparticle Growth. *Physical Review Letters,* 78**,** 4217-4220.

AVERITT, R. D., WESTCOTT, S. L. & HALAS, N. J. 1999a. Linear optical properties of gold nanoshells. *J. Opt. Soc. Am. B,* 16**,** 1824-1832.

AVERITT, R. D., WESTCOTT, S. L. & HALAS, N. J. 1999b. Ultrafast optical properties of gold nanoshells. *Journal of the Optical Society of America B,* 16**,** 1814-1823.

BARNER-KOWOLLIK, C., QUINN, J. F., MORSLEY, D. R. & DAVIS, T. P. 2001. Modeling the reversible addition–fragmentation chain transfer process in cumyl dithiobenzoate-mediated styrene homopolymerizations: Assessing rate coefficients for the addition–fragmentation equilibrium. *Journal Of Polymer Science Part A: Polymer Chemistry,* 39**,** 1353-1365.

BAXTER, L. T. & JAIN, R. K. 1989. Transport of fluid and macromolecules in tumors. I. Role of interstitial pressure and convection. *Microvasc Res,* 37**,** 77-104.

BENJAMIN, L. E., GOLIJANIN, D., ITIN, A., PODE, D. & KESHET, E. 1999. Selective ablation of immature blood vessels in established human tumors follows vascular endothelial growth factor withdrawal. *J Clin Invest,* 103**,** 159-65.

BERNARDI, R. J., LOWERY, A. R., THOMPSON, P. A., BLANEY, S. M. & WEST, J. L. 2008. Immunonanoshells for targeted photothermal ablation in medulloblastoma and glioma: an in vitro evaluation using human cell lines. *Journal of neuro-oncology,* 86**,** 165-72.

BIDWELL, G. L., 3RD & RAUCHER, D. 2005. Application of thermally responsive polypeptides directed against c-Myc transcriptional function for cancer therapy. *Molecular cancer therapeutics,* 4**,** 1076-85.

BIKRAM, M., GOBIN, A. M., WHITMIRE, R. E. & WEST, J. L. 2007. Temperature-sensitive hydrogels with SiO2-Au nanoshells for controlled drug delivery. *J Control Release,* 123**,** 219-27.

BIKRAM, M. & WEST, J. L. 2008. Thermo-responsive systems for controlled drug delivery. *Expert Opinion on Drug Delivery,* 5**,** 1077-1091.

BONAVENTURE, J., KADHOM, N., COHEN-SOLAL, L., NG, K. H., BOURGUIGNON, J., LASSELIN, C. & FREISINGER, P. 1994. Reexpression of Cartilage-Specific Genes by Dedifferentiated Human Articular Chondrocytes Cultured in Alginate Beads. *Experimental Cell Research,* 212**,** 97-104.

BUMCROT, D., MANOHARAN, M., KOTELIANSKY, V. & SAH, D. W. 2006. RNAi therapeutics: a potential new class of pharmaceutical drugs. *Nat Chem Biol,* 2**,** 711-9.

BYEON, J. H. & ROBERTS, J. T. 2012. Aerosol-based fabrication of biocompatible organic-inorganic nanocomposites. *ACS Appl Mater Interfaces,* 4**,** 2693-8.

BYRNE, J. D., BETANCOURT, T. & BRANNON-PEPPAS, L. 2008. Active targeting schemes for nanoparticle systems in cancer therapeutics. *Advanced Drug Delivery Reviews,* 60**,** 1615-1626.

CALLAHAN, D. J., LIU, W., LI, X., DREHER, M. R., HASSOUNEH, W., KIM, M., MARSZALEK, P. & CHILKOTI, A. 2012. Triple stimulus-responsive polypeptide nanoparticles that enhance intratumoral spatial distribution. *Nano Lett,* 12**,** 2165-70.

CARMELIET, P. & JAIN, R. K. 2000. Angiogenesis in cancer and other diseases. *Nature,* 407**,** 249-57.

CHABNER, B. A. & ROBERTS, T. G. 2005. Chemotherapy and the war on cancer. *Nat Rev Cancer,* 5**,** 65-72.

CHAKRABORTY, S., BISHNOI, S. W. & PEREZ-LUNA, V. H. 2010. Gold nanoparticles with poly(N -isopropylacrylamide) formed via surface initiated atom transfer free radical polymerization exhibit unusually slow aggregation kinetics *Journal of Physical Chemistry C,* 114**,** 5947-5955.

CHENG, D., CAO, N., CHEN, J., YU, X. & SHUAI, X. 2012. Multifunctional nanocarrier mediated co-delivery of doxorubicin and siRNA for synergistic enhancement of glioma apoptosis in rat. *Biomaterials,* 33**,** 1170-1179.

CHILKOTI, A., DREHER, M. R., MEYER, D. E. & RAUCHER, D. 2002. Targeted drug delivery by thermally responsive polymers. *Advanced Drug Delivery Reviews,* 54**,** 613-630.

CHIRRA, H. D., BISWAL, D. & HILT, J. Z. 2009. Controlled synthesis of responsive hydrogel nanostructures via microcontact printing and ATRP. *Polymers for Advanced Technologies***,** 773-780.

CHIRRA, H. D. & HILT, J. Z. 2010. Nanoscale Characterization of the Equilibrium and Kinetic Response of Hydrogel Structures. *Langmuir,* 26**,** 11249-11257.

CHIRRA, H. D., SPENCER, D. & HILT, J. Z. 2012. Isolate, functionalize, and release: the ISOFURE platform for the functionalization of nanoparticles. *Journal of Nanoparticle Research,* 14.

COESSENS, V., PINTAUER, T. & MATYJASZEWSKI, K. 2001. Functional polymers by atom transfer radical polymerization. *Progress in Polymer Science,* 26**,** 337-377.

COUGHLIN, A. J., ANANTA, J. S., DENG, N., LARINA, I. V., DECUZZI, P. & WEST, J. L. 2014. Gadolinium-Conjugated Gold Nanoshells for Multimodal Diagnostic Imaging and Photothermal Cancer Therapy. *Small,* 10**,** 556-565.

CUENCA, A. G., JIANG, H., HOCHWALD, S. N., DELANO, M., CANCE, W. G. & GROBMYER, S. R. 2006. Emerging implications of nanotechnology on cancer diagnostics and therapeutics. *Cancer,* 107**,** 459-66.

DANIEL, M.-C. & ASTRUC, D. 2004. Gold Nanoparticles: Assembly, Supramolecular Chemistry, Quantum-Size-Related Properties, and Applications toward Biology, Catalysis, and Nanotechnology. *Chemical Reviews,* 104**,** 293-346.

DAY, E., THOMPSON, P., ZHANG, L., LEWINSKI, N., AHMED, N., DREZEK, R., BLANEY, S. & WEST, J. 2011. Nanoshell-mediated photothermal therapy improves survival in a murine glioma model. *Journal of Neuro-Oncology,* 104**,** 55-63.

DAY, E. S., BICKFORD, L. R., SLATER, J. H., RIGGALL, N. S., DREZEK, R. A. & WEST, J. L. 2010. Antibody-conjugated gold-gold sulfide nanoparticles as multifunctional agents for imaging and therapy of breast cancer. *International journal of nanomedicine,* 5**,** 445-54.

DAY, E. S., MORTON, J. G. & WEST, J. L. 2009. Nanoparticles for thermal cancer therapy. *Journal of Biomechanical Engineering,* 131.

DAY, E. S., ZHANG, L., THOMPSON, P. A., ZAWASKI, J. A., KAFFES, C. C., GABER, M. W., BLANEY, S. M. & WEST, J. L. 2012. Vascular-targeted photothermal therapy of an orthotopic murine glioma model. *Nanomedicine,* 7**,** 1133-1148.

DONG, H. C., ZHU, M. Z., YOON, J. A., GAO, H. F., JIN, R. C. & MATYJASZEWSKI, K. 2008. One-pot synthesis of robust core/shell gold nanoparticles. *Journal of the American Chemical Society,* 130**,** 12852-+.

DONG, X. & MUMPER, R. J. 2010. Nanomedicinal strategies to treat multidrug-resistant tumors: current progress. *Nanomedicine,* 5**,** 597-615.

DREHER, M. R., LIU, W., MICHELICH, C. R., DEWHIRST, M. W. & CHILKOTI, A. 2007. Thermal cycling enhances the accumulation of a temperature-sensitive biopolymer in solid tumors. *Cancer Res,* 67**,** 4418-24.

DREHER, M. R., RAUCHER, D., BALU, N., MICHAEL COLVIN, O., LUDEMAN, S. M. & CHILKOTI, A. 2003. Evaluation of an elastin-like polypeptide-doxorubicin conjugate for cancer therapy. *Journal of controlled release : official journal of the Controlled Release Society,* 91**,** 31-43.

DROMI, S., FRENKEL, V., LUK, A., TRAUGHBER, B., ANGSTADT, M., BUR, M., POFF, J., XIE, J., LIBUTTI, S. K., LI, K. C. P. & WOOD, B. J. 2007. Pulsed-High Intensity Focused Ultrasound and Low Temperature–Sensitive Liposomes for Enhanced Targeted Drug Delivery and Antitumor Effect. *Clinical Cancer Research,* 13**,** 2722-2727.

DUFF, D. G., BAIKER, A. & EDWARDS, P. P. 1993. A new hydrosol of gold clusters. 1. Formation and particle size variation. *Langmuir,* 9**,** 2301-2309.

DUXBURY, M. S., ITO, H., ZINNER, M. J., ASHLEY, S. W. & WHANG, E. E. 2004. EphA2: a determinant of malignant cellular behavior and a potential therapeutic target in pancreatic adenocarcinoma. *Oncogene,* 23**,** 1448-56.

EDMONDSON, S., OSBORNE, V. L. & HUCK, W. T. 2004. Polymer brushes via surface-initiated polymerizations. *Chem Soc Rev,* 33**,** 14-22.

EJAZ, M., YAMAMOTO, S., OHNO, K., TSUJII, Y. & FUKUDA, T. 1998. Controlled Graft Polymerization of Methyl Methacrylate on Silicon Substrate by the Combined Use of the Langmuir‚àíBlodgett and Atom Transfer Radical Polymerization Techniques. *Macromolecules,* 31**,** 5934-5936.

ELBASHIR, S. M., HARBORTH, J., LENDECKEL, W., YALCIN, A., WEBER, K. & TUSCHL, T. 2001. Duplexes of 21-nucleotide RNAs mediate RNA interference in cultured mammalian cells. *Nature,* 411**,** 494-8.

FARADAY, M. 1857. The Bakerian Lecture: Experimental Relations of Gold (and Other Metals) to Light. *Philosophical Transactions of the Royal Society of London,* 147**,** 145-181.

FOLKMAN, J. 1971. Tumor angiogenesis: therapeutic implications. *N Engl J Med,* 285**,** 1182-6.

FORNARI, F. A., RANDOLPH, J. K., YALOWICH, J. C., RITKE, M. K. & GEWIRTZ, D. A. 1994. Interference by doxorubicin with DNA unwinding in MCF-7 breast tumor cells. *Mol Pharmacol,* 45**,** 649-56.

FRIMPONG, R. A. & HILT, J. Z. 2008. Poly(n-isopropylacrylamide)-based hydrogel coatings on magnetite nanoparticles via atom transfer radical polymerization. *Nanotechnology,* 19**,** 175101.

FURGESON, D. Y., DREHER, M. R. & CHILKOTI, A. 2006. Structural optimization of a "smart" doxorubicin-polypeptide conjugate for thermally targeted delivery to solid tumors. *Journal of controlled release : official journal of the Controlled Release Society,* 110**,** 362-9.

GAD, S. C., SHARP, K. L., MONTGOMERY, C., PAYNE, J. D. & GOODRICH, G. P. 2012. Evaluation of the toxicity of intravenous delivery of auroshell particles (gold-silica nanoshells). *Int J Toxicol,* 31**,** 584-94.

GALAEV, I. Y. & MATTIASSON, B. 1999. 'Smart' polymers and what they could do in biotechnology and medicine. *Trends in Biotechnology,* 17**,** 335-340.

GALE, N. W. & YANCOPOULOS, G. D. 1999. Growth factors acting via endothelial cell-specific receptor tyrosine kinases: VEGFs, angiopoietins, and ephrins in vascular development. *Genes & development,* 13**,** 1055-66.

GEORGE, M. & ABRAHAM, T. E. 2006. Polyionic hydrocolloids for the intestinal delivery of protein drugs: Alginate and chitosan — a review. *Journal of Controlled Release,* 114**,** 1-14.

GOBIN, A. M., LEE, M. H., HALAS, N. J., JAMES, W. D., DREZEK, R. A. & WEST, J. L. 2007. Near-Infrared Resonant Nanoshells for Combined Optical Imaging and Photothermal Cancer Therapy. *Nano Letters,* 7**,** 1929-1934.

GOBIN, A. M., MOON, J. J. & WEST, J. L. 2008. EphrinA I-targeted nanoshells for photothermal ablation of prostate cancer cells. *International journal of nanomedicine,* 3**,** 351-8.

GOBIN, A. M., WATKINS, E. M., QUEVEDO, E., COLVIN, V. L. & WEST, J. L. 2010. Near-Infrared-Resonant Gold/Gold Sulfide Nanoparticles as a Photothermal Cancer Therapeutic Agent. *Small,* 6**,** 745-752.

HAHN, G. M. 1979. Potential for therapy of drugs and hyperthermia. *Cancer Res,* 39**,** 2264-8.

HANAHAN, D. & WEINBERG, R. A. 2000. The hallmarks of cancer. *Cell,* 100**,** 57-70.

HANAHAN, D. & WEINBERG, R. A. 2011. Hallmarks of cancer: the next generation. *Cell,* 144**,** 646-74.

HASHIZUME, H., BALUK, P., MORIKAWA, S., MCLEAN, J. W., THURSTON, G., ROBERGE, S., JAIN, R. K. & MCDONALD, D. M. 2000. Openings between Defective Endothelial Cells Explain Tumor Vessel Leakiness. *The American Journal of Pathology,* 156**,** 1363-1380.

HILDEBRANDT, B., WUST, P., AHLERS, O., DIEING, A., SREENIVASA, G., KERNER, T., FELIX, R. & RIESS, H. 2002. The cellular and molecular basis of hyperthermia. *Critical Reviews in Oncology/Hematology,* 43**,** 33-56.

HIRSCH, L. R., GOBIN, A. M., LOWERY, A. R., TAM, F., DREZEK, R. A., HALAS, N. J. & WEST, J. L. 2006. Metal Nanoshells. *Annals of Biomedical Engineering,* 34**,** 15-22.

HIRSCH, L. R., STAFFORD, R. J., BANKSON, J. A., SERSHEN, S. R., RIVERA, B., PRICE, R. E., HAZLE, J. D., HALAS, N. J. & WEST, J. L. 2003. Nanoshell-mediated near-infrared thermal therapy of tumors under magnetic resonance

guidance. *Proceedings of the National Academy of Sciences of the United States of America,* 100**,** 13549-54.

HUANG, H. C., KORIA, P., PARKER, S. M., SELBY, L., MEGEED, Z. & REGE, K. 2008. Optically responsive gold nanorod-polypeptide assemblies. *Langmuir,* 24**,** 14139-44.

HUANG, X., EL-SAYED, I. H., QIAN, W. & EL-SAYED, M. A. 2006. Cancer Cell Imaging and Photothermal Therapy in the Near-Infrared Region by Using Gold Nanorods. *Journal of the American Chemical Society,* 128**,** 2115-2120.

ISSELS, R. D. 2008. Hyperthermia adds to chemotherapy. *Eur J Cancer,* 44**,** 2546-54.

ISSELS, R. D., LINDNER, L. H., VERWEIJ, J., WUST, P., REICHARDT, P., SCHEM, B.-C., ABDEL-RAHMAN, S., DAUGAARD, S., SALAT, C., WENDTNER, C.-M., VUJASKOVIC, Z., WESSALOWSKI, R., JAUCH, K.-W., DÜRR, H. R., PLONER, F., BAUR-MELNYK, A., MANSMANN, U., HIDDEMANN, W., BLAY, J.-Y. & HOHENBERGER, P. 2010. Neo-adjuvant chemotherapy alone or with regional hyperthermia for localised high-risk soft-tissue sarcoma: a randomised phase 3 multicentre study. *The Lancet Oncology,* 11**,** 561-570.

JAIN, R. K. 1987. Transport of molecules in the tumor interstitium: a review. *Cancer Res,* 47**,** 3039-51.

JAIN, R. K. 1990. Vascular and interstitial barriers to delivery of therapeutic agents in tumors. *Cancer Metastasis Rev,* 9**,** 253-66.

JAIN, R. K. 2005. Normalization of tumor vasculature: an emerging concept in antiangiogenic therapy. *Science,* 307**,** 58-62.

JAMES, W. D., HIRSCH, L. R., WEST, J. L., O'NEAL, P. D. & PAYNE, J. D. 2007. Application of INAA to the build-up and clearance of gold nanoshells in clinical studies in mice. *Journal of Radioanalytical and Nuclear Chemistry,* 271**,** 455-459.

JEONG, W., NAPIER, M. E. & DESIMONE, J. M. 2010. Challenging nature's monopoly on the creation of well-defined nanoparticles. *Nanomedicine,* 5**,** 633-639.

KEERL, M., SMIRNOVAS, V., WINTER, R. & RICHTERING, W. 2008. Copolymer Microgels from Mono- and Disubstituted Acrylamides: Phase Behavior and Hydrogen Bonds. *Macromolecules,* 41**,** 6830-6836.

KELLY, J. Y. & DESIMONE, J. M. 2008. Shape-Specific, Monodisperse Nano-Molding of Protein Particles. *Journal of the American Chemical Society,* 130**,** 5438-5439.

KELLY, K. L., CORONADO, E., ZHAO, L. L. & SCHATZ, G. C. 2002. The Optical Properties of Metal Nanoparticles: The Influence of Size, Shape, and Dielectric Environment. *The Journal of Physical Chemistry B,* 107**,** 668-677.

KIM, H.-O., KIM, E., AN, Y., CHOI, J., JANG, E., CHOI, E. B., KUKREJA, A., KIM, M.-H., KANG, B., KIM, D.-J., SUH, J.-S., HUH, Y.-M. & HAAM, S. 2013. A Biodegradable Polymersome Containing Bcl-xL siRNA and Doxorubicin as a Dual Delivery Vehicle for a Synergistic Anticancer Effect. *Macromolecular Bioscience,* 13**,** 745-754.

KIM, J., SERPE, M. J. & LYON, L. A. 2005. Photoswitchable Microlens Arrays. *Angewandte Chemie- International Edition,* 44**,** 1333-1336.

KIM, J.-H. & LEE, T. R. 2006. Discrete thermally responsive hydrogel-coated gold nanoparticles for use as drug-delivery vehicles *Drug Development Research,* 67**,** 61-69.

KIM, J.-H. & LEE, T. R. 2007. Hydrogel-Templated Growth of Large Gold Nanoparticles: Synthesis of Thermally Responisve Hydrogel-Nanoparticle Composites *Langmuir,* 23**,** 6504-6509.

KIM, J.-H. & LEE, T. R. 2008. Thermo-Responsive Hydrogel-Coated Nanoshells for In Vivo Drug Delivery. *Journal of Biomedical & Pharmaceutical Engineering* 2**,** 29-35.

KUO, C. K. & MA, P. X. 2001. Ionically crosslinked alginate hydrogels as scaffolds for tissue engineering: Part 1. Structure, gelation rate and mechanical properties. *Biomaterials,* 22**,** 511-521.

LANDEN, C. N., JR., CHAVEZ-REYES, A., BUCANA, C., SCHMANDT, R., DEAVERS, M. T., LOPEZ-BERESTEIN, G. & SOOD, A. K. 2005. Therapeutic EphA2 gene targeting in vivo using neutral liposomal small interfering RNA delivery. *Cancer research,* 65**,** 6910-8.

LANGER, R. 1990. New methods of drug delivery. *Science,* 249**,** 1527-33.

LANGER, R. S. & PEPPAS, N. A. 1981. Present and future applications of biomaterials in controlled drug delivery systems. *Biomaterials,* 2**,** 201-14.

LEWINSKI, N., COLVIN, V. & DREZEK, R. 2008. Cytotoxicity of nanoparticles. *Small,* 4**,** 26-49.

LI, D. X., HE, Q., CUI, Y., WANG, K. W., ZHANG, X. M. & LI, J. B. 2007. Thermosensitive copolymer networks modify gold nanoparticles for nanocomposite entrapment. *Chemistry-a European Journal,* 13**,** 2224-2229.

LI, G. F., FAN, J. D., JIANG, R. & GAO, Y. 2004. Cross-linking the linear polymeric chains in the ATRP synthesis of iron oxide/polystyrene core/shell nanoparticles. *Chemistry of Materials,* 16**,** 1835-1837.

LI, J.-M., WANG, Y.-Y., ZHAO, M.-X., TAN, C.-P., LI, Y.-Q., LE, X.-Y., JI, L.-N. & MAO, Z.-W. 2012. Multifunctional QD-based co-delivery of siRNA and doxorubicin to HeLa cells for reversal of multidrug resistance and real-time tracking. *Biomaterials,* 33**,** 2780-2790.

LIECHTY, W. B., KRYSCIO, D. R., SLAUGHTER, B. V. & PEPPAS, N. A. 2010. Polymers for drug delivery systems. *Annu Rev Chem Biomol Eng,* 1**,** 149-73.

LIU, W., DREHER, M. R., FURGESON, D. Y., PEIXOTO, K. V., YUAN, H., ZALUTSKY, M. R. & CHILKOTI, A. 2006. Tumor accumulation, degradation and pharmacokinetics of elastin-like polypeptides in nude mice. *Journal of controlled release : official journal of the Controlled Release Society,* 116**,** 170-8.

LIU, W., MACKAY, J. A., DREHER, M. R., CHEN, M., MCDANIEL, J. R., SIMNICK, A. J., CALLAHAN, D. J., ZALUTSKY, M. R. & CHILKOTI, A. 2010. Injectable intratumoral depot of thermally responsive polypeptide-radionuclide conjugates delays tumor progression in a mouse model. *Journal of Controlled Release,* 144**,** 2-9.

LOO, C., LOWERY, A., HALAS, N., WEST, J. & DREZEK, R. 2005. Immunotargeted Nanoshells for Integrated Cancer Imaging and Therapy. *Nano Letters,* 5**,** 709-711.

LOWERY, A. R., GOBIN, A. M., DAY, E. S., HALAS, N. J. & WEST, J. L. 2006. Immunonanoshells for targeted photothermal ablation of tumor cells. *International journal of nanomedicine,* 1**,** 149-54.

LU, W., XIONG, C., ZHANG, G., HUANG, Q., ZHANG, R., ZHANG, J. Z. & LI, C. 2009. Targeted photothermal ablation of murine melanomas with melanocyte-stimulating hormone analog-conjugated hollow gold nanospheres. *Clin Cancer Res,* 15**,** 876-86.

LU, Y., STUREK, M. & PARK, K. 2014. Microparticles produced by the hydrogel template method for sustained drug delivery. *Int J Pharm,* 461**,** 258-69.

MACEWAN, S. R., CALLAHAN, D. J. & CHILKOTI, A. 2010. Stimulus-responsive macromolecules and nanoparticles for cancer drug delivery. *Nanomedicine,* 5**,** 793-806.

MACKAY, J. A., CHEN, M., MCDANIEL, J. R., LIU, W., SIMNICK, A. J. & CHILKOTI, A. 2009. Self-assembling chimeric polypeptide-doxorubicin

conjugate nanoparticles that abolish tumours after a single injection. *Nature materials,* 8**,** 993-9.

MAEDA, H., WU, J., SAWA, T., MATSUMURA, Y. & HORI, K. 2000. Tumor vascular permeability and the EPR effect in macromolecular therapeutics: a review. *J Control Release,* 65**,** 271-84.

MALVERN INSTRUMENTS. 2014. *Dynamic Light Scattering: An Introduction in 30 Minutes. Technical Note MAK656-01.* [Online]. Malvern Insturments Ltd. [Accessed January 10 2014].

MARMOR, J. B. 1979. Interactions of hyperthermia and chemotherapy in animals. *Cancer Res,* 39**,** 2269-76.

MASCI, G., GIACOMELLI, L. & CRESCENZI, V. 2004. Atom Transfer Radical Polymerization of N-Isopropylacrylamide. *Macromolecular Rapid Communications,* 25**,** 559-564.

MATSUMURA, Y. & MAEDA, H. 1986. A New Concept for Macromolecular Therapeutics in Cancer Chemotherapy: Mechanism of Tumoritropic Accumulation of Proteins and the Antitumor Agent Smancs. *Cancer Research,* 46**,** 6387-6392.

MCDANIEL, J. R., MACEWAN, S. R., DEWHIRST, M. & CHILKOTI, A. 2012. Doxorubicin-conjugated chimeric polypeptide nanoparticles that respond to mild hyperthermia. *Journal of Controlled Release,* 159**,** 362-367.

MCKINNELL, R. G. 2006. *The Biological Basis of Cancer*, Cambridge University Press.

MEHIER-HUMBERT, S. & GUY, R. H. 2005. Physical methods for gene transfer: Improving the kinetics of gene delivery into cells. *Advanced Drug Delivery Reviews,* 57**,** 733-753.

MENG, H., LIONG, M., XIA, T., LI, Z., JI, Z., ZINK, J. I. & NEL, A. E. 2010. Engineered Design of Mesoporous Silica Nanoparticles to Deliver Doxorubicin and P-Glycoprotein siRNA to Overcome Drug Resistance in a Cancer Cell Line. *ACS Nano,* 4**,** 4539-4550.

MEYER, D. E., KONG, G. A., DEWHIRST, M. W., ZALUTSKY, M. R. & CHILKOTI, A. 2001a. Targeting a Genetically Engineered Elastin-like Polypeptide to Solid Tumors by Local Hyperthermia. *Cancer Research,* 61**,** 1548-1554.

MEYER, D. E., SHIN, B. C., KONG, G. A., DEWHIRST, M. W. & CHILKOTI, A. 2001b. Drug targeting using thermally responsive polymers and local hyperthermia. *Journal of Controlled Release,* 74**,** 213-224.

MINTZER, M. A. & SIMANEK, E. E. 2008. Nonviral Vectors for Gene Delivery. *Chemical Reviews,* 109**,** 259-302.

MOHAMED, M. B., ISMAIL, K. Z., LINK, S. & EL-SAYED, M. A. 1998. Thermal Reshaping of Gold Nanorods in Micelles. *The Journal of Physical Chemistry B,* 102**,** 9370-9374.

MORONES, J. R. & FREY, W. 2009. Room temperature synthesis of an optically and thermally responsive hybrid PNIPAM-gold nanoparticle. *Journal Nanoparticle Research,* 12**,** 1401-1414.

NANOSPECTRA BIOSCIENCES, L., ,. 2014. *TUMOR ABLATION USING AUROLASE® THERAPY* [Online]. Available: http://www.nanospectra.com/index.html.

NAVARRO, G., SAWANT, R. R., BISWAS, S., ESSEX, S., TROS DE ILARDUYA, C. & TORCHILIN, V. P. 2011. P-glycoprotein silencing with siRNA delivered by DOPE-modified PEI overcomes doxorubicin resistance in breast cancer cells. *Nanomedicine,* 7**,** 65-78.

NEEDHAM, D. 1999. Materials Engineering of Lipid Bilayers for Drug Carrier Performance. *MRS Bulletin,* 24**,** 32-41.

NEEDHAM, D., ANYARAMBHATLA, G., KONG, G. & DEWHIRST, M. W. 2000. A New Temperature-sensitive Liposome for Use with Mild Hyperthermia: Characterization and Testing in a Human Tumor Xenograft Model. *Cancer Research,* 60**,** 1197-1201.

NIEMZ, M. H. 2004. *Laser-Tissue Interactions: Fundamentals and Applications*, Springer.

NIKOOBAKHT, B. & EL-SAYED, M. A. 2003. Preparation and Growth Mechanism of Gold Nanorods (NRs) Using Seed-Mediated Growth Method. *Chemistry of Materials,* 15**,** 1957-1962.

NUNES, J., HERLIHY, K. P., MAIR, L., SUPERFINE, R. & DESIMONE, J. M. 2010. Multifunctional shape and size specific magneto-polymer composite particles. *Nano Lett,* 10**,** 1113-9.

NUPPONEN, M. & TENHU, H. 2007. Gold Nanoparticles Protected with pH and Temperature-Sensitive Diblock Copolymers. *Langmuir,* 23**,** 5352-5357.

O'NEAL, D. P., HIRSCH, L. R., HALAS, N. J., PAYNE, J. D. & WEST, J. L. 2004. Photo-thermal tumor ablation in mice using near infrared-absorbing nanoparticles. *Cancer Lett,* 209**,** 171-6.

ODIAN, G. G. 2004. *Principles of polymerization,* Hoboken, N.J. , Wiley-Interscience.

OH, Y. K. & PARK, T. G. 2009. siRNA delivery systems for cancer treatment. *Advanced drug delivery reviews,* 61**,** 850-62.

OLDENBURG, S. J., AVERITT, R. D., WESTCOTT, S. L. & HALAS, N. J. 1998. Nanoengineering of optical resonances. *Chemical Physics Letters,* 288**,** 243-247.

OWENS, D. E., EBY, J. K., JIAN, Y. & PEPPAS, N. A. 2007a. Temperature-responsive polymer-gold nanocomposites as intelligent therapeutic systems. *Journal of Biomedical Materials Research Part A,* 83A**,** 692-695.

OWENS, D. E., JIAN, Y., FANG, J. E., SLAUGHTER, B. V., CHEN, Y.-H. & PEPPAS, N. A. 2007b. Thermally Responsive Swelling Properties of Polyacrylamide/Poly(acrylic acid) Interpenetrating Polymer Network Nanoparticles. *Macromolecules,* 40**,** 7306-7310.

PARK, J., ESTRADA, A., SHARP, K., SANG, K., SCHWARTZ, J. A., SMITH, D. K., COLEMAN, C., PAYNE, J. D., KORGEL, B. A., DUNN, A. K. & TUNNELL, J. W. 2008. Two-photon-induced photoluminescence imaging of tumors using near-infrared excited gold nanoshells. *Optics Express,* 16**,** 1590-1599.

PARK, J. W., BENZ, C. C. & MARTIN, F. J. 2004. Future directions of liposome- and immunoliposome-based cancer therapeutics. *Seminars in Oncology,* 31, Supplement 13**,** 196-205.

PARK, K. 1997. *Controlled Drug Delivery: Challenges and Strategies*, American Chemical Soc.

PARROTT, M. C., FINNISS, M., LUFT, J. C., PANDYA, A., GULLAPALLI, A., NAPIER, M. E. & DESIMONE, J. M. 2012. Incorporation and controlled release of silyl ether prodrugs from PRINT nanoparticles. *J Am Chem Soc,* 134**,** 7978-82.

PARROTT, M. C., LUFT, J. C., BYRNE, J. D., FAIN, J. H., NAPIER, M. E. & DESIMONE, J. M. 2010. Tunable Bifunctional Silyl Ether Cross-Linkers for the Design of Acid-Sensitive Biomaterials. *Journal of the American Chemical Society,* 132**,** 17928-17932.

PETROS, R. A., ROPP, P. A. & DESIMONE, J. M. 2008. Reductively Labile PRINT Particles for the Delivery of Doxorubicin to HeLa Cells. *Journal of the American Chemical Society,* 130**,** 5008-5009.

PITSILLIDES, C. M., JOE, E. K., WEI, X., ANDERSON, R. R. & LIN, C. P. 2003. Selective Cell Targeting with Light-Absorbing Microparticles and Nanoparticles. *Biophysical Journal,* 84**,** 4023-4032.

PONCE, A. M., VUJASKOVIC, Z., YUAN, F., NEEDHAM, D. & DEWHIRST, M. W. 2006. Hyperthermia mediated liposomal drug delivery. *International Journal of Hyperthermia,* 22**,** 205-213.

QIN, G., LI, Z., XIA, R., LI, F., O'NEILL, B. E., GOODWIN, J. T., KHANT, H. A., CHIU, W. & LI, K. C. 2011. Partially polymerized liposomes: stable against leakage yet capable of instantaneous release for remote controlled drug delivery. *Nanotechnology,* 22**,** 155605.

QIU, Y. & PARK, K. 2001. Environment-sensitive hydrogels for drug delivery. *Advanced Drug Delivery Reviews,* 53**,** 321-339.

REUFER, M., DIAZ-LEYVA, P., LYNCH, I. & SCHEFFOLD, F. 2009. Temperature-sensitive poly(N-isopropyl-acrylamide) microgel particles: a light scattering study. *Eur Phys J E Soft Matter,* 28**,** 165-71.

ROLLAND, J. P., MAYNOR, B. W., EULISS, L. E., EXNER, A. E., DENISON, G. M. & DESIMONE, J. M. 2005. Direct fabrication and harvesting of monodisperse, shape-specific nanobiomaterials. *J Am Chem Soc,* 127**,** 10096-100.

RUBIN, P. & WILLIAMS, J. P. 2001. *Clinical Oncology: A Multidisciplinary Approach for Physicians and Students*, W.B. Saunders Company.

SAFRA, T., MUGGIA, F., JEFFERS, S., TSAO-WEI, D. D., GROSHEN, S., LYASS, O., HENDERSON, R., BERRY, G. & GABIZON, A. 2000. Pegylated liposomal doxorubicin (doxil): Reduced clinical cardiotoxicity in patients reaching or exceeding cumulative doses of 500 mg/m2. *Annals of Oncology,* 11**,** 1029-1033.

SALTIEL, E. & MCGUIRE, W. 1983. Doxorubicin (adriamycin) cardiomyopathy. *West J Med,* 139**,** 332-41.

SARASWATHY, M. & GONG, S. 2014. Recent developments in the co-delivery of siRNA and small molecule anticancer drugs for cancer treatment. *Materials Today*.

SASAK, S., KAWASAKI, H. & MAEDA, H. 1996. Volume Phase Transition Behavior of N-Isopropylacrylamide Gels as a Function of the Chemical Potential of Water Molecules. *Macromolecules,* 30**,** 1847-1848.

SATARKAR, N. S. & HILT, J. Z. 2008. Magnetic hydrogel nanocomposites for remote controlled pulsatile drug release. *J Control Release,* 130**,** 246-51.

SATARKAR, N. S., ZHANG, W., EITEL, R. E. & HILT, J. Z. 2009. Magnetic hydrogel nanocomposites as remote controlled microfluidic valves. *Lab Chip,* 9**,** 1773-9.

SCHILD, H. G. 1992. Poly(N-isopropylacrylamide): experiment, theory and application. *Progress in Polymer Science,* 17**,** 163-249.

SCHULZ, L. G. 1954. The Optical Constants of Silver, Gold, Copper, and Aluminum. I. The Absorption Coefficient k. *Journal of the Optical Society of America,* 44**,** 357-362.

SCHULZ, L. G. & TANGHERLINI, F. R. 1954. Optical Constants of Silver, Gold, Copper, and Aluminum. II. The Index of Refraction n. *Journal of the Optical Society of America,* 44**,** 362-367.

SEIWERT, T. Y., SALAMA, J. K. & VOKES, E. E. 2007. The concurrent chemoradiation paradigm--general principles. *Nat Clin Pract Oncol,* 4**,** 86-100.

SERSHEN, S. R., HALAS, N. J. & WEST, J. L. 2002a. Pulsatile Release of Insulin via Photothermally Modulated Drug Delivery. *Annual International Conference of the IEEE Engineering in Medicine and Biology- Proceedings,* 1**,** 490-491.

SERSHEN, S. R., MENSING, G. A., NG, M., HALAS, N. J., BEEBE, D. J. & WEST, J. L. 2005. Independent Optical Control of Microfluidic Valves Formed from Optomechnically Responsive Nanocomposite Hydrogels. *Advanced Materials,* 17**,** 1366-1368.

SERSHEN, S. R., NG, M., HALAS, N. J. & WEST, J. L. 2002b. Optically controllable materials: Potential valves and actuators in microfluidics and MEMs. *Annual International Conference of the IEEE Engineering in Medicine and Biology-Proceedings,* 3**,** 1822-1823.

SERSHEN, S. R., WESTCOTT, S. L., HALAS, N. J. & WEST, J. L. 2000. Temperature-sensitive polymer-nanoshell composites for photothermally modulated drug delivery. *Journal of Biomedical Materials Research Part A,* 51**,** 293-298.

SERSHEN, S. R., WESTCOTT, S. L., HALAS, N. J. & WEST, J. L. 2002c. Independent optically addressable nanoparticle-polymer optomechanical composites. *Applied Physics Letters,* 80**,** 4609-4611.

SERSHEN, S. R., WESTCOTT, S. L., WEST, J. L. & HALAS, N. J. 2001. An opto-mechanical nanoshell-polymer composite. *Applied Physics B,* 73**,** 379-381.

SHAN, J., CHEN, J., NUOPPONEN, M. & TENHU, H. 2004. Two Phase Transitions of Poly(N-isopropylacrylamide) Brushes Bound to Gold Nanoparticles. *Langmuir,* 20**,** 4671-4676.

SHAN, J., NUOPPONEN, M., JIANG, H., VIITALA, T., KAUPPINEN, E., KONTTURI, K. & TENHU, H. 2005. Amphiphilic Gold Nanoparticles Grafted with Poly(N-isopropylacrylamide) and Polystyrene
. *Macromolecules,* 38**,** 2918-2926.

SHIVAPOOJA, P., ISTA, L. K., CANAVAN, H. E. & LOPEZ, G. P. 2012. ARGET-ATRP synthesis and characterization of PNIPAAm brushes for quantitative cell detachment studies. *Biointerphases,* 7**,** 32.

SIMNICK, A. J., AMIRAM, M., LIU, W., HANNA, G., DEWHIRST, M. W., KONTOS, C. D. & CHILKOTI, A. 2011. In vivo tumor targeting by a NGR-decorated micelle of a recombinant diblock copolypeptide. *Journal of Controlled Release,* 155**,** 144-151.

SINGH, N. & LYON, L. A. 2007. Au Nanoparticle Templated Synthesis of pNIPAm Nanogels. *Chemistry of Materials,* 19**,** 719-726.

STOBER, W., FINK, A. & BOHN, E. 1968. Controlled growth of monodisperse silica spheres in the micron size range. *Journal of Colloid and Interface Science,* 26**,** 62-69.

STRONG, L. E. & WEST, J. L. 2011. Thermally responsive polymer–nanoparticle composites for biomedical applications. *Wiley Interdisciplinary Reviews: Nanomedicine and Nanobiotechnology,* 3**,** 307-317.

TARATULA, O., KUZMOV, A., SHAH, M., GARBUZENKO, O. B. & MINKO, T. 2013. Nanostructured lipid carriers as multifunctional nanomedicine platform for pulmonary co-delivery of anticancer drugs and siRNA. *Journal of Controlled Release,* 171**,** 349-357.

TEWEY, K. M., ROWE, T. C., YANG, L., HALLIGAN, B. D. & LIU, L. F. 1984. Adriamycin-Induced DNA Damage Mediated by Mammalian DNA Topoisomerase II. *Science,* 226**,** 466-468.

TURKEVICH, J., STEVENSON, P. C. & HILLER, J. 1951. A study of the nucleation and growth processes in the synthesis of colloidal gold. *Discussions of the Faraday Society,* 11**,** 55-75.

URRY, D. W. 1997. Physical Chemistry of Biological Free Energy Transduction As Demonstrated by Elastic Protein-Based Polymers‚Ä†. *The Journal of Physical Chemistry B,* 101**,** 11007-11028.

VASANI, R. B., MCINNES, S. J. P., COLE, M. A., JANI, A. M. M., ELLIS, A. V. & VOELCKER, N. H. 2011. Stimulus-Responsiveness and Drug Release from

Porous Silicon Films ATRP-Grafted with Poly(N-isopropylacrylamide). *Langmuir***,** null-null.

WANG, C., FLYNN, N. T. & LANGER, R. 2004a. Controlled Structure and Properties of Thermoresponsive Nanoparticle-Hydrogel Composites. *Advanced Materials,* 16**,** 1074-1079.

WANG, C., FLYNN, N. T. & LANGER, R. 2004b. Morphologically well-defined gold nanoparticles embedded in thermo-responisve hydrogel matrices. *Materials Research Society Symposium Proceedings,* 820**,** 333-338.

WANG, H., WU, Y., ZHAO, R. & NIE, G. 2013. Engineering the Assemblies of Biomaterial Nanocarriers for Delivery of Multiple Theranostic Agents with Enhanced Antitumor Efficacy. *Advanced Materials,* 25**,** 1616-1622.

WEBER, L. M., LOPEZ, C. G. & ANSETH, K. S. 2009. Effects of PEG hydrogel crosslinking density on protein diffusion and encapsulated islet survival and function. *J Biomed Mater Res A,* 90**,** 720-9.

WEI, Q., JI, J. & SHEN, J. 2008. Synthesis of Near-Infrared Responsive Gold Nanorod/PNIPAAm Core/Shell Nanohybrids via Surface Initiated ATRP for Smart Drug Delivery. *Macromolecular Rapid Communications,* 29**,** 645-650.

WEISSLEDER, R. 2001. A clearer vision for in vivo imaging. *Nat Biotech,* 19**,** 316-317.

WESTPHAL, M., HILT, D. C., BORTEY, E., DELAVAULT, P., OLIVARES, R., WARNKE, P. C., WHITTLE, I. R., JAASKELAINEN, J. & RAM, Z. 2003. A phase 3 trial of local chemotherapy with biodegradable carmustine (BCNU) wafers (Gliadel wafers) in patients with primary malignant glioma. *Neuro Oncol,* 5**,** 79-88.

XIA, Y., YIN, X., BURKE, N. A. D. & ST√∂VER, H. D. H. 2005. Thermal Response of Narrow-Disperse Poly(N-isopropylacrylamide) Prepared by Atom Transfer Radical Polymerization. *Macromolecules,* 38**,** 5937-5943.

XIONG, X.-B. & LAVASANIFAR, A. 2011. Traceable Multifunctional Micellar Nanocarriers for Cancer-Targeted Co-delivery of MDR-1 siRNA and Doxorubicin. *ACS Nano***,** null-null.

XU, F. J., NEOH, K. G. & KANG, E. T. 2009. Bioactive surfaces and biomaterials via atom transfer radical polymerization. *Progress in Polymer Science,* 34**,** 719-761.

YOSHIDA, R., SAKAI, K., OKANO, T. & SAKURAI, Y. 1994. Modulating the phase transition temperature and thermosensitivity in N-isopropylacrylamide copolymer gels. *Journal of Biomaterials Science Polymer Edition,* 6**,** 585-598.

YU, Y.-Y., CHANG, S.-S., LEE, C.-L. & WANG, C. R. C. 1997. Gold Nanorods: Electrochemical Synthesis and Optical Properties. *The Journal of Physical Chemicstry B,* 101**,** 6661-6664.

YUSA, S.-I., FUKUDA, K., YAMAMOTO, T., IWASAKI, Y., WATANABE, A., AKIYOSHI, K. & MORISHIMA, Y. 2007. Salt Effect on the Heat-Induced Association Behavior of Gold Nanoparticles Coated with Poly(N-isopropylacrylamide) Prepared via Reversible Addition−Fragmentation Chain Transfer (RAFT) Radical Polymerization. *Langmuir,* 23**,** 12842-12848.

ZAHR, A. S., DAVIS, C. A. & PISHKO, M. V. 2006. Macrophage Uptake of Core−Shell Nanoparticles Surface Modified with Poly(ethylene glycol). *Langmuir,* 22**,** 8178-8185.

ZHANG, T., LI, G., GUO, L. & CHEN, H. 2012. Synthesis of thermo-sensitive CS-g-PNIPAM/CMC complex nanoparticles for controlled release of 5-FU. *Int J Biol Macromol,* 51**,** 1109-15.

ZHAO, Y., QIN, Y., LIANG, Y., ZOU, H., PENG, X., HUANG, H., LU, M. & FENG, M. 2013. Salt-Induced Stability and Serum-Resistance of Polyglutamate Polyelectrolyte Brushes/Nuclear Factor-κB p65 siRNA Polyplex Enhance the Apoptosis and Efficacy of Doxorubicin. *Biomacromolecules,* 14**,** 1777-1786.

ZHOU, H. S., HONMA, I., KOMLYAMA, H. & HAUS, J. W. 1994. Controlled synthesis and quantum-size effect in gold-coated nanparticles. *Physical Review B,* 50**,** 12052-12056.

ZHU, C. H., HAI, Z. B., CUI, C. H., LI, H. H., CHEN, J. F. & YU, S. H. 2012. In situ controlled synthesis of thermosensitive poly(N-isopropylacrylamide)/Au nanocomposite hydrogels by gamma radiation for catalytic application. *Small,* 8**,** 930-6.

10. Biography

Laura Elizabeth Strong was born in Albuquerque, NM on July 8, 1986. She earned her B.S. in Biomedical Engineering (with honors) from the University of Texas at Austin in 2009 and her M.S. in Bioengineering from Rice University in 2012. During her graduate career, she was an HHMI Med into Grad Scholar and awarded a Nanobiology Interdisciplinary Graduate Training Program fellowship (NIH T32 EB009379). She has authored the following publications:

L.E. Strong and J.L. West. "Shrinkable, Thermally Responsive, Optically-triggerd NIPAAm coated Gold nanoshell (STRONG) particles for controlled delivery." In preparation.

L.E. Strong and J.L. West. "Optically modulated cancer therapeutic delivery: past, present and future." *Therapeutic Delivery*. In preparation. (Invited review).

L.E. Strong, S.N. Dahotre, and J.L. West. "Thermally-responsive hydrogel- gold nanoshell composite materials for optically modulated cancer therapeutic delivery. *J Controlled Release* **128:** 63-68 (2014) doi: 10.1016/j.jconrel.2014.01.014.

L.E. Strong and J.L. West. "Thermally Responsive Polymer-Nanoparticle Composites for Biomedical Applications." *Wiley Interdiscip Rev Nanomed Nanobiotechno*l. **3(3):** 307-317 (2011) doi: 10.1002/wnan.138.